E-258

MEASUREMENT OF THE ANGULAR AND ATOMIC WEIGHT DEPENDENCES OF HIGH TRANSVERSE MOMENTUM HADRON PRODUCTION IN π^-N COLLISIONS

BY

NIKOS GIOKARIS

JULY, 1981

FERMILAB
LIBRARY

THE UNIVERSITY OF CHICAGO

MEASUREMENT OF THE ANGULAR AND ATOMIC WEIGHT DEPENDENCES OF HIGH TRANSVERSE MOMENTUM HADRON PRODUCTION IN π^-N COLLISIONS

A DISSERTATION SUBMITTED TO
THE FACULTY OF THE DIVISION OF THE PHYSICAL SCIENCES
IN CANDIDACY FOR THE DEGREE OF
DOCTOR OF PHILOSOPHY

DEPARTMENT OF PHYSICS

BY

NIKOS D. GIOKARIS

CHICAGO, ILLINOIS

AUGUST, 1981

ACKNOWLEDGEMENTS

This work was made possible only because of the collective effort of many people. It is a pleasure to thank all of them.

I would like to thank the people who conceived and proposed this experiment and the construction of the High Intensity Pion Beam at FNAL: J. Cronin, H. Frisch and M. Shochet of The University of Chicago; and J. Boymond, P. Piroue and R. Sumner of the University of Princeton. My special thanks go to my collaborators who did the experiment: from Princeton University, Mike Halling, Pierre Piroue, Bernard Pope and Dick Sumner; and from The University of Chicago, Henry Frisch, James Green, Mac Mestayer, Carla Grosso-Pilcher, Lindsay Schachinger, Mel Shochet and Morris Swartz. Especially I would like to mention Dick Sumner who wrote the on-line programs, Carla Grosso-Pilcher for her work on the reconstruction program and Henry Frisch for writing the initial version of the Monte Carlo program. Jim Green did most of the analysis of the data. I entered the analysis at a later stage than he did and he was always willing to answer my numerous questions about the existing programs. It was a pleasure sharing an office with him. Mel Shochet and Mac Mestayer read one of the drafts of this thesis and made many corrections and useful comments.

Charles Edwards, an undergraduate at Princeton University at the time, worked on the construction and installation of the shower

counter. I thank Dick Armstrong, Robert Ryan, Cliff Brill, Sollie Lucero, Rudy Gabriel, Larry Fiscelli and Rich Northrop of the Engineering Services Department of the Enrico Fermi Institute, the staff of the EFI Electronics Shop and Howard Edwards and John Quinn of Princeton University for their design and construction of several components of the experiment and for their excellent technical support.

Many of the Figures in this thesis were created by plotting routines provided by Kelby Anderson. I thank him very much for making them available.

Above all I would like to thank my research advisor, Henry Frisch, for his guidance and support throughout my graduate work; also for reading and making many constructive suggestions on the many drafts of this thesis; the first one hand-written and almost in Greek!

My thanks go also to many people of the Proton Department at Fermilab for their help in installing and running the experiment. Ken Stanfield, John Hawkins, Age Visser, Ron Curier and Alan Guthke deserve special mention.

Last, but not least, I want to thank our secretary Kathy Visak for typing this thesis.

TABLE OF CONTENTS

page

ACKNOWLEDGEMENTS ii

LIST OF TABLES vii

LIST OF ILLUSTRATIONS ix

ABSTRACT xii

Chapter

I. INTRODUCTION 1

High Transverse Momentum Hadronic Processes

Angular Dependence of Hadron Production at High $P_\perp$

Atomic Weight Dependence

This Experiment (FNAL E258)

II. DESCRIPTION OF THE APPARATUS AND THE PION BEAM . . . 14

Proton West High Intensity Beam

Beam Monitors

The Magnetic Spectrometer

E258 Targets

Magnets

Collimators and Neutral Beam Dump

Trigger Counters

Čerenkov Counters

Shower Counter

Drift Chambers

Experimental Procedure

Data Acquisition

page

Chapter
III. DATA ANALYSIS 28

Transverse Momentum Scale

Momentum Calibration

Angle Between the Incident Beam and the Spectrometer

Yield Determination

Reconstruction Program

DST Program Data Cuts

Analysis of Low Momentum Runs

Corrections to the Particle Yields

Reconstruction Program Inefficiency

Computer Dead Time

Kaon Misidentification

Empty Target Subtraction

Correction for π, K Decay in Flight

Correction for Absorption from Material in the Spectrometer

Correction for Absorption in the Experimental Target

Acceptance

Monte Carlo

Slope Correction

Beam Normalization

Calibration of IC710

The Beam Normalization for the Hydrogen Target

The Beam Normalization for the Nuclear Targets

Backgrounds

Special Problems with the Analysis

Discussion of Errors

page

Chapter
IV. RESULTS 63

The production of High $P_\perp$ Hadrons in $\pi^- N$ Collisions

Data on Angular Dependence and Comparison with Theoretical Models

Nuclear Target Data - Atomic Weight Dependence

Conclusions

REFERENCES 75

LIST OF TABLES

Table page

1. QCD leading order elementary subprocesses 79

2. Primary and secondary beam energies and spectrometer angles . . 80

3. Proton West secondary beam yields 81

Particle composition of secondary beam 81

Secondary beam widths 81

4. E258 targets 82

5. E258 drift chambers 83

6. Muon to pion ratio versus momentum 84

7. Aperture and target cuts 85

8. Empty target contribution versus momentum 86

9. Number of absorption lengths of gas in the Čerenkov counter versus momentum 87

10. Number of absorption lengths for each particle from all other material in the spectrometer except Čerenkov gas 88

11. Absorption fractions for each particle type in each of the experimental targets 89

12. Integrated spectrometer acceptances for the nuclear targets . . 90

13. Integrated spectrometer acceptances for the hydrogen target . . 91

14. Absorption cross sections for the 200 and 300 π^- beam 92

15. IC710 scale factor 93

16. Center of mass angles versus momentum 94

17. Invariant cross sections

Beam: 200 GeV π^- ÷ Target: Hydrogen ÷ CM Angle: 90° 95

18. Invariant cross sections

Beam: 200 GeV π^- ÷ Target: Hydrogen ÷ CM Angle: 79° 96

Table page

19. Invariant cross sections

Beam: 200 GeV π^- ÷ Target: Hydrogen - CM Angle: 67° 97

20. FFF predicted meson invariant cross sections versus CM angle . 98

21. Angular dependence of π^-/π^+ trigger ratio in π^--p collisions . 99

22. Angular dependence of K^-/K^+ trigger ratio in π^--p collisions . 100

23. Angular dependence of $\bar{p}/p$ trigger ratio in π^--p collisions . . 101

24. Angular dependence of K^+/π^+ trigger ratio in π^--p collisions . 102

25. Angular dependence of K^-/π^- trigger ratio in π^--p collisions . 103

26. Invariant cross sections

Beam: 200 GeV π^- ÷ Target: Tungsten ÷ CM Angle: 90° 104

27: Invariant cross sections

Beam: 200 GeV π^- ÷ Target: Beryllium ÷ CM Angle: 90° . . . 105

28. Invariant cross sections

Beam: 200 GeV π^- ÷ Target: Copper ÷ CM Angle: 90° 106

29. Invariant cross sections

Beam: 300 GeV π^- ÷ Target: Tungsten ÷ CM Angle: 90° 107

30. The exponent $\alpha_i(P_\perp)$ for the production of hadrons with 200 GeV π^-'s 108

LIST OF ILLUSTRATIONS

Figure page

1. Diagram of deep inelastic electron proton scattering 110

2. Illustration of hard scattering models of large $P_\perp$ hadronic processes 112

3. Constituent Interchange Model (CIM) type diagram for high transverse momentum processes 114

4. The invariant cross section for inclusive π° production versus $x_\parallel$ in $\pi^- p$ and pp collisions at 200 GeV 116

5. Invariant cross section for inclusive π° production in pp collisions at $\sqrt{s}$ = 53 GeV versus the center of mass angle 118

6. Proton West high intensity secondary beam line at FNAL 120

7. Momentum bite of the secondary beam 122

8. Detail of the surroundings of the experimental target area . . 124

9. E258 spectrometer 126

10. The liquid hydrogen target 128

11. Two dimensional Čerenkov counter plot for a 25 GeV/c negative momentum run 130

12. Two dimensional Čerenkov counter plot for a 15 GeV/c negative momentum run 132

13. Electron, hadron, muon identifier (ehμ) 134

14. Plot of the stability of the yield 136

15. Logic diagram of the trigger electronics 138

16. Pressure curve of Čerenkov counter ČA 140

17. A diagram showing how the beam was pitched to the West 142

18. Distribution of the difference ΔX of the X-positions between all possible combinations of upstream and downstream X-tracks at the middle of the downstream dipole for a 20 GeV/c run. 144

Figure page

19. χ^2 distribution of the shower counter (ehμ) for a 25 GeV/c run 146

20. χ^2/DOF distribution in the horizontal and vertical planes for tracks with the best fit for a 25 GeV/c run 148

21. $\Delta P/P_0$ distribution for a 25 GeV/c run 150

22. Horizontal versus vertical positions of tracks at the experimental target for 25 GeV/c runs 152

23. (Number of Reconstructed Events/Number of Strobes) ratio versus the spectrometer momentum 154

24. Horizontal and vertical profiles of the 200 GeV π^- beam pitched to the West 156

25. Monte Carlo acceptances for each of the three overlapping runs versus momentum 158

26. The invariant cross section versus momentum bin for the three overlapping runs 160

27. Spectrometer acceptances versus the horizontal and vertical reconstructed angles of the particles at the target . . . 162

28. Comparison of Monte Carlo and data distributions 164

29. Integrated acceptance versus momentum for the nuclear targets 166

30. The momentum resolution of the spectrometer versus the momentum as found by the Monte Carlo program 168

31. Zero iteration invariant cross section for the reaction π^-+Be→π^-+X with 200 GeV beam 170

32. Measured and fitted local slopes versus $P_\perp$ 172

33. $\pi^- p \to \pi^+$ or π^- + anything invariant cross sections versus $P_\perp$ for the three CM angles 174

34. $\pi^- p \to K^+$ or K^- + anything invariant cross sections versus $P_\perp$ for the three CM angles 176

35. $\pi^- p \to p$ or $\bar{p}$ + anything invariant cross sections versus $P_\perp$ for the three CM angles 178

36. Comparison of the $\pi^- p \to \pi^+$, π^- + anything invariant cross sections versus $P_\perp$ with the predictions of the FFF model . . 180

37. Comparison of the $\pi^- p \to K^+$, K^- + anything invariant cross sections versus $P_\perp$ with the predictions of the FFF model . . 182

Figure page

38. The antiparticle/particle trigger ratios versus P for the three CM angles and the predictions of the FFF model for the π^-/π^+ and K^-/K^+ ratios 184

39. The K^+/π^+ and K^-/π^- trigger ratios versus P for three CM angles and the predictions of the FFF model 186

40. The π^-/π^+, K^-/K^+ and K^-/π^- trigger ratios versus the CM angle at $P_\perp$ = 4 GeV/c with 200 GeV π^- and proton beams and the predictions of the FFF model 188

41. Invariant cross sections per nucleus versus $P_\perp$ for the production of each of $\pi^\pm$, $K^\pm$, p and $\bar{p}$ in π^-W and π^-Be 200 GeV collisions 190

42. Comparison of the invariant cross sections per nucleus versus $P_\perp$ for the production of each of π^+, π^-, K^+, K^-, p and $\bar{p}$ with W and Be targets 192

43. Invariant cross sections per nucleus versus $P_\perp$ for the inclusive reaction $\pi^- + W \rightarrow \pi^+$, π^- + anything with 200 and 300 GeV beams 194

44. The invariant cross sections for the production of each of the π^+, π^-, K^+, K^-, p and $\bar{p}$ with the H, Be, Cu and W targets relative to the invariant cross section with the W target versus the logarithm of the atomic weight . . 196

45. The exponents α_i versus $P_\perp$ 198

ABSTRACT

We have measured the production of long lived hadrons ($\pi^{\pm}$, $K^{\pm}$, p and $\bar{p}$) in the 1→6 GeV/c transverse momentum range with a high intensity π^- beam incident on hydrogen and nuclear targets. We present the invariant cross sections, and some of their ratios for the production of different particles, at 90°, 79° and 67° CM angles in π^-p collisions with 200 GeV π^- beam. Also presented are the invariant cross sections with Be, Cu and W targets and a 200 GeV π^- beam, and those with a W target and a 300 GeV π^- beam. The nuclear target data are at 90° in the center of mass of the beam particle and a single nucleon in the target.

The results on the angular dependence in π^-p collisions are compared and found to be in qualitative agreement with a first order QCD calculation of a hard scattering parton model. However, substantial quantitative differences between the results and this model are observed.

The atomic weight dependence of the invariant cross sections with a π^- beam is found to be similar to the one with proton beams. If we parameterize the invariant cross section per nucleus as: $\sigma(P_\perp) = \sigma_0(P)A^{\alpha(P_\perp)}$ where σ_0 is a constant and A is the atomic weight, we find that the exponent α exceeds the value of 1 at high transverse momenta.

I dedicate it to my parents Helene and Demetres Giokaris

and

to a great teacher of mine, Garyphallia Kalaboke.

Τό ἀφιερώνω στούς γονεῖς μου
Ἑλένη καί Δημήτρη Γιόκαρη
καί
στήν ὑπέροχη καθηγήτριά μου
καί ἀνώτερο ἄνθρωπο
Γαρυφαλλιά Καλαμπόκη.

CHAPTER I

INTRODUCTION

High energy physics research is the continuation of a very long effort by man to understand the fundamental structure of matter.

It was first the ancient Greek natural philosophers who proposed that the variety of the properties of matter could be explained by the combination of a few fundamental elements. They thought that these were earth, water, air and fire. In the 5th century B.C. Democritus of Abdera advocated that matter was constructed out of some indivisible fundamental blocks which he called atomon (atomon = nondivisible).

Our present understanding of the structure of matter is founded on a series of great discoveries made only during the last 200 years. Dalton (1766-1844) established the basic ideas of the modern atomic theory (the law of partial pressures and the law of multiple proportions). Mendeleev discovered the connection between the chemical properties and the atomic weight of elements and in 1869 constructed the periodic table of elements.

In 1897 J.J. Thomson discovered the electron and in 1911 Rutherford proposed the first realistic model of the atom following the Geiger and Marsden experiments on alpha particle scattering from thin gold foils. According to Rutherford's model nearly all the mass of the atom is concentrated at its center in a region of positive

charge, the nucleus with a radius of $\sim 10^{-13}$ cm. The remaining space of the atom (radius $\sim 10^{-8}$ cm) is almost empty: there are only electrons orbiting the central positive charge.

In 1913 Bohr perfected Rutherford's theory by an early use of quantum mechanical ideas. For the next 20 years further development of quantum mechanics put forth the foundations of the modern theoretical understanding of the atom.

In 1932 Chadwick discovered the neutron. Later it was established that this particle was one of the two constituents of the nucleus, the other being the proton. Protons and neutrons are known today as nucleons.

During the last thirty years, with the advent of accelerators, it has become possible to "look" at distances even smaller than the nucleon dimensions. Once more another level in the structure of matter has been revealed. The nucleon proved to be made of smaller, even more fundamental blocks. They were given the name partons by Feynman.

The way to study the parton properties and their interactions is through "hard processes"[1] i.e., processes in which a large amount of momentum is transferred between the interacting particles. According to the uncertainty principle ($\Delta x = \hbar/\Delta p$), large momentum transfers imply collisions at small distances. Therefore by studying "hard processes" we can probe the structure of matter on a very small scale. Also we hope to be able to compare the experimental results with the predictions of asymptotically free theories of the strong interactions like quantum chromodynamics (QCD). This kind of theory, based on the assumption that the strong coupling constant decreases as the distance

between the interacting particles decreases, used perturbation theory to make predictions about small distance phenomena. At present quantitative predictions do not exist; it can be hoped, however, that progress will be made in calculating numbers.

One kind of "hard process" is the deep inelastic electron proton scattering with large momentum transfer, Q^2. The first direct evidence that the proton has structure was found at SLAC in the late 1960's from the study of such processes. It was observed that in deep inelastic electron proton scattering with large momentum transfer, Q^2, the invariant cross section (see Figure 1) behaved[1] as:

$$E_0 \frac{d^3\sigma}{dE^3} = \frac{1}{Q^4} \times (\text{a function of dimensionless parameters}) \qquad (1.1)$$

This is just the form expected for scattering from a point particle. Earlier experiments[2] in eN scattering at Stanford at much smaller momentum transfer had measured the nucleon form factors establishing that the nucleon was not pointlike. The above two facts put together suggested that the nucleon had pointlike substructure.

The SLAC machine allows momentum transfer up to Q^2 ~20 $(\text{GeV/c})^2$. According to the uncertainty principle[3] this gives the possibility to distinguish objects as small as 4×10^{-15} cm inside the nucleon.

In our experiment we studied another class of "hard processes", namely high transverse momentum hadron production in hadron-hadron collisions. These kind of processes are discussed in the following section.

High Transverse Momentum Hadronic Processes

The inclusive cross sections in hadronic collisions versus $P_\perp$ in the 0 to ~1 GeV/c $P_\perp$ region show the following two characteristics:

1) the invariant cross sections fall off very steeply with increasing $P_\perp$ as $\sigma \propto e^{-6P_\perp}$, and

2) they are approximately independent of the center of mass energy $\sqrt{s}$ of the collision.

Note that if the $e^{-6P_\perp}$ behavior at low $P_\perp$ is extrapolated to infinite $P_\perp$ it gives:

$$\langle P_\perp \rangle = \frac{\int_0^\infty P_\perp^2 e^{-6P_\perp} dP_\perp}{\int_0^\infty P_\perp e^{-6P_\perp} dP_\perp} \simeq 340 \text{ MeV/c} \tag{1.2}$$

This value of $\langle P_\perp \rangle$ corresponds to a distance of $\sim 10^{-13}$ cm, i.e., about equal to the size of the proton.

In 1971 the ISR machine at CERN came into operation. By the end of 1972 three ISR experiments[4,5,6] had discovered anomalously large hadron production at large $P_\perp$ (by large we mean $P > 2$ GeV/c), as compared to what would be expected from extrapolation of the $e^{-6P_\perp}$ behavior observed at low $P_\perp$. Similar behavior was observed soon after at Fermilab first in proton-nucleus[7] and then in proton-proton[8] collisions.

This behavior, although surprising, was not quite unexpected.

In 1971-72 theoretical papers[9,10] had suggested the possibility of using hadron production at large $P_\perp$ to investigate the nature of the nucleon. They were prompted by the Bjorken scaling observed in the deep inelastic lepton scattering experiments (see Equation (1.1), page 3). However, as often happens, the theoretical predictions did not match well what was observed.

The basic diagram of a hard scattering process between hadrons[11] is illustrated in Figure 2. In such processes a constituent a of the beam hadron A, carrying a momentum fraction x_a, interacts with the

constituent b of the target hadron B. The resulting constituents c and d fragment into the observed hadrons. In the inclusive processes we look at only one hadron with a high $P_\perp$. This hadron (h_1 in Figure 2) carries a fraction z of the parent constituent c momentum. In Figure 2 the functions G give the probability of finding a constituent a or b in A or B respectively with corresponding fractions of their momenta x_a and x_b. Function D gives the probability that hadron h_1 will carry a fraction z of the parent constituent c. The cross section for the subprocess a+b→c+d is described by $d\hat{\sigma}/d\hat{t}$. The invariant cross section for the inclusive process

$$A + B \rightarrow h_1 + X$$

is then given by the expression[11]

$$E\frac{d^3\sigma}{dp^3} = \sum_{a,b} \int dx_a\, dx_b\, dz\, G_{A-a}(x_a)\, G_{B-b}(x_b)\, D_c^{h_1}(z)\, \frac{1}{z}\, \frac{1}{\pi}\, \frac{d\hat{\sigma}}{d\hat{t}}(\hat{s},\hat{t}) \tag{1.3}$$

The sum is over all the subprocesses a+b→c+d which may vary according to the specific model used for the calculation.

In the early predictions (see for example Reference 9) the constituents a, b, c and d were supposed to be massless quarks and the scattering subprocess was expected to proceed via a vector gluon exchange. Then, from dimensional arguments, the functional dependence of the cross section should be:

$$\frac{d\hat{\sigma}}{d\hat{t}} \propto \frac{1}{s^{n/2}} \tag{1.4}$$

and:

$$E\frac{d^3\sigma}{dp^3} \propto \frac{1}{p_\perp^n} f(x_\perp,\theta) \tag{1.5}$$

where $x_\perp = 2\,p_\perp/\sqrt{s}$ and θ is the center of mass angle between the incident beam and the trigger hadron. For angles $\theta \simeq 90°$, $f(x_\perp, \theta) \to f(x_\perp)$. According to the dimensional counting rules[12,13] for large $x_\perp$ the function $f(x_\perp)$ is expected to take the form:

$$f(x_\perp) = (1-x_\perp)^m \tag{1.6}$$

where $m = 2n_s-1$, n_s being the number of non-interacting quarks. From purely dimensional arguments n (in Equation (1.5)) should be equal to 4 (see also the analogy with Equation (1.1)). Also according to the picture of Figure 2 at very high energy four distinct jets should emerge from the interaction point: two from the fragmentation of the scattered quarks and two from the remaining systems of the two incoming hadrons.

The first ISR and Fermilab results did exhibit approximate scaling in $x_\perp$. However n was far from 4: $n \simeq 8$ for pions and kaons and $n \simeq 10$-12 for protons[8].

Two models, both within the framework of the quark-parton model, were proposed to remedy this problem: 1) the "black box model"[14,15] proposed that, for some unknown reason, $d\hat{\sigma}/d\hat{t} \sim 1/st^3$ rather than $d\hat{\sigma}/d\hat{t} \sim 1/s^2$ which is expected from vector exchange. This leads to $p_\perp^{-8}$ in agreement with the observations. 2) In the Constituent Interchange Model (CIM)[16] it was argued that, in this kinematic region of $p_\perp$ between 2 and 8 GeV/c scattering processes of the form quark-meson and quark-diquark (see Figure 3) dominate the quark-

quark one. For such diagrams the predictions are that n=8 for pions and kaons and n=12 for baryons in good agreement with the experimental results[8].

In the last few years quantum chromodynamics (QCD), a field theory hoped to be the correct one for the strong interactions, was developed. Both the CIM and the "black box model" incorporated QCD ideas and were upgraded to the models described in Reference 17 and Reference 18 respectively (hereafter we will call Reference 17 CIM and Reference 18 FFF).

In the QCD approach the distribution and fragmentation functions (G's and D's in Equation (1.3)) are not only functions of the scaling variables x and z but also depend on Q^2. The choice of Q^2 is not unique. FFF for example uses:

$$Q^2 = \frac{2\,\hat{s}\,\hat{t}\,\hat{u}}{\hat{s}^2+\hat{t}^2+\hat{u}^2} \tag{1.7}$$

where $\hat{s}$, $\hat{t}$, $\hat{u}$ are the usual Mandelstam s, t, and u invariants but for the constituent subprocess. This uncertainty in the form for Q^2 makes predictions at low Q^2 (for $P_\perp$ up to ~2 GeV/c) uncertain. Also, from the experimental point of view, low $P_\perp$ events are dominated by decay fragments of resonances like ρ, φ, f, Δ etc[19].

The distribution functions are the same as measured in deep inelastic lepton and neutrino experiments. The quark fragmentation functions are the same as measured in e^+e^- annihilation into hadrons. The gluon fragmentation functions have not been measured and they have to be guessed. FFF for example assumed that $D_g^h(z) \sim (1-z)^2/z$.

According to QCD there are eight elementary subprocesses which contribute to the leading power law behavior. These are listed in Table 1. They have the general form:

$$\frac{d\hat{\sigma}}{d\hat{t}} = \pi \alpha_s^2(Q^2) \frac{|A|^2}{\hat{s}^2} \tag{1.8}$$

where $|A|^2$ have been calculated[20] for all first order QCD diagrams and are listed in Table 1. The strong coupling constant has the general form:

$$\alpha_s(Q^2) = \frac{12\pi}{(33-2n_f)\ln(Q^2/\Lambda^2)} \tag{1.9}$$

where $n_f = 4$ (the number of quark flavors). Although Λ may be process dependent its value is set in FFF equal to 0.4 GeV/c as determined in deep inelastic lepton scattering.

A QCD calculation in FFF of the invariant cross sections for the production of mesons with inclusion of only the first order diagrams leads to $n \approx 6$ (see Equation (1.5)) in the $2 \leq P_\perp \leq 10$ GeV/c region, still in disagreement with the experimental value $n=8$. This means that either the first order diagrams alone are not sufficient in the above $P_\perp$ region or that the theory is not correct.

In CIM higher order corrections to high $P_\perp$ processes are taken into account by the inclusion of CIM type (or higher twist in the QCD language) subprocesses of the form

$$q\ M \rightarrow q\ M \tag{1.10}$$

with subprocess cross section:

$$\frac{d\hat{\sigma}}{d\hat{t}} = \pi \alpha_M^2 \frac{1}{\hat{s}\,\hat{u}^3} \tag{1.11}$$

which yields the $P_\perp^{-8}$ dependence of the single particle distributions.

According to CIM subprocess (1.10) should dominate over the first order ones (see Table 1) in the $P_\perp \leq 10$ GeV/c region.

FFF argue that all the higher order terms can be approximated by assuming that the partons inside the colliding hadrons have some non-zero transverse momentum $K_\perp$. The same is valid in the fragmentation of partons into hadrons. This "primordial $K_\perp$", as it is called by R.D. Field, can also increase n from 6 to 8 in the $P_\perp \leq 10$ GeV/c region[21].

In both the CIM + QCD and the Field-Feynman-Fox + QCD models the first order diagrams dominate at really high $P_\perp$ leading to n=4. Recent results[22] from the ISR, in π° production, seem to confirm[23] that n does really approach 4 at high $P_\perp$ ($n \approx 5$ at $P_\perp \approx 15$ GeV/c, $x \approx 0.45$).

Here then was a situation where two models, the CIM and FFF, with fundamental structural differences in the $P_\perp \leq 10$ GeV/c region, were both in overall agreement with the pp data. This, of course, meant that at least one of the models was wrong.

The two models disagree drastically, however, in predictions in meson-nucleon scattering. One way then to distinguish the constituent-constituent scattering model from the CIM was to repeat the earlier experiments with a meson beam. This was done in this experiment where a π^- beam was used.

The CIM model predicted a rather high π^-/π^+ ratio (~10 at $P_\perp$= 4 GeV/c and at 90° in the CM frame) with a π^- beam. This is because of the inclusion of the subprocess of the form (1.10) (M here being π^-) which dominates for $P_\perp$ 10 GeV/c. FFF predicted that $\pi^-/\pi^+ \approx 1.5$ at the same $P_\perp$.

A major purpose of our experiment was to check which one of the above two predictions was correct. We found[24] that $\pi^-/\pi^+ \approx 1.2$

up to ~6 GeV/c $P_\perp$. The relevant data was analysed by J. Green and is presented in his thesis[25].

Therefore the CIM higher-twist contributions to large $P_\perp$ processes do not dominate in πp collisions. Although CIM agreed with the pp data, the interpretation is that CIM higher-twist terms may not dominate in the pp case either.

Since in this thesis we examine the angular and atomic weight dependence of long lived hadron production at high $P_\perp$, in the next two sections we discuss the experimental and theoretical status of these two topics.

Angular Dependence of Hadron Production at High $P_\perp$

The study of the angular dependence of hadron production at high $P_\perp$ is interesting because of the following reasons: a) A hadron produced at large $x_\perp = 2\,P_\perp/\sqrt{s}$, probably came from a valence quark of the colliding hadrons. If we assume that a hadron with large $x_\perp$ carries a large fraction of the scattered quark's momentum, then its direction should be close to that of the scattered quark. Therefore the measured angular dependence should reflect the angular dependence of the underlying hard-scattering process. b) The study of the angular dependence could provide information about the quark and gluon distribution and fragmentation functions (G's and D's for gluons in Equation (1.3)).

Two very different examples of possible angular dependences are: a) One in which all directions are the same, and only the distance to the kinematic limit matters. This would give an invariant cross section which scaled in x_R ($x_R = (x_\perp^2 + x_\parallel^2)^{1/2}$, $x_\parallel = 2P_\parallel/\sqrt{s}$). It was claimed[26] that this, so called radial scaling, fitted the data well. b) The elementary (parton) cross section $d\hat{\sigma}/d\hat{t}$ is approximately

independent of the angle (energy) and depends only on $P_\perp$, i.e., on the impact parameter of the parton-parton collision. This hypothesis, based on existed pp high $P_\perp$ data, was suggested by W. Furmanski and J. Wosiek[27,28]. The results of this experiment disprove this too (see Chapter IV).

In 1978 G. Donaldson et al.[29] published data from an FNAL experiment on the angular dependence of high $P_\perp$ inclusive π° production in $\pi^\pm p$ and pp interactions at 100 and 200 GeV. The main characteristics of their data were a wide plateau in the CM angular distribution and evidence for scaling in both πp and pp interactions. The $\pi^\pm p \to \pi^\circ X$ cross section fell less steeply with $x_\parallel = 2\, P_\parallel / \sqrt{s}$ and peaked at $x_\parallel$ = 0.14 in contrast to the $pp \to \pi^\circ X$ cross sections which peaked at $x_\parallel = 0$ and were, of course, symmetric around $x_\parallel = 0$ as we would expect (see Figure 4).

More data on the π° inclusive cross section in pp collisions (at the ISR) for CM production angles $\theta = 90°$ and $22° \geqslant \theta \geqslant 5°$ and at $\sqrt{s}$ = 23 and 53 GeV were published[30] in 1980. They found that the cross section is strongly dependent on both θ and $\sqrt{s}$ at small angles and therefore the hypothesis of radial scaling was incapable of incorporating both θ and $\sqrt{s}$ dependence of the cross section. They also found that their data were in qualitative agreement with the predictions of the FFF model (see Figure 5).

In our experiment it was the first time that a pion beam was used to measure the angular dependence of the long lived charged hadrons produced at high $P_\perp$. The FFF model predicted a strong dependence of the π^-/π^+ and K^-/K^+ ratios on the center of mass angle. Our results, described in Chapter IV, were somewhat surprising.

Atomic Weight Dependence

It has been observed in several experiments[31,32] that the invariant cross section per nucleus can be parameterized as:

$$\sigma = \sigma_0 A^{\alpha} \tag{1.14}$$

where σ_0 is the cross section per nucleon and A is the atomic weight.

At low $P_\perp$ the value $\alpha \approx 2/3$ is both observed experimentally and expected from the area of a black disk ($\sigma \propto R^2$ and $R \propto A^{1/3} \rightarrow \sigma \propto A^{2/3}$).

At high $P_\perp$ no nuclear shadowing is expected to occur[33]. If it is true that high $P_\perp$ events are produced by hard scattering processes involving partons, then for a given beam particle the invariant cross section should be proportional to the number of the target constituents; i.e., proportional to the number of target nucleons.

This means that, at high $P_\perp$, $\alpha = 1$ should be expected[33]. However the first FNAL data[7,8,34] on high $P_\perp$ inclusive hadron production from Be, Ti and W targets showed that the power α rose, for $P_\perp \geq 2$ GeV/c, to values of ~1.15 for $\pi^{\pm}$, ~1.2 for $K^{\pm}$ and ~1.3 for p and $\bar{p}$. This Chicago-Princeton group discovery of the anomalous A-dependence in high $P_\perp$ inclusive hadron production with proton beams has been confirmed by many other groups (see for example References 35, 36, 37 and 38). The anomalous nuclear enhancement is even stronger for jets. FNAL data[39] with proton and $\pi^{\pm}$ beams show α, for a symmetric pair of jets, rising to ~1.6 at $P_\perp \approx 6$ GeV/c.

Two reviews on A-dependence at high P are given in References 40 and 41.

Many explanations have been suggested for the anomalous A-dependence at high $P_\perp$. The fact that α is greater than 1 requires that the nucleons in the nucleus act collectively.

Two main classes of mechanisms that can produce such a collective effect have been proposed. The one is multiple scattering[33,42,43,44] of partons inside the nuclei. The second is a difference in the momentum distribution of the quarks in different nuclei with the consequent increase in probability that a quark can carry a substantial fraction of the momentum of the whole nucleus[45,46]. Fermi motion is just such an effect, but is not large enough to account for the data (see Reference 41 and references therein).

This Experiment (FNAL E258)

In this experiment we used a high intensity π^- beam to study high $P_\perp$ long-lived charged hadron ($\pi^\pm$, $K^\pm$, p and $\bar{p}$) production.

We took data with several beam energies at several center of mass angles and with hydrogen and nuclear targets so that we could study the transverse momentum and the energy dependence of the cross sections as well as their angular and their atomic weight dependence. Also we took data with a proton beam so that we could make a direct comparison of the cross sections with π^- and proton beams.

The results on the $P_\perp$ and $x_\perp$ dependence with the hydrogen target as well as the comparison between the π^- and proton beams are given in Reference 25.

In this thesis we describe the results on the angular dependence with the hydrogen target and π^- beam and the atomic weight dependence with the π^- beam.

In Chapter II we describe the detector and the data acquisition. Chapter III describes the data analysis and in Chapter IV we present and discuss the results.

CHAPTER II

DESCRIPTION OF THE APPARATUS AND THE PION BEAM

This experiment (FNAL E258) was the first experiment to use the High Intensity Pion Beam commissioned in the Proton West area at Fermilab in September 1978. The experiment (and a much simpler beam line) was proposed[47] in 1973 following a series of experiments investigating high transverse momentum interactions with proton beams by this same group. The properties of the High Intensity beam line and the details of the spectrometer are described below.

Proton West High Intensity Beam

Protons, accelerated to an energy of 400 GeV, were extracted from the main ring and transported to the Proton West beam line where they hit a one absorption length Be production target (see Figure 6). The intensity of the primary proton beam was measured by a Secondary Emission Monitor (SEM) a few feet in front of the production target. Typical proton beam intensities during the experiment were 5×10^{12} protons/pulse.

Figure 6 shows the arrangement of the elements of the high intensity beam during the period that E258 took data. The dipole magnet immediately after the production target selected the sign of the secondary beam and swept out from the beam channel all particles whose momenta differed from the beam momentum by more than ±40%. The

first quadrupole triplet took the flux emerging from the target box and, with the dipoles immediately downstream, formed a horizontally dispersed vertical focus at the position of the momentum slit.

The dispersion at the momentum slit was about 3mm/% and therefore one could, by varying the momentum slit horizontal aperture, change the momentum bite of the particles accepted at the end of the beam line from 0% (momentum slit completely closed) to 10% RMSFW (momentum slit completely open). The momentum slit was followed by three bends (consisting of 4 dipoles) and four quadrupoles which were set to alternating polarities to form a FODO channel. The three bends corrected the dispersion and the angle-momentum correlation. The FODO channel transmitted the beam to final focusing triplet. Chromatic aberrations are not corrected in this beam.

The FODO system was followed by a targeting triplet which focused the beam at the position of the experimental (E258) target. The horizontal and vertical trim dipoles, immediately after the final triplet, were used for horizontal and vertical target sweeps respectively (see page 25) and for positioning the beam at the target.

The elements indicated as SWIC at several positions along the beam line are Segmented Wire Ion Chambers. They were used to monitor the secondary beam profile, i.e., to check that the quality (shapes and widths) and the position of the beam were as they should be. Reference 48 gives a detailed description of the Proton West High Intensity beam as it was conceived, if not built.

The secondary beam in its present form can transport particles with energy up to 300 GeV.

Not shown in Figure 6 is a system of 4 additional dipole magnets, immediately upstream of the experimental target which was used during some parts of the running period to change the targeting angle of the incident beam by 16 mrad to the East or to the West (for details see Figure 17 and page 32).

By removing the production target primary protons could also be transported down the beam line to the experimental target. Data with 200 GeV primary protons were taken to normalize the data taken with this experiment to previous data taken with a proton beam by a similar spectrometer in the Proton East area. The proton-induced data also allowed a careful study of the systematics.

In Table 2 the primary and secondary beams, energies and spectrometer angles in the Lab and CM frames at which data was taken in this experiment are listed.

As indicated above, the intensity of the primary proton beam was measured by a Secondary Emission Monitor (SEM) a few feet in front of the production target, and the intensity of the secondary beam was measured by the two Ion Chambers IC710 and IC711/IC712 a few feet in front of the experimental target. Using the IC and SEM information we measured the π^-/proton yield of the secondary beam. These yeilds are given in Table 3. These yields are proportional to $x(1-x)^4$ where $x = \pi^-$ momentum/proton momentum. The experiment was run typically with 2-4 x 10^9 pions/pulse; 200 GeV proton runs were done with an intensity of 2-3 x 10^{10} protons/pulse.

The aperture of the momentum slit was wide open (3"x3") during all the running period of E258. This resulted in a momentum bite, at the experimental target, of 10% (RMSFW) (see Figure 7) and an acceptance

$\Delta\Omega$ $\Delta P/P$ of 110-μsr%. These numbers were found by the HALO Monte Carlo program[49]. The horizontal and vertical secondary beam widths, as measured with the SWIC five feet in front of the experimental target, are given in Table 3.

It should be noted here that the secondary beam particle composition was not measured by us. Particle compositions of similar beams, as measured by other groups[50,51] are given in Table 3. We see that, for these values of x, almost all of the beam is π^-'s. However, although throughout this dissertation I will be talking about a π^- secondary beam, it should be kept in mind that there is a small K^- and $\bar{p}$ contamination.

Because of the radio-frequency (RF) acceleration in the main ring the primary and secondary beam particles were grouped in "RF buckets" approximately 2 nsec wide and 18.8 nsec apart from each other. A spill monitor helped to check continually for "super-buckets" a source of increase in the number of accidentals, and to find the effective spill, or duty factor for each beam pulse. E258 took data with nominal spill lengths of .5, 1 and 1.5 sec. A typical value for the effective spill length was 65% of the spill length.

Beam Monitors

The area surrounding the experimental target is shown in more detail in Figure 8. A few feet in front of the experimental target we see the SWIC (SWIC710) with which we checked the position and the shape of the secondary beam, and the two Ion Chambers IC710 and IC711/IC712 with which we measured the beam flux.

The Ion Chambers were contained in a cylindrical aluminum tube 6" in diameter. They were fed by a mixture of 95% Ar, 5% CO_2, gas at

atmospheric pressure. The charge produced by the beam through ionization of the gas was collected by a capacitor and was digitized. The electrodes (anode and cathode) of IC710 were circular and 6" in diameter. The electrodes of IC711/IC712 were divided into two parts: the inside part (IC712) had a cross section equal to the cross section of the nuclear targets (1.25" x 0.75"), and the outside part (IC711) was the complement of the inside part to the IC710 electrodes. In this way the fraction of the beam that hit the nuclear targets could be measured by IC712.

At an angle of 90° in the Laboratory Frame and a distance from the target of 15' and 20' there were the East and the West 90° monitors respectively (see Figure 8). Each of them consisted of a telescope with three scintillator counters in it. The coincidences between these three counters were linear in the amount of beam that hit the target. The 90° monitors were used, together with the Ion Chambers, for the beam normalization of the nuclear targets.

The Magnetic Spectrometer

The spectrometer (Figure 9) consisted of a quadrupole doublet that took the flux of the particles produced around 80-mrad at the experimental target, and focused it at the end of the spectrometer (at the position of D7). The horizontal and vertical magnifications of this doublet were about 3 and 6 respectively at the end of the spectrometer. The doublet was followed by a dipole (a 16 mrad bend), which selected the sign and the momentum of the particles accepted by the spectrometer. Downstream of this dipole a set of two collimators and the neutral beam dump were used to stop all particles with momenta far from the central momentum of the spectrometer. These collimators

reduced the single rates enough in the downstream part of the spectrometer so that we could measure things there.

The downstream part of the spectrometer consisted of scintillator trigger counters (A1, A2,...A6) and a second dipole (with 16 mrad bend also) with drift chambers (D1, D2,...D7) on either side to measure the momentum of individual particles with high precision, and two Čerenkov counters ($\check{C}_A$, $\check{C}_B$) to separate pions from kaons from protons. At the end of the spectrometer there was a shower counter (ehμ) to separate muons from hadrons.

The dispersion of the two dipoles at the position of D7 was .6"/%.

The various elements of the spectrometer are described in detail below.

E258 Targets

E258 used a liquid hydrogen and three nuclear targets, Beryllium (Be), Copper (Cu) and Tungsten (W) so that the atomic weight dependence of the cross sections could be studied. The nuclear targets were rectangular 1.25" horizontally by 0.75" vertically. The hydrogen target consisted of a 20" long, 3" diameter stainless-steel flask, with side walls 0.003" thick, and with 0.001" thick hemispherical stainless-steel end windows. The hydrogen target is shown in Figure 10. In Table 4 a list of the targets, their lengths and some of their physical constants is given. The reason that two Be targets were used, a short and a long one, was to check the correction to the cross sections due to absorption in the targets.

The nuclear targets were mounted on a stage which moved remotely to bring the wanted target up to beam height.

The hydrogen target was mounted on a separate stage which moved the target into the beam line along a circular path.

Magnets

The two quadrupole magnets of the spectrometer were 4Q120 type quads[52]. They were 10' long. Their upstream faces were at a distance of 44.6' (the first one) and 56.6' (the second one) from the experimental target. The upstream one focused in the vertical plane and defocused in the horizontal plane and the downstream one focused in the horizontal plane and defocused in the vertical plane. The current of the upstream one was 20% higher than that of the downstream. Their different position and strength causes the difference in the horizontal and vertical magnifications at the end of the spectrometer as noted on page 18.

The two dipole magnets were 6-3-120 type dipoles[52]. They were also 10' long. Their upstream faces were at a distance of 68.6' and 175.6' downstream of the experimental target. They ran in series from the same power supply. Each of them bent the beam by 16 mrad to the East. The polarities and currents of all magnets were set remotely.

Collimators and Neutral Beam Dump

There were two steel collimators in the spectrometer: one vertical and one horizontal. They were used to stop all hadrons whose momenta were well off the momentum range accepted by the spectrometer. The apertures of both these collimators were wide open during all E258 runs: they were 4" by 4". Their length was 5' each.

These two collimators were followed by the neutral beam dump. It was used to stop neutral secondaries. It was made of concrete and steel. Its length was 9' and its aperture was 5" by 3".

Trigger Counters

The trigger consisted of a fourfold coincidence A1·A2·A3·A5. The four scintillation counters are shown in Figure 9. Scintillation counters A4, A6 in the same location as A5 but smaller in size, were not used during data taking. They were substituted for A5 in the trigger whenever there was need to reduce the momentum bite of the spectrometer (the size of the momentum bite was mainly determined by the size of either of A4, A5, A6 because the dispersion is largest at their location) for some systematic studies during the tune-up of the spectrometer. A1, A2 and A3 were 6.5" wide and 3.5" tall. A5 was 12" wide and 6" tall. All of them were 1/4" thick. Their high voltages were set so that they gave average pulses of 100 mV for minimum ionizing particles at the discriminator. The signal of each one of them was split into two. One pulse was integrated by an ADC and was written on magnetic tape whenever there was a trigger. The other passed through a discriminator whose threshold was -30 mV and output signal 7 nsec wide (this pulse was used for the trigger). The timing of trigger counters A1, A2 and A3 was the same to better than 1/2 nsec. Counter A5 was delayed by 2 nsec to determine the timing.

Čerenkov Counters

Particles were identified by the two Čerenkov counters ČA and ČB (see Figure 9). The length of ČA is 46'; and of ČB is 66'. They

both consist of a 1-ft.-diameter stainless steel tube with nonreflecting walls. The tube is bolted to a 6-ft.-long optics section. Each counter has two channels. The inner channel accepts light emitted at angles of 0 to 9 mrad and the outer one is sensitive to light emitted at angles of 9 to 40 mrad. The light is focused onto a 2" photomultiplier (RCA 31000M) in each channel. With a threshold requirement of 2 photoelectrons the counters are 99% efficient when the Čerenkov angle exceeds 3.5 mrad. Both CO_2 and He were used as gas fillings at pressures ranging from .5 to 5 atm. The gas pressure was measured with a precision transducer to 0.9%. The temperature was measured at several locations along the counter with a precision of 0.5° C. The counter walls were in thermal contact with a water jacket in which the water was continuously circulated so that the temperature of the gas was uniform within the measurement accuracy over the length of the counter.

For momenta larger than 20 GeV/c the pressures in the two counters were set so that K's produced a signal in the inner channel of ČA and π's produced a signal in the outer channel of ČA and in either the inner or the outer channel of ČB (see Figure 11). For momenta less than or equal to 20 GeV/c the pressures in the two counters were set so that K's produced a signal in CA and π's produced a signal in CB (see Figure 12). In both of the above modes p's or $\bar{p}$'s did not give any signal. They appeared as pedestals in the ADC's (see Figures 11 and 12).

Shower Counter

Electrons and muons directly produced in the target, are only about 10^{-4} of the produced hadrons[53]. This fraction is negligible.

However, a good fraction of the π's and K's decay into muons (for a momentum of 10 GeV/c 13% of the π's and 65% of the K's decay). The muons, of course, would appear as π's in the Cerenkov counters. To distinguish them from the hadrons a lead/lucite calorimeter (indicated as ehμ in Figure 9) was used at the end of the spectrometer (see Figure 13). It consisted of seven modules. The first module consisted of 18 layers of 1/4" lead alternating with 18 layers of 1/2" lucite, forming a depth of 30 radiation lengths or 1.4 absorption lengths. Each of the remaining six modules consisted of 20 layers of 1/4" lead alternating with 20 layers of 1/8" lucite. A cascade of particles, produced in the lead layers by the trigger particle, produced Čerenkov light at 45° as they passed through the lucite sheets. The light was focused by the lucite and guided by aluminized mylar light cones onto 58DVP photomultiplier tubes. The first module, designed to identify electrons, had six photomultipliers (each sampling three lead-lucite layers) and each of the remaining six modules had one photomultiplier. The photomultiplier signals were integrated by ADC's. The scintillator counters A7 and A8, in about the middle and the end of the identifier, were used for calibration purposes as described in the analysis chapter.

For a detailed discussion of the electron, hadron, muon identifer see Reference 54.

Drift Chambers

There were seven drift chambers (D1...D7, see Figure 9) in the E258 spectrometer. They were made at Princeton University. They were used to find the trajectory of each particle, determine its momen-

tum in conjunction with the second dipole magnet, and extrapolate the track through the upstream part of the spectrometer back to the target. Each of the chambers consisted of either one or two modules, each module containing two sense planes offset by half a cell. One of the two sense planes in each module had 7 and the other 8 wires, except in D7 where the one plane had 12 and the other 13 wires. The sense planes were 1/2" apart, and the drift space was 1/2". The sense wires were vertical (X wires) for half the planes and rotated through by 10° from the vertical (U wires) for the other planes. Table 5 contains a list of the E258 chambers.

The high voltage wires were at a negative potential of 3.8 KV. The sense wires were at 0 potential. As drift chamber gas an equal by volume mixture of Argon and C_2H_6 was used.

Typical drift chamber plane efficiencies were 98%, varying, from plane to plane, from a minimum value of 95% to a maximum of 99% (by plane efficiency we mean here the number of times that there was at least one hit at that plane for a certain number of triggers divided by the number of triggers). A detailed discussion of the drift chamber electronics is given in Reference 55 (however, the dead time of the E258 chambers was 200 nsec rather than the 100 nsec given in Reference 55). The measured drift velocity was 205 nsec/cm. The intrinsic spatial drift chamber resolution was measured at the M5 test beam at FNAL to be 150 μ (sigma) or 3.1 nsec. The time resolution, associated with the readout electronics was 4.5 nsec giving a total drift chamber resolution of 5.5 nsec or 260 μ (sigma).

Experimental Procedure

Before the start of a run, we positioned carefully the incident beam on the target. The position of the target stage, when a given target was set on the axis of the spectrometer, was determined before each running period by optical survey. The correct horizontal position of the beam on the target was verified by sweeping the beam across the target (the targets did not move in the horizontal plane) with a trim dipole magnet positioned about 100' in front of the target. By plotting the ratios: 1) the East and West 90° monitors to the ion chamber IC710, 2) the East 90° monitor to the West 90° monitor, 3) the number of triggers to the ion chamber IC710 and 4) the inner (IC712) to the outer (IC711) ion chambers as a function of the current in the horizontal trim dipole or, equivalently, versus the horizontal beam position as read by the SWIC in front of the target, we were able to determine the optimum horizontal beam position.

The targets could be moved remotely in the vertical direction. The correct vertical position of the beam on the target was verified by sweeping the beam across the target with a vertical trim dipole magnet and by moving the target vertically by small increments. The ratio of the difference of the counts of two identical scintillation counters, symmetrically positioned the one above and the other below the beam at the downstream end of the spectrometer, to the sum of their counts was recorded for each beam and target position. The optimum position was that for which the above ratio was zero.

Before each run the currents of the dipole and quadrupole magnets and the gas pressure of the Čerenkov counters were set carefully to the values corresponding to the selected momentum. Runs

with positive and negative polarity were taken in turn for a given momentum and target to minimize the systematic uncertainties in the particle/antiparticle ratios. Also runs with each of the nuclear targets were taken in turn for a given momentum to minimize the systematic uncertainties in the atomic weight dependence of the cross sections.

During any long running period we often would go back and take data at some fixed momentum to check the stability of the measured yields. The relative yields for a series of such runs, taken over a one month long running period, is shown in Figure 14. An estimated 5% systematic error has been added in quadrature to the statistical error of the relative yield. We see that the fluctuation of the points is within error.

Data Acquisition

The data were read out by a PDP-9 computer via CAMAC. Whenever a trigger occured the computer sent out a stop pulse and "froze" the drift chamber readout electronics. All the hits of each of the drift chamber wires during the 1.2 μsec time period before the trigger were read out. All this information as well as all the scalers and their accumulated values were written on magnetic tape for every pulse during the time between successive accelerator spills.

A diagram of the trigger electronics is shown in Figure 15. From this figure we see that, in a way, we had two experiments running in parallel. The one experiment used the beam pulse to gate all scalers whose counts were written on tape at the end of the pulse. In the second experiment the trigger pulse signalled the computer

which, if not busy, read and wrote on tape all the drift chamber and ADC information about that event. This information was used for the off-line analysis. The reason for having this arrangement is that the cross sections vary by about ten orders of magnitude throughout the transverse momentum range that we covered. The finite deadtime of the computer would limit statistics at low momentum - hence the scaler arrangement. At low $P_\perp$ ($P_\perp \leq 2$ GeV/c) the yield was very high and the fraction of events whose information was written by the computer on tape was small (at the 10 GeV/c spectrometer setting and with the tungsten target only about 10% of the events were written on tape). These events are called strobes. At high $P_\perp$ ($P_\perp \geq 3$ GeV/c) the yield was low and the number of strobes was equal to the number of triggers.

The computer deadtime varied from 10 msec to 15 msec/event so that the maximum number of events that were written on tape varied from 60 to 100 per (1 sec spill) pulse. Various on-line display programs supplied a continuous monitoring of the operation of the apparatus. Other data, such as magnet currents, Čerenkov pressures and temperatures were continuously monitored and recorded by the computer.

CHAPTER III

DATA ANALYSIS

The goal of the data analysis was to determine the invariant cross section versus the transverse momentum $P_\perp$ for the inclusive production of each one of the long lived hadrons $\pi^\pm$, $K^\pm$, p and $\bar{p}$ in π^--N collisions.

These cross sections have a very strong $P_\perp$ dependence; they decrease by about one order of magnitude for each 1 GeV/c increase in $P_\perp$. This means that an accurate knowledge of the transverse momentum scale was required. Also a very accurate determination of the momentum acceptance of the spectrometer was crucial.

The invariant cross section is given by the expression:

$$E\frac{d^3\sigma_i}{dP^3} = \frac{dN^{pr}}{N_0\, e^{-L/\lambda_i}\left(\frac{\lambda_b\lambda_i}{L|\lambda_b-\lambda_i|}\right)\left(1-e^{(L/\lambda_b\lambda_i)|\lambda_b-\lambda_i|}\right)\frac{\rho N_A L}{A}}\;\frac{E}{P^3 d\Omega\frac{dP}{P}} \qquad (3.1)$$

where:

dN^{pr} is the number of particles of type i produced into the phase space $d\Omega dP/P$

E, P are the energy and momentum of the produced particles

N_0 is the number of beam particles that hit the target

λ_b is the absorption length of the beam particles in the target

λ_i is the absorption length of particles i in the target

ρ, L, A are the density, length and atomic weight of the target, respectively

N_A is Avogadro's number

The transverse momentum point to which the invariant cross section, given by Equation (3.1), corresponds is:

$$P_\perp = P \sin\theta \simeq P\theta$$

where θ is the angle between the incident beam and the direction of the produced particles.

If we define a quantity N_b^t which depends only on properties of the beam and the target

$$N_b^t \equiv N_0 e^{-L/\lambda_i} \left(\frac{\lambda_b \lambda_i}{L\,|\lambda_b - \lambda_i|} \right) \left(1 - e^{(L/\lambda_b \lambda_i)\,|\lambda_b - \lambda_i|} \right) \frac{\rho N_A L}{A} \tag{3.2}$$

and we make the approximation that $E \approx P$ for all momenta at which the experiment took data (the smallest momentum was 10 GeV/c) we can write Equation (3.1) in the form:

$$E \frac{d^3\sigma_i}{dP^3} = \frac{dN^{pr}}{N_b^t} \frac{1}{P^2\, d\Omega\, dP/P}$$

If we multiply and divide the right hand side by dN^{ac}, the above formula takes the form:

$$E \frac{d^3\sigma_i}{dP^3} = \frac{dN^{ac}}{N_b^t} \frac{1}{P^2 \frac{dN^{ac}}{dN^{pr}}\, d\Omega\, dP/P} \tag{3.3}$$

where dN^{ac} is the number of particles i of momentum P and angle θ that would be accepted by a spectrometer of infinitesimal acceptance.

In the real world, of course, all spectrometers accept a finite number of particles N^{ac} over some finite solid angle $\Delta\Omega$, and a finite momentum bite $\Delta P/P_0$, where P_0 is the central momentum of the spectrometer. We can approximate the invariant cross section at transverse momentum $P_{\perp 0} = P_0\theta$ in terms of finite quantities as:

$$E\frac{d\sigma_i}{dP^3} \approx \frac{N^{ac}}{N_b^t}\,\frac{1}{P_o^2\,Acc} \qquad (3.4)$$

where $Acc \equiv N^{ac}/N^{pr}\Delta\Omega\Delta P/P_o$ is the integrated acceptance of the spectrometer. The right hand side of Equation (3.4) gives only an approximate estimation of the invariant cross section at $P_{\perp o} = P_o\theta$, because the average transverse momentum $\langle P_\perp \rangle$ of the particles N^{ac} is not necessarily equal to $P_o\theta$ nor is their average momentum $\langle P \rangle$ equal to P_o. If we insist that we want to assign the number of the right hand side of Equation (3.4) to the invariant cross section at $P_\perp = P_o\theta$ we have to apply some correction (slope correction) as discussed in detail on page 49. We also note that in an experiment we do not measure N^{ac} directly but some number of events N^{ev}.

It will be our task in this chapter to describe how we can deduce the quantities in the right hand side of Equation (3.4) from quantities measured during the experiment. In the first section we describe how we determined the transverse momentum scale. The second section describes the reconstruction program and the determination of the yield (N^{ac} in Equation (3.4)). In the third section we discuss the Monte Carlo and the determination of the acceptance of the spectrometer. The fourth section describes how the beam normalization was done and finally we discuss the backgrounds, some special problems with the analysis and the errors to the cross sections.

Transverse Momentum Scale

As pointed out on page 29 the transverse momentum $P_\perp$ at which we intend to plot the invariant cross section for a given spectrometer momentum P_o is given by:

$$P_{\perp o} = P_o \theta$$

where θ was the angle between the incident beam and the spectrometer. Because the cross sections for the processes that we study here, depend very strongly on $P_\perp$, a knowledge of the transverse momentum scale to ~1% is important. This means that we had to measure very carefully P_o and θ. In the following two sections we describe how we did that.

Momentum Calibration

The momentum scale P_o of the spectrometer was calibrated as follows: We set the current in the two dipole magnets at some value I. We also substituted counter A6 for counter A5 in the trigger (see Figure 9 and page 21). Counter A6 had much smaller dimensions and restricted the momentum bite of the particles that triggered the spectrometer to a vlaue less than ±1%. Then two pressure curves, one for each Čerenkov counter, were taken in the pressure range where kaons at the spectrometer momentum produced Čerenkov light near the 9 mrad boundary between the inner channel and the outer channel. Precise knowledge of the geometry of the optical system and the index of refraction of He, which has a very low dispersion, permits an accurate calibration of the beam momentum. Figure 16 shows the efficiencies $\frac{\check{C}A1.T}{T}$ and $\frac{\check{C}A2.T}{T}$ of the inner (ČA1) and the outer (ČA2) channels of the first Cerenkov counter in the region where the kaon light moves across the 9 mrad boundary as the index of refraction η is varied. In terms of the extrapolated indices of refraction, shown in Figure 16, the momentum of the kaons is given by:

$$P_o = \sqrt{\frac{m_K^2}{(n-1)_1 + (n-1)_2 - \theta^2}}$$

where m_K is the kaon mass, θ is the boundary angle between the two channels, and $(n-1)_1$ and $(n-1)_2$ are the extrapolated indices of refraction for the inner and outer channels respectively. With $\theta^2 = (81\pm3) \times 10^{-6}$ we find $P_{01} = (27.3\pm0.2)$ GeV/c. A similar curve for the second Čerenkov counter gave $P_{02} = (27.5\pm0.2)$ GeV/c. We thus take the momentum P_0 corresponding to the dipole current I to be (27.4±0.14) GeV/c. To find what current was needed for any other momentum we used the 6-3-120 dipole transfer constants of Reference 56 normalized of course to our Čerenkov measurement. The magnet current, as monitored by the computer, is known with an accuracy of ±1%. We thus know the momentum scale P_0 to ±1.1%.

Angle Between the Incident Beam and the Spectrometer

The angle θ between the unpitched beam and the spectrometer was 80 mrad. This number was obtained by surveying the spectrometer and is known to an accuracy of about ±.3% (its accuracy is limited by how well we know the direction of the incident beam).

As indicated on page 16 the targeting angle of the incident beam was changed by some amount θ_{pitch} to the East or to the West. To accomplish this a system of four dipole magnets (EPB dipoles) was employed as pitching magnets. Figure 17 shows how the beam was pitched to the West resulting in an angle θ = 80 mrad + θ_{pitch}. To pitch the beam to the East the polarity of the most upstream pitching magnet was reversed and the horizontal trim magnet and the three downstream pitching magnets were moved to their image positions with respect to the unpitched beam and, of course, their polarities were also reversed. In this case it was θ = 80 mrad - θ_{pitch}.

The angle θ_{pitch} was found by the following two methods: 1) From the transfer constants of the EPB dipoles that were used to pitch the beam taken from Reference 57. 2) From the horizontal offset h of the beam at the position of the SWIC in front of the target and the distance d of this SWIC from the target (see Figure 17). The pitching angle is $\theta_{pitch} = \arctan \frac{h}{d}$.

Methods (1) and (2) gave the same answer within error. The pitching angles for both cases (pitching the beam to the East or to the West) were found to be (16.3±.5) mrad. Therefore the angle θ was (96.3±.55) mrad when the beam was pitched to the West and (63.7±.55) mrad when the beam was pitched to the East (see also Table 2).

In conclusion the transverse momentum scale is known with an accuracy of ±1.1%, ±1.2% and ±1.4% when the beam is unpitched, pitched to the West and pitched to the East respectively.

Yield Determination

The yield determination (N^{ac} in Equation (3.4)) proceeded in the following three steps: a) We used the drift chamber information to find out which of the events that were written on tape had tracks that reconstructed. b) All possible tracks for each reconstructed event were refitted and the best track was chosen. Then the Čerenkov counter and the ehμ information was used to identify the particles as protons, pions, kaons and muons. c) Several corrections were applied on the yield of each particle: decay in flight in the case of π's and K's, absorption from material in the experimental target and the spectrometer, etc. Each one of the above three steps is described in detail below.

Reconstruction Program

A program was written that read the primary data tapes and searched for events whose tracks reconstructed. Reconstructed events were accepted and written on secondary tapes called DST tapes (Data Summary Tapes). The cuts at this stage were chosen to be very loose so as not to exclude any possibly good data.

First, for every event, the reconstruction program read the times of the hits of the wires that fired and converted them to space (X and U) coordinates. To do that the program needed the drift velocity of the electrons in the chambers. This drift velocity was calculated from the size of the drift chamber cell and the time that the electrons took to drift from the one edge of the cell to the other (this was obtained directly by the program from the data). Then the program required that: 1) there was at least one hit on one of the X-wires (from now on called an X-hit) of D1 or D2 and there was at least one more X-hit on D3 or D4 and 2) there were at least one X-hit on two out of the three D5, D6 and D7 chambers and 3) there was at least one hit on U-wires (from now on called U-hits) on three out of the five D1, D2, D3, D6, and D7 chambers. Conditions 1, 2 and 3 are the least number of requirements needed for an event to have a reconstructable track upstream and downstream of the 2nd bend.

In the second step the program fitted the upstream and downstream X-tracks to straight lines and required that the chisquares per degree of freedom (χ^2/DOF) of at least one upstream and one downstream X-track (there might be more than one pair of upstream and downstream tracks) was less than or equal to 15. Then the program required that there was at least one pair of upstream and downstream

X-tracks whose difference in the X-positions, ΔX, at the middle of the second dipole was between -.3" and .3" (see Figure 18).

Third the program checked if there was at least one U-track whose hits were compatible with at least one accepted X-track. Then, from the X and U-hits, it calculated the Y coordinates and fitted them to a straight line and required that there was at least one Y-track whose fit had a χ^2/DOF of less than or equal to 12.5.

The reconstruction program efficiency was about 94% at 25 GeV/c. We explain on page 39 how we calculated this number.

DST Program - Data Cuts

A second program (from now on called the DST program) read the DST tapes and, for each event, found the track with the best fit. The program also determined the particle type and applied some cuts on the data.

The DST program first calculated the momentum for each pair of upstream and downstream X-tracks. The momentum was calculated from the measured bend angle in the second bend magnet as $P=P_0/(1-\Delta\theta/\theta_0)$ where P_0 was the central momentum of the spectrometer, θ_0 = 16 mrad and $\Delta\theta=\theta_0-\theta$, where θ was the angle between the upstream and downstream X-tracks. The program then made global X and Y fits to all possible tracks and chose the track with the smallest sum of the X and Y chisquares (χ_x^2/DOF+χ_y^2/DOF).

Particle identification followed. The program first checked if the event was a muon. Using the ehμ information it calculated the quantity:

$$\chi^2 = \sum_{j=1}^{6} \left(\frac{X_j - \bar{X}_j}{\sigma_j}\right)^2 + \sum_{i=1}^{6} \left[\left(\frac{X_i - \bar{X}_i}{\sigma_i}\right)^2 + C\right] \qquad (3.5)$$

where:

X_j is the ADC signal from counter j of the first module

$\bar{X}_j$, σ_j are the average signal and the standard deviation of the distribution of minimum ionizing particles of counter j of the first module

X_i, $\bar{X}_i$, σ_i are similar quantities for the remaining six modules

C = 1 if X_i = pedestal of counter i

= 0 if X_i pedestal of counter i

The inclusion of the constant C improved the separation of muons from hadrons. The determination of $\bar{X}_j$, σ_j, $\bar{X}_i$ and σ_i was done during the calibration of the apparatus. A sample of minimum ionizing particles (muons in this case) was selected by requiring minimum ionizing signals in both A7 and A8 counters (see Figure 13).

From Equation (3.5) we expect muons, as minimum ionizing particles, to have much smaller χ^2 than hadrons which will tend to give large signals in the early counters and small, if at all, in the later counters. A χ^2 distribution for a 25 GeV/c run is shown in Figure 19. Making a cut at χ^2 = 10 we separated hadrons from muons.

The fraction of muons per pion as a function of momentum is given in Table 6.

The contamination of the hadron sample by muons is no more than 10% of the amount of muons and therefore less than 1% of the pions for all spectrometer momenta.

If the particle was identified as a hadron by the ehμ the program used the Čerenkov counter information to determine if it was a π, K, or p. The sums ČA and ČB of the ADC counts of the inner and outer channels for the two Cerenkov counters were calculated (ČA = ČA1 + ČA2, ČB = ČB1 + ČB2). For spectrometer momenta larger than or equal to

20 GeV/c pions were defined as events with ČA>30 and ČB>30, kaons as events with ČA>30 and ČB≤30 and protons as events with ČA≤30 and ČB≤30 (see Figure 11). Events with ČB>30 and ČA≤30, indicated as errors in Figure 11 were rejected by the program. For spectrometer momenta of 10 and 15 GeV/c the pions did not produce a signal in the upstream Čerenkov (page 22). In this case pions were defined as events with ČB>30 (see Figure 12).

The next step of the DST program was to apply cuts on each event and to decide whether to accept the event.

The first cut required that $\chi_x^2/DOF<11$ and $\chi_y^2/DOF<11$. X and Y chisquared distributions for 25 GeV/c runs are shown in Figure 20.

The next five cuts required that the track passed through the apertures of D7 and both dipoles and quadrupoles.

The seventh cut required that the ADC reading of trigger counter A5 was more than or equal to 50. This cut eliminated triggers caused by Čerenkov light in the lucite light guide of A5.

The eighth cut was on $\Delta P/P_0 = (P-P_0)/P_0$ where P was the measured momentum of the event and P_0 the central momentum. The cut required that $-.15 \leq \Delta P/P_0 \leq .2$. A $\Delta P/P_0$ distribution for a 25 GeV/c run is shown in Figure 21.

The final cut was on the position of the track at the target (see Figure 22). The aperture and target cuts are listed in Table 7.

At the end of each data run the DST program wrote on a disk file the number of particles of each type that were accepted, the scaler totals, the beam momentum, the target type, the spectrometer momentum, the number of absorption lengths of gas in the Čerenkov counters and the East and West 90° monitor counts corrected for accidentals. This information was used by a third program to calculate cross sections.

Analysis of Low Momentum Runs

In Figure 23 the ratio of the number of reconstructed events to the number of strobes versus the spectrometer momentum is shown for a number of randomly chosen runs with 200 GeV π^- beam (pitched to the West) and with the tungsten (W) target. By strobes we mean the events that were written on the magnetic tapes. No DST cuts were applied on the reconstructed events.

At momenta $\geq$40 GeV/c the rates were low, and a lot of the triggers were accidentals and they did not reconstruct. The drift chamber information plus the DST cuts were essential in rejecting the accidentals in this momentum range.

At intermediate (25 and 30 GeV/c) and low (10, 15 and 20 GeV/c) momenta the fraction F of triggers that were accidentals was very small. The number of accidentals was measured by scaling the coincidence between the four trigger counters A1, A2, A3, A5 where the signal of A1 was delayed by 1RF bucket (18.8 nsec) with respect to the other three. The fraction F was ~.5% at 25 and 30 GeV/c and only ~.1% at 10, 15 and 20 GeV/c. On the other hand at low momenta the multiple scattering is large resulting in the loss (because of the reconstruction technique and not because they scattered out of the detector) of a large fraction of events (see Figure 23). For these reasons we did the following:

For momenta $\leq$20 GeV/c we did not use the method of analysis described in page 35 (reconstruction method). We assumed that all triggers recorded by the scalers were good events. We still however used the fraction of events that were reconstructed to find the particle ratios. These ratios were checked and found to be equal (as expected)

to the ones obtained directly from the scaler information (see page 27). We called this method of analysis the scalers method.

Scalers and reconstruction methods gave the same cross sections at 25 GeV/c within ±2%.

Corrections to the Particle Yields

A number of corrections were applied on the yield of each particle. They are discussed in detail below in the order that were actually made:

1) Reconstruction Program Inefficiency

To find the reconstruction inefficiency we assumed that all strobes were good events at 25 GeV/c and therefore they should all reconstruct (except, of course, the small fraction of the accidentals A(1)235/A1235). Then we calculated the average efficiency ε=(number of reconstructed events/number of strobes) over several ±25 GeV/c runs throughout all the running period of the experiment. We found ε=.94±.02 and therefore the inefficiency was $1-\varepsilon$=6%±2%. A further assumption was made that the inefficiency stayed constant for momenta >25 GeV/c. Only the data that were analyzed with the reconstruction method were corrected for reconstruction program inefficiency.

2) Computer Dead Time

The correction because of computer dead time was easily done by multiplying the yield of each particle for a given run by the ratio (number of triggers/number of strobes) (triggers≡number of A1·A2·A3·A5 coincidences; strobes≡number of triggers written on tape) for that run. This correction was done also only for data that were analyzed with the reconstruction method.

3) Kaon Misidentification

At momentum settings of 10, 20, 25 and 30 GeV/c the Čerenkov angle of some of the kaons with momenta at the low end of the momentum acceptance of the spectrometer was below threshold in the upstream Čerenkov counter ČA. This resulted in some fraction of kaons being misidentified as protons. By studying some high statistics runs at these momenta with fine momentum binning, we found that 8%, 2%, 1% and 0% of the kaons were mistagged as protons at momenta 10, 20, 25 and 30 GeV/c respectively and we corrected the number of kaons and protons correspondingly.

A similar problem appeared at the high momentum side of the momentum acceptance at spectrometer settings of 70, 75, 80 and 90 GeV/c. There some fraction of the kaons did produce Čerenkov light in the downstream Čerenkov counter ČB, and were misidentified as pions. Unfortunately, very poor statistics at these high momenta did not permit a similar analysis like the one described above. A rough estimate of the fraction of kaons that were misidentified as pions at these momenta was ~6% of the total number of kaons. Because of the big uncertainty (~100%) in this estimate we decided to add it in the systematic error rather than correcting the pion and kaon yields for it. This correction (6%) is much smaller than the statistical errors at these high momenta.

4) Empty Target Subtraction

The walls of the hydrogen target box contributed significantly to the hydrogen target yields. The empty target contributions were measured directly by runs that were done at all momentum settings with the hydrogen target empty. They are listed in Table 8. We notice

that the contributions for particle and antiparticle are the same. The increase of the contribution as the momentum increases is explained by the fact that the steel walls contribute more due to the strong dependence of the cross sections on the atomic weight of the target.

5) Correction for π, K Decay in Flight

To correct for π, K decay in flight we multiplied their yields by $\exp(L/\lambda)$, where L = 258.7' was the spectrometer length (from the target up to the shower counter) and λ was the π or K decay length respectively (the whole spectrometer length was used for L because all muons are subtracted from the hadron sample using the shower counter information). λ was calculated using the formula:

$$\lambda = \frac{P_o}{M} c \tau$$

where:

P_o was the central momentum of the spectrometer, M the π or K mass, τ the π or K lifetime and c the velocity of the light.

The decay in flight correction was 13% and 65% for pions and kaons respectively at 10 GeV/c momentum and 3.5% and 23% for pions and kaons respectively at 40 GeV/c momentum.

6) Correction for Absorption by Material in the Spectrometer

The number of absorption lengths[58] λ_c of gas in the Čerenkov counters versus momentum is given in Table 9.

The number of absorption lengths λ_{sp} for all other material in the spectrometer for each particle type is given in Table 10. The absorption cross sections were obtained from Reference 59.

To correct for absorption we multiplied the yield of each particle by $1/\exp[-(\lambda_c+\lambda_{sp})]$. This factor was ~20% at 10 GeV/c and ~10% at 40 GeV/c momentum setting.

7) Correction for Absorption in the Experimental Target

The target absorption is actually contained in N_b^t (see Equation (3.2), page 29). It can be proved that an equivalent expression for N_b^t is:

$$N_b^t = N_0 \left(1 - e^{-L/\lambda_b}\right) \frac{\rho N_A \lambda_b}{A} \left(1 - F_i\right) \qquad (3.6)$$

where:

F_i is the fraction of particles of type i that were absorbed in the target. The F_i's were calculated directly from the absorption lengths, λ_i's, and the target lengths and they were also found by a Monte Carlo program where the exact beam-target geometry and the beam and target sizes were taken into account. The two methods agreed within 1%. The F_i's, of course, depended on the λ_i's of Equation (3.2). The absorption lengths λ_i were calculated from the atomic weight A of the target, the target density ρ, the Avogadro's number N_A and the absorption cross section σ_i for the particle of type i and for a given target through the formula:

$$\lambda_i = \frac{A}{\sigma_i N_A \rho} \qquad (3.7)$$

The absorption cross sections σ_i were obtained from References 32, 58, 59, 60, 61, 62 and 63.

In Table 11 we list the F_i's for all particle types and targets. The momentum dependence of the F_i's in the momentum region 10→90 Gev/c that we took data is small (~2%). Their values given in Table 11 are the averages over momentum.

The agreement of the cross sections at ±25 GeV/c between the long and short Be targets (see Table 4) was better than ±5% (consistent with the overall systematic error). This is a good indication that the target absorption was done correctly.

We note that all the above corrections are very much the same for particle and antiparticle. This fact gives the unique capability to this kind of experiment to measure the particle/antiparticle ratios simply by doing two runs at the same momentum but opposite magnet polarities, normalizing the yields to the same number or incident beam particles and using the Cerenkov counter information to find the particle, antiparticle yields and take their ratio.

Acceptance

We defined as the integrated acceptance, Acc, of the spectrometer the quantity (see page 30):

$$A_{cc} \equiv \frac{N^{ac}}{N^{pr}} \Delta\Omega \frac{\Delta P}{P_0} \tag{3.8}$$

It tells us what fraction of the particles that were produced in the solid angle $\Delta\Omega$ and with momenta between P_0 and $P_0+\Delta P$ will be accepted by the spectrometer.

There is not really any way to measure Acc directly. To determine it we had to use a Monte Carlo program which is described in detail below.

Monte Carlo

The Monte Carlo program originated trajectories at the front of the experimental target. The X, Y distributions of their vertices

were consistent with the horizontal, vertical profiles of the secondary beam as read off by the SWIC in front of the target (SC710 in Figure 8). Such a pair of SC710 horizontal and vertical beam profiles for the 200 GeV π^- beam pitched to the West is shown in Figure 24.

Interaction points were chosen according to an exponential law $(1-\exp^{-z/\lambda_b})$ where λ_b was the absorption length of the beam particles in the target. The program checked if the interaction point (x, y, z) was in the volume of the target.

Secondary particles were produced at the interaction points with angles $\theta_o-\Delta\theta_x \leq \theta_x \leq \theta_o+\Delta\theta_x$ (where θ_o was the angle between the beam and the spectrometer), $-\Delta\theta_y \leq \theta_y \leq \Delta\theta_y$ and momenta $P_o-\Delta P_- \leq P \leq P_o+\Delta P_+$.

Special care was taken to make sure that $\Delta\theta_x$, $\Delta\theta_y$ and ΔP_-, ΔP_+ were large enough to cover the angle and momentum acceptance of the spectrometer. For this we found that $\Delta\theta_x$=8 mrad, $\Delta\theta_y$=6 mrad, $\Delta P_-/P_o$=0.2, and $\Delta P_+/P_o$=0.3 were large enough values for all but the tungsten targets. For the tungsten target the multiple scattering was bigger and some trajectories that started out even with bigger $\Delta\theta_x$ and $\Delta\theta_y$ could be scattered in and still be accepted. We used $\Delta\theta_x$=12 mrad, $\Delta\theta_y$=9 mrad for the tungsten target.

The secondaries were produced with flat distributions in θ_x and θ_y and either a flat distribution or a distribution of the form $P_\perp \exp(-\alpha P_\perp)$ (where α was constant) in $P_\perp$.

A flat distribution in $P_\perp$ was used when we wanted to find the integrated acceptance of the spectrometer (as it is explained below) and the distribution of the form $P_\perp \exp(-\alpha P_\perp)$ was used (this is a good approximation to the local dependence of the cross section on $P_\perp$; see page 51) when we wanted to compare Monte Carlo with data distributions.

The secondaries were traced through the spectrometer. They were multiple scattered everywhere they went through material such as the experimental target, trigger counters, windows and gas of the Čerenkov counters, etc.

The X, Y coordinates of the tracks at the positions of all drift chambers, the target, and the magnets were recorded on magnetic tape. The production angles θ_x and θ_y and the momentum P and the smeared positions of the tracks at the position of the drift chambers were also recorded on tape. Smearing was done with a Gaussian distribution with sigma = 260 μ (for the X coordinate) and sigma = 260/sin 10° = 1497 μ (for the Y coordinate).

The Monte Carlo tapes were later analyzed with the same DST program that was used for the data.

We first made sure that the Monte Carlo program reproduced the data distributions rather well.

To check the shape of the momentum acceptance of the spectrometer we did the following: we took three runs with the same target and with the central momentum of the spectrometer shifted by small amounts as shown in Figure 25. In Figure 25 we have plotted the acceptance of the spectrometer for each momentum bin versus momentum as calculated by the Monte Carlo program.

Monte Carlo events were produced with a flat distribution in P. Each momentum bin was 2% of the central momentum P_0. P_0 was 25, 27.5 and 30 GeV/c: i.e., the same as the spectrometer settings of the three special runs. From Figure 25 we see that there is an overlapping, in the momentum acceptance, between the three runs and that the bin acceptances of two such runs differ at some momenta by as much as

a factor of 50. The number of particles, accepted in each run, was normalized to the same incident beam flux and was then binned in the same momentum bins as the ones used to calculate the bin-by-bin acceptance. If ΔN_i^j was the number of particles in momentum bin i and for the run j (j = 1, 2, 3 for the 25, 27.5, 30 GeV/c run respectively), and A_i^j was the corresponding acceptance, then according to Equation (3.3) the invariant cross section at momentum P (corresponding to momentum bin i) should be:

$$E \frac{d^3\sigma}{dP^3} = C \frac{\Delta N_i^j}{P P_o^j A_i^j} \tag{3.9}$$

Here C is a constant which is the same for all i and j and P_0^j is the central momentum for run j. It should be noted here that the reason that we can use Equation (3.3) to calculate the invariant cross section and not worry about correcting it (slope correction) as pointed out on page 30 is because the momentum bins i are rather small (only 2% of P_0). The right hand side of Equation (3.9) divided by C is plotted against the momentum in Figure 26. We see that the cross sections calculated even at very different points of the momentum acceptance of the spectrometer but, of course, at the same momentum agree adequately. It should be noted that the errors in Figure 26 are only statistical.

The matching of the three overlapping runs guaranteed that we had found the right momentum acceptance. Finding the right momentum acceptance was a tedious job. It required that we give the Monte Carlo program the right beam profile and target position, that the magnet transfer constants and positions were correct etc. The three overlapping runs served as a guide and provided a severe test that what we did was correct.

During the data runs the beam had a small horizontal offset h from the center of the target. This was because the acceptance of the spectrometer had a maximum at a non zero h. h was different for the different running periods (for example it was different for the unpitched, pitched to the East and pitched to the West beams). There was no vertical beam offset.

Because the acceptance depended on h we had to find h. To find h we did a series of Monte Carlo runs varying h by small increments from run to run (this was somewhat similar to the horizontal target sweeps described in Chapter II, page 25). In these runs particles were produced with a spectrum $\frac{dN}{dP_\perp} \propto P_\perp \; e^{-\alpha P_\perp}$. The constant α was the local slope of the yield versus momentum curve at the neighborhood of $P_{\perp o}$, where $P_{\perp o}$ was the transverse momentum corresponding to the central momentum P_o. As P_o's for these runs, 25 GeV/c and 30 GeV/c were chosen. Monte Carlo and data distributions were compared for each such run. Distributions whose shapes and averages are very sensitive in h are the horizontal distribution of the particles accepted by the spectrometer at D7 and, of course, the horizontal target distribution. We therefore chose as h the one of that run whose horizontal distributions at D7 and at the target were closest to the data. The h values, found with the above method, were consistent with the SC710 readings. This exercise, called horizontal alignment, was done for every running period and separately for the hydrogen and the nuclear targets.

The θ_x (horizontal reconstructed angle) and θ_y (verticle reconstructed angle) acceptances of the spectrometer, as found by the Monte Carlo program, are shown in Figure 27. We note that the θ_y acceptance

is broader than the θ_x. This is a result of the fact that the first quadrupole was vertically focusing.

In Figure 28 a comparison between data and Monte Carlo horizontal position at the target, horizontal position at D7 and $\Delta P/P_0$ distributions is made for a 30 GeV/c run with the hydrogen target. The agreement is acceptable.

After we had made sure that the Monte Carlo program reproduced the data, we proceeded to find the integrated acceptances for each target and for each running period. We can express Acc in terms of $\Delta\theta_x$, $\Delta\theta_y$, ΔP_- and ΔP_+ in the form

$$Acc = \frac{N^{ac}}{N^{pr}} \left(4\,\Delta\theta_x\,\Delta\theta_y\right) \frac{(\Delta P_- + \Delta P_+)}{P_0} \tag{3.10}$$

It was found that Acc was the same for all nuclear targets for a given running period and at fixed momentum. The values are given in Table 12. The ±1% error is statistical only. No DST cuts were applied at 10, 15 and 20 GeV/c. The 300 GeV π^- beam acceptances are slightly higher than the 200 GeV π^- beam ones because the 300 GeV beam was narrower.

In Figure 29 the nuclear target integrated acceptance is plotted versus momentum. All DST cuts were applied. The 10, 15 and 20 GeV/c acceptances without any DST cuts are also shown. These acceptances were used in the scalers method of analysis (see page 38). The decrease of the acceptance at low momenta is due to the multiple scattering. We notice however that the multiple scattering does not have any effect for momenta $\geq$ 25 GeV/c.

The integrated acceptances for the hydrogen target are listed in Table 13.

The overall systematic uncertainty in Acc, mostly because of uncertainties in h, was estimated to be ±3%.

In Figure 30 the momentum resolution of the spectrometer versus the momentum is shown. A δ-function momentum distribution was produced by the Monte Carlo program at each run. We see again that at low momenta (10, 15 and 20 GeV/c) the multiple scattering dominates (the resolution falls like 1/P at this region). At momenta $\geq$ 30 GeV/c the multiple scattering has died out and the resolution is constant and ~±1%. This value is what we expect from the 260 μ (sigma) drift chamber resolution for the X-coordinate.

Slope Correction

This correction is associated with the finite acceptance of the spectrometer.

We have described how the quantities P_o, N^{ac} and Acc in Equation (3.4) were determined. Suppose that we have also determined N_b^t (this is described in detail in the following section). We can then use Equation (3.4) to calculate the invariant cross section. However a problem arises immediately: at what $P_\perp$ is this cross section to be plotted? The most natural choice would be the average $P_\perp$ of the particles N^{ac}. However, as indicated on page 30 this average is not in general, equal to $P_o\theta$. If, on the other hand, we insist that we want to plot the invariant cross section of Equation (3.4) at $P_o\theta$ we have to apply to it some correction. We call this the slope correction.

Before we describe how the slope correction was done we will formulate the problem. Assume that the invariant cross section can be parametrized, locally in $P_\perp$, with some function $f(P_\perp)$. Then:

$$E \frac{d^3\sigma_i}{dP^3} \equiv \sigma_i(P_\perp) = K f(P_\perp) \tag{3.11}$$

where K is a constant. From Equations (3.3) and (3.11) we have then:

$$K f(P_\perp) = \frac{dN^{ac}}{N_b^t} \frac{1}{P P_o \frac{dN^{ac}}{dN^{pr}} d\Omega \frac{dP}{P_o}} \tag{3.12}$$

or:

$$N^{ac} \equiv \int dN^{ac} = N_b^t K P_o \int f(P_\perp) P \frac{dN^{ac}}{dN^{pr}} d\Omega \frac{dP}{P_o} \tag{3.13}$$

where the integral is over the solid angle seen by the spectrometer and the momentum acceptance of the spectrometer. If we now indicate the left hand side of Equation (3.4) as σ_0 (from now on called the zero iteration invariant cross section) we will have:

$$\sigma_o = \frac{N^{ac}}{N_b^t} \frac{1}{P_o^2 \, Acc} \tag{3.14}$$

or:

$$N^{ac} = \sigma_o N_b^t P_o^2 Acc \tag{3.15}$$

From Equations (3.13) and (3.15) we have:

$$K = \sigma_o \frac{P_o \, Acc}{\int f(P_\perp) P \frac{dN^{ac}}{dN^{pr}} d\Omega \frac{dP}{P_o}} \tag{3.16}$$

We can get an idea of the functional form of $f(P_\perp)$ by plotting the zero iteration cross sections (Equation (3.14)) versus $P_\perp$ as shown in Figure 31. From Figure 31 we see that $f(P_\perp)$ can (locally in $P_\perp$) take the form:

$$f(P_\perp) = e^{-\alpha P_\perp} \tag{3.17}$$

As we see from Figure 31 α does change with $P_\perp$ but it is quite constant over the momentum acceptance of the spectrometer.

From Equations (3.11), (3.16) and (3.17) we have:

$$\sigma(P_{\perp o}) = K f(P_{\perp o}) = \sigma_o \frac{P_o \, A_{cc} \, e^{-\alpha P_{\perp o}}}{\int P \, e^{-\alpha P_\perp} \frac{dN^{ac}}{dN^{tr}} \, d\Omega \, \frac{dP}{P_o}} \tag{3.18}$$

where: $P_{\perp o} = P_o \theta$.

It is now clear from Equation (3.18) that the slope correction to σ_o is given by:

$$c = \frac{P_o \, A_{cc} \, e^{-\alpha P_{\perp o}}}{\int P \, e^{-\alpha P_\perp} \frac{dN^{ac}}{dN^{tr}} \, d\Omega \, \frac{dP}{P_o}} \tag{3.19}$$

Based on the above analysis the slope correction is done as follows:

1) Calculate the zero iteration cross sections (Equation (3.14)).

2) For each pair of neighboring points $P_{\perp 1}$, $P_{\perp 2}$, (where we took data) with zero iteration cross sections σ_{o1}, σ_{o2}, respectively calculate the local slope using the formula:

$$\alpha = \frac{\ln\left(\frac{\sigma_{o1}}{\sigma_{o2}}\right)}{P_{\perp 1} - P_{\perp 2}} \tag{3.20}$$

We call these the measured slopes. Then we fitted the measured slopes to a smooth curve. A quadratic fit (if

there were more than three measured points) or a linear fit (if there were only three measured points) proved to be adequate in almost all cases. To calculate the slope correction (see Step 3, below) at each $P_\perp$ point the fitted slope corresponding to that point was used. In only a few cases the fitted slopes seemed to be obviously unreasonable and we had to use inserted (after careful inspection) slopes. An example of measured and fitted (to a quadratic) slopes is shown in Figure 32.

3) Calculate the correction factors c according to Equation (3.19). The denominator of Equation (3.19) was found by numerical integration. (As $\frac{dN^{ac}}{dN^{pr}}$ we took the ratio of the number of particles accepted by the spectrometer divided by the number of particles produced in the solid angle $d\Omega = 2\Delta\theta_x\Delta\theta_y$ and in a momentum interval with central momentum P and bite $\frac{dP}{P_o} = 2\%$.

4) Multiply the σ_o's by c's to find the first iteration cross sections σ_1's.

5) Repeat steps 1→4, using in the place of the σ_o's the last iteration cross sections, as many times as they are required for the cross sections to converge.

We found out that the fourth iteration cross sections differed from the third iteration ones by less than .5%. We iterated all cross sections three times.

Typical values for c (Equation (3.19)) were ~6% at ±10 GeV/c, ~25% at ±30 GeV/c and ~50% at ±60 GeV/c (the increase of c with momentum is due to the growth of the absolute momentum bite with momentum).

Beam Normalization

The last quantity that remains to be determined in the right hand side of Equation (3.4) is N_b^t. This is given by (see Equation (3.6)):

$$N_b^t = N_0 \left(1 - e^{-L/\lambda_b}\right) \frac{\rho N_A \lambda_b}{A} \left(1 - F_i\right)$$

We explained in page 42 how the F_i's were found. ρ (the density of the target) is given in Table 4. The absorption length λ_b of the beam particles in the target was calculated using the formula:

$$\lambda_b = \frac{A}{\sigma_b N_A \rho}$$

The absorption cross sections, σ_b, were obtained from References 58, 59, 60, 61, 62 and 63 and are given in Table 14.

N_0, the number of beam particles that hit the target, was measured by IC710 for the hydrogen target. .To find N_0 for the nuclear targets we combined the information from IC710, IC711/IC712 and the East and West 90° monitors. In the following we first describe how IC710 was calibrated and then we explain how the beam normalization for the hydrogen and the nuclear targets was done.

Calibration of IC710

We define the scale factor S of the ion chamber as the number of particles that have to go through it to produce one count at the digitizer. The value of S may be different for pions and protons of the same energy because of their different ionization (relativistic rise).

We found S for IC710 for pions with the following four methods:

1) Counting the Number of Beam Pions by a Scintillator

A scintillator was put at the position of the experimental target. The pion beam intensity was lowered to a small enough value ($\sim 5\times10^5$ π^-/pulse) so that the scintillator would not saturate. We then measured, during a run, the number of scintillator counts N_{sc}, the number of IC710 counts N_{ic}, the number of the spectrometer triggers N_{tr}, and the number of beam pulses P. If N_{pd} is the number of IC710 pedestal counts per pulse (this was also measured) then the scale factor of IC710 should be:

$$S = \frac{N_{sc}}{N_{ic} - P N_{pd}} \tag{3.21}$$

We also did several more runs with higher beam intensities (up to $\sim 1 \times 10^9$ π^-/pulse, i.e., close to the typical intensities of the experiment). The ratio: $N_{tr}/(N_{ic}-P\ N_{pd})$ remained constant within 5% with intensity. This ensured the linearity of IC710 up to the above intensities.

2) Foil Calibration with Protons

This was done with primary 200 GeV protons. A thin copper foil was put just in front of IC710 and a run of some certain number of pulses P was taken. Beam intensities were $\sim 2 \times 10^{10}$ protons/pulse. The number of IC710 counts N_{ic} was recorded.

The copper foil was analyzed[64] and the amount of ^{24}Na produced in the reaction:

$$p + Cu \rightarrow {}^{24}Na + X \tag{3.22}$$

was measured radiochemically. From the cross section of reaction (3.22) (we took it to be 4mb[64,65,66] and the amount of ^{24}Na produced, the number of protons N_p that went through the foil and IC710 was determined. The scale factor of IC710 for 200 GeV protons was then:

$$S_p = \frac{N_p}{N_{ic} - P N_{pd}} \tag{3.23}$$

The scale factor for 200 GeV pions was obtained by adjusting S_p for the difference in dE/dX for pions and protons because of the relativistic rise, a 5% effect[67].

A problem with this method was that IC710 started to saturate at intensities of ~2 x 10^{10} particles/pulse. We solved it by plotting on a pulse-by-pulse base the IC710 counts/SEM counts ratio versus SEM counts. This ratio did reach a constant value at intensities of about 10^{10} protons/pulse. The difference of this ratio at intensities 2 x 10^{10} and 10^{10} protons/pulse gives, of course, a measure of the size of IC710 saturation between the two intensities.

3) Foil Calibrations with Pions

This method is similar to #2. It was done as follows: two copper foils (~1 mil thickness each) were put one in front of the SEM (in the primary proton beam - see Figure 6) and the other in front of IC710 (in the secondary π^- beam - see Figure 6).

The two foils were irradiated by the proton and π^- beams, for several days. The proton and π^- beam energies were 350 GeV and 200 GeV respectively. Their intensities were ~5 x 10^{12} protons/pulse and 7 x 10^8 π^-'s/pulse.

The two foils were analysed and the amounts of ^{57}Co produced in each of the reactions:

$$\pi^- + Cu \rightarrow {}^{57}Co + X \tag{3.24}$$

$$p + Cu \rightarrow {}^{57}Co + X \tag{3.25}$$

were measured. By assuming (this assumption is confirmed by measurements[68]) that the ratio of the cross sections of reactions (3.24) and

(3.25) is equal to the ratio of the total inelastic cross sections of protons and π^-'s in Cu we could determine the π^-/incident proton yield of the secondary beam. From the number of SEM counts and its scale factor (found according to method #2) the total number of protons that hit the experimental target was found. From the number of protons and the π^-/proton yield the number of π^-'s that went through IC710 was measured. The number of π^-'s and the number of IC710 counts gave the IC710 scale factor.

The advantage of this method relative to method #2 is that this one was done with beam conditions (particle type and intensities) similar to the ones during the experiment.

4) Direct Calculation of the Scale Factor

We also calculated S for 200 GeV π^- directly as follows: Assume that dE/dx is the average energy loss per unit length for 200 GeV π^-'s in the chamber gas and $\bar{E}$ is the average energy needed to produce one ion pair. dE/dx and $\bar{E}$ were taken from Reference 67. Then the total number of ion pairs per π^-, produced in IC710 would be:

$$N = \frac{dE}{dx}\frac{L}{\bar{E}} \tag{3.26}$$

where L is the "gas" length of IC710. Then if q is the electric charge needed to produce one count in IC710 (this was measured) the scale factor S should be:

$$S = \frac{q}{Ne} \tag{3.27}$$

where e is the electron's charge.

The IC710 scale factors as obtained with methods 1→4 are given in Table 15.

The 7% quoted error of method #1 measures the nonlinearities of the scintillator (5%) and of IC710 (5%) versus the beam intensity.

The 9% quoted error of method #2 is because of the error in the cross section of the reaction (3.22), (7%), and because of the nonlinearity of IC710, (5%).

The 9% quoted error of method #3 is because of a 7% error in the cross section of reaction (3.22) and a 5% error in the assumption that the cross sections of reactions (3.24) and (3.25) are proportional to the respective total inelastic cross sections[68].

Finally the 7% quoted error of method #4 is because of errors in the measurement of L, $\frac{dE}{dx}$ and $\bar{E}$. These errors were 2%, 5% and 4% respectively.

We used the calculated number (method #4) as the scale factor of IC710. Note that the mean of the four methods is 1.59×10^4 π^-'s/count and their spread is ±8% (sigma).

We conclude that we know the absolute beam normalization to better than ±10%.

The Beam Normalization for the Hydrogen Target

The beam size was smaller than the hydrogen target and IC710 was much bigger than both of them. We therefore used IC710 to find the number of π^-'s that hit the hydrogen target for each run. Runs with very poor effective spill lengths and/or indication of IC710 saturation were rejected.

The Beam Normalization for the Nuclear Targets

The normalization of the nuclear targets was done as follows: For each target the average ratio $R_T \equiv \langle \frac{ME}{MW} \rangle$ was calculated where ME and MW were the counts for each run of the East and West 90° monitors

respectively corrected for accidentals. Then the average (over all runs with the same target) ratio $K_T \equiv \frac{ME+R_T MW}{IC712}$ was calculated (IC712 was the counts minus pedestal of the inner part of the ion chamber IC711/IC712 for each run). The number of π^-'s that hit some nuclear target T during some run should then be:

$$N_{\pi^-} = \frac{ME + R_T MW}{K_T} \tag{3.28}$$

The number of π^-'s that went through IC712 was calculated from the ratio of the IC712 to IC711 counts which we obtained from the ion chamber IC711/IC712, and the requirement that the sum of IC711 plus IC712 particles should be equal to the particles measured by IC710. In this way an independent determination of the IC711/IC712 scale factor was not necessary.

It should be noted that, before each running period, the ion chamber IC711/IC712 was carefully aligned along the beam line, making therefore sure that the amount of beam that hit the nuclear targets was equal to that which passed through IC712.

The reason that the nuclear target beam normalization was not done directly with IC712 was because we felt that the ME,MW counts were a more direct and sensitive, though only relative, measure of the amount of beam that hit the target. We did not use this method for normalizing the hydrogen target only because the statistics in the 90° monitors were poor.

The stability of the $\frac{ME+R_T MW}{IC712}$ ratios (as measured by the sigmas of their distributions over all runs) was ~2-3% (this spread was caused by transverse beam motion - the statistical error was less than 1%).

Backgrounds

The most significant background for the hydrogen data came from the target walls. We described on page 40 how it was subtracted.

For the nuclear targets, background events could come from the atmospheric gas and/or other material close to the experimental target (such as the ion chambers, see Figure 8). To find the size of this background we took runs at several momenta with the target out.

At ±25 GeV/c spectrometer settings the target-out yields were much less than 1% of the yields of any of the nuclear targets. At ±40 GeV/c, the highest momenta with nonzero target-out yields, this background was 1-2% of the Be target yield and less than 1% of the Cu and W target yields. However the statistics were very bad (±100%).

We therefore decided to do the following: because for momenta up to 30 GeV/c the target-out yields were much less than 1% we did not make any correction for it. For momenta $\geq$40 GeV/c a 2% systematic error was assigned to the cross sections of the Be target only, as an upper limit to the uncertainty of this background at high momenta.

Special Problems with the Analysis

Problem with the 40 GeV/c Be runs

The $(ME+R_T MW)/IC712$ ratio (see page 58) was about a factor of 2.5 lower than its average value for the ±40 GeV/c runs with the Be target (200 GeV π^-, pitched to the West beam). A careful examination of the ratios IC712/IC710 and IC712/IC711 did not show anything unusual. This indicated that the beam was at the right position.

The above two facts roused the suspicion that the Be target was not at its nominal position during those two runs.

Indeed the vertical distribution of the events at the target and at D7 showed clearly that the target was lower than its nominal height by a considerable amount. Because these were the only Be runs at ±40 GeV we tried and succeeded in correcting them. To do that we had to answer two questions: 1) What fraction of the beam flux counted by IC712, hit the offset target? and 2) What was the reduction of the acceptance of the spectrometer because of the target offset?

The answer to the first question was easy. The 90° monitor counts were proportional to the amount of beam that hit the target (since their distance from the target was ~20', a target motion of even the whole target vertical size, 3/4", should not have changed their acceptance at all). Since we did use the 90° monitors to normalize the nuclear targets the problem posed by this question was automatically solved. However we have to emphasize here that the ±40 GeV/c runs were not used in calculating the average $\frac{MW+R_T MW}{IC712}$.

To answer the second question we used the Monte Carlo. We first made sure that the Monte Carlo reproduced the vertical target and D7 distributions well. We then made several runs "lowering the target" at the program by small intervals. Comparison of the vertical distributions at the target and at D7 between these Monte Carlo runs and those of the ±40 GeV data runs showed that the target should have been lower than its nominal position by ~.475". This corresponded to a (22±5)% reduction in the acceptance. The relevant cross sections were multiplied by 1/.78 and the ±5% uncertainty in this correction was added, in quadrature, to their total errors.

The offset of the Be target was caused by improper operation of the target controls system. The vertical target position was not

zeroed before the target controls were given instructions to bring the Be target at beam height. This resulted in a vertical target offset although the readback value for the vertical position indicated that the target was at its nominal height.

The pleasant part of this problem was our realization, once more, of the power of the Monte Carlo program.

Discussion of Errors

At the low momentum region (10, 15 and 20 GeV/c) the errors to the cross sections are dominated by systematic uncertainties. There follows a transition region (~30 GeV/c) where systematic and statistical (arising from the Poisson distribution of events) errors are about equal. Finally at high momenta (≥40 GeV/c) the statistical errors are dominant.

At low momenta (10, 15 and 20 GeV/c) we assigned a systematic error of ±8% due to uncertainties in the scalers method. This figure is about half the difference in the cross sections at ±10 GeV/c computed by the scalers and reconstruction methods. All other systematic errors are much smaller here and were neglected (for example the maximum error in the empty target subtraction from the hydrogen target is ~±2%, the maximum error because of muon misidentification is ~±2%, the maximum error in the slope correction is ~±1%, the maximum error because of absorption is ~±2%). The total error in the cross sections at this momentum region is the statistical error plus the ±8% systematic error added in quadrature.

For momenta ≥25 GeV/c the total error is the sum of the following errors: the error in the slope correction, the error in the

empty target subtraction (±2%, for the hydrogen target only), the error because of beam motion [±4%, as measured by the spread of $(ME+R_TMW)/IC712$ ratio (see page 58) and the uncertainty in the acceptance (see page 49)], the error in the correction because of absorption in the target (±2% for nuclear targets only), and the statistical error. All these errors were added in quadrature.

Since the maximum error because of kaon misidentification (6% of the kaon cross section) at momenta 70, 75, 80 and 90 GeV/c (see page 40) is much smaller than the statistical errors at these momenta it was neglected. For the same reason the 2% error due to uncertainties in the background subtraction from the Be target cross sections (see page 59), was neglected.

Not included in the errors to the cross sections is a ±12% overall normalization error. It is the sum in quadrature of the uncertainty in the beam normalization (±10%), the uncertainty in the reconstruction program inefficiency (±2%), the error in the cross section because of the uncertainty in the transverse momentum scale (±5%) and the overall uncertainty in the integrated acceptance (±5%). The overall uncertainty in the acceptance was computed by examination of the change in the cross sections when the DST cuts were varied within reasonable limits.

CHAPTER IV

RESULTS

This chapter presents the results of this experiment. In the first section I summarize the results that were obtained by James Green[25] who analysed the hydrogen target data. In the second section I present my analysis of the data on the angular dependence and compare them with predictions of theoretical models. The third section presents my analysis of the data on the atomic weight dependence in $\pi^- N$ collisions. Finally, in the last section my conclusions are listed.

The Production of High $P_\perp$ Hadrons in π^--p Collisions

In this section I mention briefly the main conclusions that were reached from the part[25] of the data of this experiment which are not included in my thesis. These data, as was mentioned in Chapter I, are the production cross sections of long lived charged hadrons with transverse momenta in the 1→6 GeV/c region and with 200, and 300 GeV π^- and 200 GeV proton beams incident on a hydrogen target.

The main conclusions[25] from the above data were the following:

1) The cross sections with the 200 GeV proton beam, from this experiment agree within 25% (consistent with the quoted systematic errors of the two experiments) with the ones of Reference 8. This is a very important check on our experiment.

2) The data show a general trend that the observed particles reflect the quark content of the incident particles.

3) The pion beam cross sections do not fall as rapidly with increasing $x_\perp$ as the proton cross sections, in agreement with the fact that the pion structure function is much flatter than that of the proton.

4) The data do not agree by more than an order of magnitude with the predictions of the CIM model[17]. They do agree more or less with the predictions of the model of Field[18].

5) The 200 and 300 GeV cross sections with the π^- beam factorize to fit the form $P_\perp^{-n}(1-x_\perp)^m$ (see Equation 1.5). The fits are good. The power n is ~8 for the mesons ($\pi^\pm$ and $K^\pm$) and ~10 for p and $\bar{p}$ (much larger than the value 4 expected from first order QCD but the same as that obtained from the proton data[8]).

Data on Angular Dependence and Comparison with Theoretical Models

As mentioned before we took data with the spectrometer at 96.3, 80 and 63.7 mrad (in the lab frame) with respect to the 200 GeV incident π^- beam. The above angles correspond, for a massless particle, to CM angles of 90°, 79° and 67° respectively. The CM angles for each of the π, K and p and for each of the three lab angles are listed versus momentum in Table 16. We notice that at very small momenta (10 and 15 GeV/c) the CM angles for K's and p's differ considerably from their asymptotic values. However for momenta $\geq$25 GeV/c or for $P_\perp \geq 2$ GeV/c, the CM angles for all three species of particles are very close.

The invariant cross sections for the production of each of the particles $\pi^{\pm}$, $K^{\pm}$, p and $\bar{p}$ and for each of the three angles in 200 GeV π^-p collisions are listed in Tables 17, 18 and 19. The quoted errors are the total errors (statistical and systematic), and were calculated as described on page 61. These cross sections are plotted versus $P_\perp$ in Figures 33, 34 and 35. We do not observe any significant angular dependence for the production of the positively charged particles π^+, K^+ and p, in this range of angles. However we do see an increase of the cross sections for the production of the negatively charged particles π^-, K^- and $\bar{p}$ as we move at smaller angles in the forward hemisphere.

In contrast to the case of proton-proton collisions the angular distribution in π^--p collisions need not be symmetric around 90° CM angle. It should also be noted here that because a quark in the pion has, on the average, a higher momentum in the π^--p CM frame than a quark in the proton (the pion has two quarks and the proton has three) the quark-quark CM system moves in the forward direction with respect to the π^--p system. Therefore the 90° angle of the π^--p system corresponds to a larger angle in the quark-quark system. The more forward angles of 79° and 67° in the π^--p CM system could therefore correspond to angles closer to 90° in the quark-quark system. If the processes that we study do come from quark-quark hard scattering and furthermore if they were quark flavor invariant they should be symmetric around 90° in the quark-quark CM system (see also the analogy with pp case; Reference 30 and Figure 4). An increase, then, of the cross sections as we move from 90° to 79° and 67° in the π^--p system could be easily explained. However we know that this is not quite true. The cross

sections do depend on the kind of the interacting particles, i.e., on the quark flavor. If one makes the reasonable assumption[24] that a particle observed at large x_1 came from a valence quark, one can identify a π^+ or K^+ or p as usually coming from the proton and a π^- or K^- or $\bar{p}$ as coming from the beam π^-. Furthermore if we assume that the observed particle has a large fraction of the scattered quark's momentum, then the particle's direction is close to that of the scattered quark. Therefore the measured angular dependence should be strongly correlated with the angular dependence of the underlying hard-scattering process.

The increase of the π^-, K^- and $\bar{p}$ cross sections as we move from the 90°, in the π^--p frame, to 79° and 67° clearly indicates that these cross sections do not depend only on $P_\perp$ or, equivalently, only on the impact parameter of the collision (see page 11 and References 27 and 28).

In Figures 36 and 37 we compare the cross sections for the production of $\pi^\pm$ and $K^\pm$ at 90° in π^--p collisions with the predictions[69] of the FFF model. The shapes of the predicted cross sections are very similar to the data for all particles. However the normalization of the predicted theoretical cross sections seems to be smaller than the data (the disagreement is bigger for π^+ and K^+ and it is very small for π^- and K^-). Note that the predictions of the FFF model are also lower for the $pp \to \pi^\circ$ + anything case (see Figure 5). Not shown in the predicted cross sections of Figures 36 and 37 is a 30% "statistical" error due to the limited number of Monte Carlo events that were used to estimate these theoretical cross sections[70]. No comparison is done with the p and $\bar{p}$ cross sections because the FFF model does not handle

baryons. Also no comparison between the data and the FFF model is done for the 79° and 67° CM angles because no predictions of these cross sections versus $P_\perp$ were available at the time that this thesis was written. However the cross sections (at $P_\perp$ = 4 GeV/c) versus the CM angle were given to us by R. Field. These are listed in Table 20. We see that the π^- and K^- cross sections increase as we move from 90° to 60° in qualitative agreement with the data. Also the small decrease of the π^+ and K^+ cross sections at the same angle range is not inconsistent with the data.

As I mentioned already in the introduction (Chapter I) the CIM model disagrees drastically with the 90° π^--p data[24,25]. No further comparisons with this model will be made in this thesis.

In Tables 21-25 the trigger ratios π^-/π^+, K^-/K^+, $\bar{p}/p$, K^+/π^+ and K^-/π^- for the three angles are listed. As trigger ratio of two hadrons h_1 and h_2 produced in π^--p collisions we define the quantity:

$$\frac{\pi^- + p \to h_1 + \text{anything}}{\pi^- + p \to h_2 + \text{anything}}$$

The quoted errors are the sum, in quadrature of the statistical error and the error in the slope correction (all other systematic errors cancel in these ratios).

In Figures 38 and 39 the above ratios have been plotted versus $P_\perp$. Also shown are the predictions[69] of the FFF model (again this model cannot predict the $\bar{p}/p$ ratio).

From Figure 38 we see that all three antiparticle/particle ratios increase as the CM angle decreases at a fixed $P_\perp$. This increase is strongest for the π^-/π^+ ratio and it is the smallest for the $\bar{p}/p$ ratio.

This behavior is in accordance with the quark flavor content of the particles involved (see also remarks made on page 65). The K^-/K^+ ratio is constant up to $P_\perp \approx 3$ GeV/c and then it shows, for larger $P_\perp$, a small decrease. The same, with much less certainty though, could be said for the π^-/π^+ 90° ratio. Fitting the π^-/π^+ ratio to a constant C we get C = 1.18. The X^2 of the fit is 13.34 for seven degrees of freedom. This corresponds to an ~15% confidence level. Neil Fleishon and James Stirling[71] suggest that a decrease in the π^-/π^+ at large $x_\perp$ could be explained if the pion gluon distribution function is enhanced such that the dominant scattering mechanism is beam glue on target quarks. The π^-/π^+ ratio then will fall below unity because the proton consists of more up than down quarks. The π^-/π^+ and K^-/K^+ predicted[69] ratios by the FFF model are in overall qualitative agreement with the data. However this model predicted a much stronger angular dependence. Both the data and the predictions of the FFF model are consistent with no angular dependence of the K^+/π^+ and K^-/π^- ratios (see Figure 39).

Another way to present the trigger ratios is versus the CM angle at a fixed $P_\perp$. This is done (at $P_\perp$ = 4 GeV/c) for the trigger ratios π^-/π^+, K^-/K^+ and K^-/π^- in Figure 40. Also shown are the same ratios as measured in 200 GeV pp collisions in this experiment (see Reference 25) and the predictions of the FFF model for both the π^- and, for contrast, the proton beams. The measured value of these ratios in pp collisions and at 90° agrees with the predictions very well. The FFF predictions for the K^-/π^- ratio in π^--p collisions agree very well with the data too. However the predicted π^-/π^+ and K^-/K^+ ratios are considerably larger than the data especially at θ_{CM} = 67°. After these trigger ratios were published[24], R. Field[70] succeeded in rectifying the above disagreement by hardening the gluon fragmentation

function of the FFF model. This new prediction for the π^-/π^+ ratio (indicated as the New FFF) is shown by the dashed line in Figure 40. Field[70] says that hardening the gluon fragmentation function is a way to solve the problem but it may not be the only one. The cause of the disagreement may well lie elsewhere.

Neil Fleishon and James Stirling tried to fit simultaneously the following data:

$\frac{\pi^- + p \to \pi^\circ + X}{p + p \to \pi^\circ + X}$	beam ratio of Reference 72,
$\frac{p + p \to \pi^- + X}{p + p \to \pi^+ + X}$	trigger ratio of Reference 8 and
$\frac{\pi^- + p \to \pi^- + X}{\pi^- + p \to \pi^+ + X}$	trigger ratios at 90°, 79° and 67° of this experiment.

They used a naive, hard scattering, QCD parton model like the one of the FFF model. They tried to fit the above three sets of data by varying the proton gluon distribution functions but they did not succeed. Their conclusion was that the proton gluon distributions indicated by the beam and the trigger ratios were inconsistent.

More recently E.L. Berger et al.[73] have calculated the absolute rate and kinematic dependence of the cross sections for the high-twist subprocesses $qg \to \pi q$ and $q\bar{q} \to \pi g$ in perturbative QCD. They show that the contributions of these high-twist terms are quantitatively important for $P_\perp \lesssim 6$ GeV/c and $x_\perp \gtrsim 0.5$. The inclusion of these terms does not make the π^-/π^+ trigger ratio agree with our data. Their predicted ratio is still too high especially at the forward angle of 67°.

Nuclear Target Data - Atomic Weight Dependence

The invariant cross sections per nucleus for the production of each of the hadrons $\pi^\pm$, $K^\pm$, p and $\bar{p}$ in π^--N collisions, where N=W,

Be, Cu, with 200 GeV beam and at 90° CM angle are listed in Tables 26, 27 and 28. The invariant cross sections with 300 GeV π^- beam and W target at 90° are listed in Table 29. The quoted errors are the total errors, and were calculated as described on page 61.

In Figure 41 the invariant cross sections per nucleus versus $P_\perp$ for the production of each of the $\pi^\pm$, $K^\pm$, p and $\bar{p}$ in π^--W and π^--Be collisions are plotted. We see that the invariant cross sections are steeply falling functions of $P_\perp$, the fall being even steeper for the case of the baryons p and $\bar{p}$ (this was also the case for the hydrogen target cross sections[25]). We also note for both targets and for P up to ~3 GeV/c hadrons are produced with decreasing abundance as: π^-, π^+, p, K^+, K^- and $\bar{p}$. For $P_\perp > 4$ GeV/c protons are produced with a smaller abundance than that of K^+ and K^-.

In Figure 42 we compare the invariant cross sections for the production of each of π^+, π^-, K^+, K^-, p and $\bar{p}$ with the W and Be targets. We note that as P increases the W and Be cross sections deviate more and more from each other (this effect is stronger in the case of the baryons p and $\bar{p}$). We also note that for $P_\perp >$ ~4 GeV/c the above deviation has reversed (for the case of π^+, π^-, K^+ and K^-) and the cross sections for the two targets come closer together. The anomalous atomic weight dependence (see Chapter I and below) is a manifestation of this behavior of the cross sections.

In Figure 43 the 200 and 300 GeV cross sections (with the W target) for the production of π^+ and π^- respectively are plotted. We see that there is not much $\sqrt{s}$ dependence at low $P_\perp$. However we do see a $\sqrt{s}$ dependence at high $P_\perp$. This dependence is stronger the higher the $P_\perp$.

These features of the cross sections are similar to the ones observed with a proton beam[7,8].

One word on the π^-/π^+ ratio with the nuclear targets is in order. We remind that this ratio is 1.16±0.04 (see Table 21) at $P_\perp$=2.9 GeV/c in 200 GeV π^-p collisions and at 90° in the CM system. From Tables 26, 27 and 28 we find that at the same $P_\perp$ this ratio is 1.43±0.07, 1.41±0.07 and 1.36±0.06 for the Be, Cu and W targets respectively. We note that, at this value of $P_\perp$, the π^-/π^+ ratio for the nuclear target is about 20% higher than the hydrogen target one. This is consistent with the fact that the neutrons consist of two d quarks and only on u quark and therefore they should produce π^-'s more copiously than the protons. We also note that the π^-/π^+ ratio is the same, within errors, for the three nuclear targets as it should be because their proton/neutron ratios are about the same and equal to ~1. It should however be noted that it would be dangerous to try to extract the π^-/π^+ ratio for a neutron target from the nuclear and hydrogen target data. To do this a deuteron target should be used.

In Figure 44 the H, Be, Cu and W cross sections relative to the W cross section versus the logarithm of the atomic weight have been plotted for each of the particles $\pi^\pm$, $K^\pm$, p and $\bar{p}$. These relative yields correspond to $P_\perp$ = 2.9 GeV/c (we have data with the Cu target only at $P_\perp$ = 2.4 and 2.9 GeV/c - see Table 28). We see that the three nuclear target points lie on a straight line (the hydrogen target point tends to lie below the line). The straight lines drawn in Figure 44 are just fits by eye.

Figure 44 suggests that the invariant cross sections per nucleus can be parametrized (for the nuclear targets) as:

$$E \frac{d^3\sigma}{dP^3} = I_i(P_\perp) A^{\alpha_i(P_\perp)} \tag{4.1}$$

where the index i refers to the outgoing hadron i ($i = \pi^\pm$, $K^\pm$, p, $\bar{p}$).

Since we have data with the Cu target only at $P_\perp$ = 2.4 and 2.9 GeV/c, we have used only the Be and W targets to extract the exponents $\alpha_i(P_\perp)$. This exponent for a particle i and for some $P_\perp$ is given by the form:

$$\alpha_i(P_\perp) = \frac{\ln\left(\frac{\sigma_W(P_\perp)}{\sigma_{Be}(P_\perp)}\right)}{\ln\left(\frac{A_W}{A_{Be}}\right)} \tag{4.2}$$

where α_W and α_{Be} are the W and Be target cross sections and A_W, A_{Be} are their atomic weights respectively.

The exponents α_i's for the six particles are listed in Table 30. To calculate the quoted errors in the α_i's we assigned as total errors to the invariant cross sections the sum, in quadrature, of the statistical error, the error in the slope correction and a 3% systematic error. This sytematic error is the sum, in quadrature, of a 2% error in the estimation of the target absorption, a 2% error because of beam motion and a 1% error in the target densities. All other systematic errors are the same for the two targets and should cancel in the ratios (see Equation (4.2)).

The exponents α_i's are shown in Figure 45. Also plotted are the exponents from Reference 34 measured with D, Be, Ti and W targets wtih 400 GeV protons and at 97° CM angle. The dashed lines at α_i = 1 have been drawn for contrast.

From Figure 45 we notice that the α_i's for the π^- beam are very much similar to the corresponding ones for the proton beam i.e.,

1) at low $P_\perp$ the α_i's approach the value of 2/3 as expected

from the area of a black disk (see page 12),

2) for $P_\perp$ values $\gtrsim$2 GeV/c they exceed the value 1, an indication that the nucleus acts in some collective way,

3) The $\alpha_{\pi^\pm}$ and $\alpha_{K^\pm}$ seem to saturate at $P_\perp$ = 4 GeV/c,

4) $\alpha_{\pi^\pm}$ and $\alpha_{K^\pm}$ show an indication of decreasing at $P_\perp$>4 GeV/c but the statistics at these $P_\perp$ values is not good enough so that a definite statement on this matter could be made,

5) α_p and $\alpha_{\bar{p}}$ seem to rise to much higher values than the rest of the exponents but again the statistics is not sufficient to confirm if this, extremely strong, A-dependence is true (we note that an α value of 1.5 means that the tungsten nucleus acts as if it had 2500 nucleons).

From the same Figure we notice that the proton exponents are slightly higher than the π^- ones at the low (1→3 GeV/c) $P_\perp$ region. This is consistent with a small $\sqrt{s}$ dependence observed[34] at low $P_\perp$ with proton beams. The fact that the proton data are at 97° rather than 90° could also have some influence on this matter.

Conclusions

We have presented in this thesis data on the angular and atomic weight dependence of inclusive hadron production at high $P_\perp$ with 200 GeV and 300 GeV π^- beams.

A comparison of these data with the predictions of the FFF model[18] which uses a first order QCD calculation and has fitted rather well the similar data but with proton beams shows the following:

1) The invariant cross sections for the production of the mesons $\pi^\pm$, $K^\pm$ predicted by the model follow the shape of

the data but they are lower (the disagreement is bigger for the π^+ and K^+).

2) The model predicted a much stronger angular dependence of the π^-/π^+ and K^-/K^+ trigger ratios than the observed ones. Hardening of the gluon fragmentation function fixed the problem. Attempts by other authors involving variation of the gluon distribution function[71] or addition of some high-twist terms[73] could not fix this problem.

3) The model agreed very well with the angular dependence of the K^+/π^+ and K^-/π^- trigger ratios.

It will be very interesting to extend these data to higher $P_\perp$ and also to further angles (both in the forward and backward hemisphere of the π^--p CM system). Such data could shed light on the gluon fragmentation function. Also pinning down the statistics to determine if the π^-/π^+ trigger ratio falls at higher $P_\perp$ is important.

The atomic weight dependence of the cross sections with π^- beam is very similar to the one observed with proton beams. The nuclei behave in some collective way at high transverse momentum processes.

REFERENCES

1. For a recent review of Hard Processes, see A.V. Efremov and A.V. Radyushkin, La Rivista Del Nuovo Cimento 3, N. 2 (1980).

2. R. Hofstadter, Ann. Rev. Nucl. Sci. 7, 231 (1957).

3. The connection between transverse momentum and small transverse distances is given by the Heisenberg uncertainty principle as long as the whole momentum is transferred in a single collision: see for example Reference 9.

4. M. Banner et al., Phys. Lett. 44B, 537 (1973).

5. F.W. Busser et al., Phys. Lett. 46B, 471 (1973).

6. B. Alper et al., Phys. Lett. 44B, 521 (1973).

7. J.W. Cronin et al., Phys. Rev. D 11, 3105 (1975).

8. D. Antreasyan et al., Phys. Rev. D 19, 764 (1979).

9. S.M. Berman, J.D. Bjorken, J.B. Kogut, Phys. Rev. D 4, 3388 (1971).

10. R. Blankenbecler et al., Phys. Lett. 42B, 461 (1972).

11. For a review of QCD Phenomenology of Large P Processes, see R. Stroynowski, in Proceedings of SLAC Summer Institute on Particle Physics (1979). Edited by Anne Mosher.

12. S.J. Brodsky and G. Farrar, Phys. Rev. Lett. 31, 1153 (1973).

13. V. Matveev, R. Muradyan and A. Tavkhelidze, Nuovo Cimento Letters 7, 719 (1973).

14. R.D. Field and R.P. Feynman, Phys. Rev. D 15, 2590 (1977).

15. R.P. Feynman, R.D. Field and G.C. Fox, Nucl. Phys. B128, 1 (1977).

16. B. Blankenbecler, S.J. Brodsky and J.F. Gunion, Phys. Rev. D 12, 3469 (1975).

17. D. Jones and J.F. Gunion, Phys. Rev. D 19, 867 (1979).

18. R.P. Feynman, R.D. Field and G.C. Fox, Phys. Rev. D 18, 3320 (1978).

19. M. Deutschmann et al., Nucl. Phys. B103, 426 (1976).

20. B.L. Combridge, J. Kripfganz and J. Ranft, Phys. Lett. 70B, 234 (1977); R. Cutler and D. Sivers, Phys. Rev. D 16, 679 (1977) and Phys. Rev. D 17, 196 (1978).

21. R.D. Field, Phys. Rev. Lett. 40, 997 (1978).

22. D.A. Levinthal, Ph.D. thesis, Columbia University, 1980.

23. The production of direct photons (which could be misidentified as π°'s and therefore increase n in the experiment of Reference 22) is at present a matter of both experimental and theoretical controversy; see, for example, Reference 11 and References therein.

24. H.J. Frisch et al., Phys. Rev. Lett. 44, 511 (1980).

25. J.M. Green, Ph.D. thesis, University of Chicago, 1981 (unpublished).

26. F.E. Taylor et al., Phys. Rev. D 14, 1217 (1976).

27. W. Furmanski and J. Wosiek, Proceedings of Tutzing Meeting (1976).

28. W. Furmanski and J. Wosiek, Acta Physica Polonica B8, 649 (1977).

29. G. Donaldson et al., Phys. Lett. 73B, 375 (1978).

30. D. Lloyd Owen et al., Phys. Rev. Lett. 45, 89 (1980).

31. G. Belletini et al., Nucl. Phys. 79, 609 (1966).

32. S.P. Denisov et al., Nucl. Phys. B61, 62, (1973).

33. G.R. Farrar, Phys. Lett. 56B, 185 (1975).

34. L. Klubert et al., Phys. Rev. Lett. 38, 670 (1977).

35. D.A. Garbutt et al., Phys. Lett. 67B, 355 (1977).

36. R.J. Fisk, Ph.D. thesis, State University of New York at Stony Brook, 1978.

37. D.A. Finley, Ph.D. thesis, Purdue University, 1978.

38. D.A. Finley et al., Phys. Rev. Lett. 42, 1031 (1979).

39. C. Bromberg et al., Phys. Rev. Lett. 42, 1202 (1979).

40. H.J. Frisch, Invited Talk at the Annual Meeting, Division of Particles and Fields; Brookhaven National Laboratory, October 1976.

41. H.J. Frisch, Proceedings of the first workshop on Ultra-Relativistic Nuclear Collisions, LBL-8957, UC-34C, Conf - 7905107, May 1979.

42. J. Pumplin and E. Yen, Phys. Rev. D 11, 1812 (1975).

43. J.H. Kuhn, Phys. Rev. D 13, 2948 (1976).

44. A. Krzywicki et al., Phys. Lett. 85B, 497 (1979).

45. F. Berlad, A. Dar and G. Eilam, Technion - PH - 79 - 71.

46. A. Krzywicki, Phys. Rev. D 14, 152 (1976).

47. J.W. Cronin et al., E258 Proposal at FNAL. Proposed: October 1973. Approved: June, 1974.

48. B. Cox et al., P-West High Intensity Secondary Beam Area. Design Report. March, 1977.

49. Halo. A Computer Program to Calculate Muon Halo. By Ch. Iselin. CERN 74-17. Laboratory II. Experimental Areas Group. 29 August, 1974.

50. W.F. Baker et al., NAL-Pub-74/13-Exp. 7100.104.

51. H.W. Atherton et al., CERN 80-07, SPS Division, August, 1980.

52. For a detailed description of these magnets see for example: T. Toohig, Fermilab TM-632/2200.00/1975.

53. J.P. Boymond et al., Phys. Rev. Lett. 33, 112 (1974).

54. C.D. Edwards, Jr., "A Čerenkov Light Sampling Calorimeter." A thesis submitted to the Physics Department of Princeton University-Unpublished.

55. H.J. Frisch et al., IEEE Trans. Nuclear Science N5-27, 150 (1980).

56. Krause and G. Koizumi, FERMILAB TM-607/2920.00/1975.

57. R. Juhala, FERMILAB TM434/0621.05/1973.

58. Particle Properties Data Booklet - April 1980.

59. C. Allaby et al., Soviet Journal of Nuclear Physics 13, 295 (1971).

60. S.P. Denisov et al., Phys. Lett. 36B, 416 (1971).

61. S.P. Denisov et al., Nucl. Phys. B65, 3 (1973).

62. A.S. Carroll et al., Phys. Rev. Lett. 33, 928 (1974).

63. A.S. Carroll et al., Phys. Rev. Lett. 33, 932 (1974).

64. S. Baker, FNAL Safety Section. Private communication.

65. J. Hudis et al., Phys. Rev. 129, 434 (1963).

66. A Chapman-Hatchett et al., CERN Report, SPS/ABT/Int. 79-1 (1979). (We thank Frank Sciulli for this).

67. F. Sauil, CERN 77-09 (1977).

68. D. Boyce, DPT of Nuclear Chemistry, The University of Chicago. Private communication.

69. The π^- cross section was given to me by R. Field in private communication. The π^+, K^+ and K^- cross sections were calculated from the π^- cross section and the predicted trigger ratios π^-/π^+, K^-/π^- and K^-/K^+. These ratios were given to our group by R. Field also in private communication.

70. R. Field, Private communication.

71. Neil Fleishon and James Stirling, University of Washington at Seattle. Private communication. See also Preprint: RLO-1388-847, University of Washington, by the same authors.

72. G. Donaldson et al., Phys. Rev. Lett. 40, 917 (1978).

73. E.L. Berger et al., Phys. Rev. D 23, 99 (1981).

TABLE 1

QCD LEADING ORDER ELEMENTARY SUBPROCESSES

Subprocess		$\lvert A\rvert^2$
$q_i q_j \to q_i q_j$ $q_i \bar{q}_j \to q_i \bar{q}_j$	$i \neq j$	$\frac{4}{9} \frac{s^2 + u^2}{t^2}$
$q_i q_i \to q_i q_i$		$\frac{4}{9} \left(\frac{s^2 + u^2}{t^2} + \frac{t^2 + s^2}{u^2} \right) - \frac{8}{27} \frac{s^2}{u\ t}$
$q_i \bar{q}_i \to q_i \bar{q}_i$		$\frac{4}{9} \left(\frac{s^2 + u^2}{t^2} + \frac{t^2 + u^2}{s^2} \right) - \frac{8}{27} \frac{u^2}{s\ t}$
$q_i \bar{q}_i \to gg$		$\frac{32}{27} \frac{u^2 + t^2}{u\ t} - \frac{8}{3} \frac{u^2 + t^2}{s^2}$
$gg \to q_i \bar{q}_i$		$\frac{1}{6} \frac{u^2 + t^2}{u\ t} - \frac{3}{8} \frac{u^2 + t^2}{s^2}$
$q_i g \to q_i g$		$-\frac{4}{9} \frac{u^2 + s^2}{u\ s} + \frac{u^2 + s^2}{t^2}$
$gg \to gg$		$\frac{9}{2} \left(3 - \frac{u\ t}{s^2} - \frac{u\ s}{t^2} \right) - \frac{s\ t}{u^2}$
$q_i \bar{q}_i \to q_j \bar{q}_j$		$\frac{4}{9} \frac{t^2 + u^2}{s^2}$

TABLE 2

PRIMARY AND SECONDARY BEAM ENERGIES AND SPECTROMETER ANGLES

Primary Proton Beam Energy (GeV)	Secondary Beam Particle	Secondary Beam Energy (GeV)	Lab frame spectrometer angle (mrad)	C.M. frame spectrometer angle
350	π^-	200	80	79°
350	π^-	200	96.3	90°
450	π^-	200	96.3	90°
200	Proton	200	96.3	90°
400	π^-	200	96.3	90°
400	π^-	300	80	91°
400	π^-	200	80	79°
400	π^-	200	63.7	67°

TABLE 3

PROTON WEST HIGH INTENSITY SECONDARY BEAM YIELDS

Proton Beam Energy (GeV)	Secondary π^- Beam Energy (GeV)	Yield of π^- per incident proton
400	200	4.7×10^{-4}
400	300	5.1×10^{-5}
350	200	2.9×10^{-4}

PARTICLE COMPOSITION OF SECONDARY BEAM

$X \equiv \frac{\text{SECONDARY BEAM MOMENTUM}}{\text{PROTON BEAM MOMENTUM}}$	π^- %	K^- %	$\bar{p}$ %
0.5	94.7	4.7	0.6
0.75	98	2	< 0.2

SECONDARY BEAM WIDTHS

SECONDARY BEAM	HORIZONTAL WIDTH (FWHM)	VERTICAL WIDTH (FWHM)
π^-	1"	0.75"
Proton	0.35"	0.3"

TABLE 4

E258 TARGETS

TARGET	ATOMIC WEIGHT	DENSITY	LENGTH		
		(gr/cm^3)	(inches)	(number of absorption lengths for 200 GeV π^-'s)	(number of absorption lengths for 200 GeV protons)
*H	1.01	0.071	20±.001	0.043	0.069
Be (Long)	9.01	1.85	7.22±.001	0.34	0.49
Be (Short)	9.01	1.85	1.±.001	0.047	0.068
Cu	63.54	8.96	2.91±.001	0.41	0.51
**W	183.85	18.22	2.031±.001	0.46	0.556

* The hydrogen was at 20.4°K (boiling point) and atmospheric pressure
** Kennametal W-2

TABLE 5

E258 DRIFT CHAMBERS

Chamber	Coordinate	Distance from Target	Number of Sense Wires
D1	X	116'	15
	U		15
D2	X	122'	15
	U		15
D3	X	170'	15
	U		15
D4	X	176'	15
D5	X	187'	15
D6	X	190'	15
	U		15
D7	X	258'	25
	U		25
			200 wires (Total)

TABLE 6

MUON TO PION RATIO VERSUS MOMENTUM

Spectrometer Momentum (positive and negative) (GeV/c)	μ/π %
10	7.8
15	5.7
20	4.5
25	3.7
30	3.2
40	2.4
50	1.6
60	1.2
70	0.8
80	0.5
90	0.2

TABLE 7

APERTURE AND TARGET CUTS

Location (See Figure 7)	Horizontal (inches)	Vertical (inches)
D7	±6	±3
Downstream dipole	±2.68	±1.48
Upstream dipole	±2.68	±1.48
Downstream quadrupole	2.52*	1.6*
Upstream quadrupole	1.6*	3.0*
Hydrogen target	+2.4 -3.2	±0.8
Nuclear targets	±1.6	±0.7

*The quadrupole cuts were elliptical. The numbers given are the horizontal and vertical semi-axes of the ellipses.

TABLE 8

EMPTY TARGET CONTRIBUTION VERSUS MOMENTUM

(in %)

Momentum (GeV/c)	10	15	20	25	≥30
Particles Produced					
$\pi^{\pm}$	8.3±0.4	8.1±0.2	11.0±1.5	10.9±0.8	11.0±8.0
$K^{\pm}$	8.9±0.8	11.6±1.3	10.7±1.0	10.7±1.7	11.6±3.5
p or $\bar{p}$	9.9±0.9	11.7±1.0	12.8±3.2	13.3±4.2	14.8±14.8

TABLE 9

NUMBER OF ABSORPTION LENGTHS OF GAS IN THE ČERENKOV COUNTER VERSUS MOMENTUM

Spectrometer Setting (GeV/c)	Number of Absorption Lengths
10	0.108
15	0.075
20	0.028
25	0.02
30	0.013
40	0.008
45	0.007
50	0.006
60	0.005
75	0.004
90	0.003

TABLE 10

NUMBER OF ABSORPTION LENGTHS FOR EACH PARTICLE FROM ALL OTHER MATERIAL IN THE SPECTROMETER EXCEPT ČERENKOV GAS

Particle	Number of Absorption Lengths
π^+	0.09
K^+	0.076
p	0.118
π^-	0.09
K^-	0.087
$\bar{p}$	0.127

TABLE 11

ABSORPTION FRACTIONS F_i FOR EACH PARTICLE TYPE IN EACH OF THE EXPERIMENTAL TARGETS

Target / Particle	W	Be (long)	Be (Short)	Cu	H
π^+	0.22	0.16	0.024	0.19	0.019
K^+	0.18	0.13	0.02	0.16	0.014
p	0.24	0.21	0.029	0.22	0.029
π^-	0.22	0.17	0.025	0.19	0.021
K^-	0.21	0.15	0.023	0.18	0.018
$\bar{p}$	0.26	0.245	0.04	0.26	0.038

TABLE 12

INTEGRATED SPECTROMETER ACCEPTANCES FOR THE NUCLEAR TARGETS

(μsr ± 1%)

Running period Momentum (GeV/c)	200 GeV π^- 96.3-mrad	300 GeV π^- 80-mrad
10	5.36	5.57
15	5.55	5.87
20	5.53	5.87
25	5.11	5.38
30	5.11	5.18
40	5.27	5.32
90	5.37	5.40

TABLE 13

INTEGRATED SPECTROMETER ACCEPTANCES FOR THE HYDROGEN TARGET

(μsr ± 1%)

Running period Momentum (GeV)	200 GeV π^- 96.3-mrad	200 GeV π^- 80-mrad	200 GeV 63.7-mrad
10	4.4	4.56	----
15	4.45	4.73	----
20	4.42	4.72	----
25	4.13	4.28	4.34
30	4.14	4.34	4.36
40	4.18	4.45	4.57
50	4.25	4.48	4.51
60	4.25	4.48	4.56
70	4.25	4.48	4.57
90	4.25	4.48	4.47

TABLE 14

ABSORPTION CROSS SECTIONS FOR 200 AND 300 GeV π^- BEAMS

Target	Absorption Cross Section (mbarns/nucleus ± 2%)
W	1416
Be	151
H	20
Cu	654

TABLE 15

IC710 SCALE FACTOR

Method	Scale Factor (π^-'s/count)
1. Scintillator	$1.48 \times 10^4 \pm 7\%$
2. Foil calibration with protons	$1.82 \times 10^4 \pm 9\%$
3. Foil calibration with pions	$1.42 \times 10^4 \pm 9\%$
4. Direct calculation	$1.62 \times 10^4 \pm 7\%$

TABLE 16

CENTER OF MASS ANGLES VERSUS MOMENTUM*

200 GeV π^- Beam

Particle Produced	π			K			P		
Beam-Spectrometer Angle in the Lab	96.3 mrad	80 mrad	63.7 mrad	96.3 mrad	80 mrad	63.7 mrad	96.3 mrad	80 mrad	63.7 mrad
Momentum (GeV/c)									
10	90.4°	----	----	97.2°	----	----	115.0°	----	----
15	90.0°	----	----	93.1°	----	----	101.6°	----	----
20	89.9°	----	----	91.7°	----	----	96.5°	----	----
25	89.9°	----	66.9°	91.0°	----	68.3°	94.1°	----	72.5°
30	89.8°	79.3°	66.8°	90.6°	80.2°	67.8°	92.8°	82.7°	70.7°
40	89.8°	79.2°	----	90.2°	79.7°	----	91.5°	81.2°	----
45	----	----	66.8°	----	----	67.2°	----	----	68.5°
50	89.8°	79.2°	----	90.0°	79.6°	----	90.9°	80.5°	----
60	89.8°	79.2°	66.8°	90.0°	79.4°	67.0°	90.5°	80.1°	67.7°
75	----	----	66.7°	----	----	66.9°	----	----	67.4°
90	----	----	66.7°	----	----	66.8°	----	----	67.2°

* The CM angles are given only for momenta for which data exist.

TABLE 17

INVARIANT CROSS SECTIONS $Ed^3\sigma/dp^3(cm^2/GeV^2)$

BEAM: 200 GeV π^- : TARGET: Hydrogen : CM ANGLE: 90°

Particle Produced	π^+	π^-	K^+	K^-	p	$\bar{p}$
$P_\perp$(GeV/c)						
0.96	$2.18\pm0.18\times10^{-28}$	$2.54\pm0.21\times10^{-28}$	$6.51\pm0.59\times10^{-29}$	$4.91\pm0.46\times10^{-29}$	$6.35\pm0.53\times10^{-29}$	$2.49\pm0.22\times10^{-29}$
1.44	$1.87\pm0.15\times10^{-29}$	$2.26\pm0.18\times10^{-29}$	$6.07\pm0.51\times10^{-30}$	$4.76\pm0.41\times10^{-30}$	$6.63\pm0.55\times10^{-30}$	$2.75\pm0.23\times10^{-30}$
1.93	$2.17\pm0.18\times10^{-30}$	$2.43\pm0.20\times10^{-30}$	$7.43\pm0.71\times10^{-31}$	$5.62\pm0.58\times10^{-31}$	$8.40\pm0.74\times10^{-31}$	$3.54\pm0.36\times10^{-31}$
2.41	$2.50\pm0.12\times10^{-31}$	$2.97\pm0.14\times10^{-31}$	$1.03\pm0.05\times10^{-31}$	$7.72\pm0.41\times10^{-32}$	$9.12\pm0.46\times10^{-32}$	$2.81\pm0.16\times10^{-32}$
2.89	$4.07\pm0.21\times10^{-32}$	$4.73\pm0.25\times10^{-32}$	$1.68\pm0.11\times10^{-32}$	$1.14\pm0.09\times10^{-32}$	$1.27\pm0.08\times10^{-32}$	$4.13\pm0.39\times10^{-33}$
3.85	$1.38\pm0.11\times10^{-33}$	$1.33\pm0.11\times10^{-33}$	$5.55\pm0.71\times10^{-34}$	$3.70\pm0.57\times10^{-34}$	$3.02\pm0.44\times10^{-34}$	$7.18\pm2.14\times10^{-35}$
4.82	$4.85\pm0.99\times10^{-35}$	$6.05\pm1.10\times10^{-35}$	$2.46\pm0.73\times10^{-35}$	$1.58\pm0.61\times10^{-35}$	$7.98\pm4.03\times10^{-36}$	----------
5.78	$2.96\pm1.15\times10^{-36}$	$1.66\pm0.84\times10^{-36}$	$7.92\pm5.68\times10^{-37}$	$4.97\pm5.02\times10^{-37}$	$1.35\pm0.98\times10^{-36}$	----------

TABLE 18

INVARIANT CROSS SECTIONS $Ed^3\sigma/dp^3(cm^2/GeV^2)$

BEAM: 200 GeV π^- : TARGET: Hydrogen : CM ANGLE: 79°

Particle Produced	π^+	π^-	K^+	K^-	p	$\bar{p}$
$P_\perp$(GeV/c)						
2.40	$2.86\pm0.15\times10^{-31}$	$3.68\pm0.21\times10^{-31}$	$1.23\pm0.08\times10^{-31}$	$1.04\pm0.09\times10^{-31}$	$9.00\pm0.61\times10^{-32}$	$3.59\pm0.39\times10^{-32}$
3.20	$1.22\pm0.09\times10^{-32}$	$1.75\pm0.11\times10^{-32}$	$6.19\pm0.63\times10^{-33}$	$4.27\pm0.47\times10^{-33}$	$4.24\pm0.45\times10^{-33}$	$1.12\pm0.20\times10^{-33}$
4.00	$1.03\pm0.10\times10^{-34}$	$1.25\pm0.11\times10^{-33}$	$3.06\pm0.53\times10^{-34}$	$2.49\pm0.47\times10^{-34}$	$1.21\pm0.28\times10^{-34}$	$6.63\pm2.25\times10^{-35}$
4.80	$5.00\pm1.28\times10^{-35}$	$7.85\pm2.08\times10^{-35}$	$2.67\pm0.97\times10^{-35}$	$3.24\pm1.47\times10^{-35}$	----------	$5.52\pm5.57\times10^{-36}$

TABLE 19

INVARIANT CROSS SECTIONS $Ed^3\sigma/dp^3(cm^2/GeV^2)$

BEAM: 200 GeV π^- : TARGET: Hydrogen : CM ANGLE: 67°

Particle Produced	π^+	π^-	K^+	K^-	p	$\bar{p}$
$P_\perp$(GeV/c)						
1.59	$1.18\pm0.06\times10^{-29}$	$1.57\pm0.08\times10^{-29}$	$3.78\pm0.24\times10^{-30}$	$3.94\pm0.23\times10^{-30}$	$3.89\pm0.22\times10^{-30}$	$2.30\pm0.14\times10^{-30}$
1.91	$2.94\pm0.15\times10^{-30}$	$4.18\pm0.21\times10^{-30}$	$1.08\pm0.06\times10^{-30}$	$9.98\pm0.63\times10^{-31}$	$9.63\pm0.54\times10^{-31}$	$5.24\pm0.36\times10^{-31}$
2.87	$6.41\pm0.32\times10^{-32}$	$9.78\pm0.48\times10^{-32}$	$2.60\pm0.16\times10^{-32}$	$2.61\pm0.16\times10^{-32}$	$1.67\pm0.10\times10^{-32}$	$9.07\pm0.67\times10^{-33}$
3.82	$2.06\pm0.13\times10^{-33}$	$3.49\pm0.21\times10^{-33}$	$9.84\pm0.82\times10^{-34}$	$9.28\pm0.83\times10^{-34}$	$4.41\pm0.45\times10^{-34}$	$1.83\pm0.30\times10^{-34}$
4.78	$1.03\pm0.13\times10^{-34}$	$2.30\pm0.25\times10^{-34}$	$3.86\pm0.79\times10^{-35}$	$2.57\pm0.71\times10^{-35}$	$1.08\pm0.36\times10^{-35}$	$3.23\pm2.31\times10^{-36}$
5.73	$4.60\pm1.57\times10^{-36}$	$1.39\pm0.37\times10^{-35}$	$1.04\pm0.61\times10^{-36}$	$1.28\pm0.75\times10^{-36}$	----------	$9.60\pm9.79\times10^{-37}$

TABLE 20

FFF* PREDICTED MESON INVARIANT CROSS SECTIONS VERSUS CM ANGLE

($\pi^- + p \rightarrow h$ + anything: 200 GeV, $P_\perp$ = 4 GeV/c)

Θ_{CM}	$E \frac{d^3\sigma}{dp^3}$ (cm²/GeV²)			
	π^+	K^+	π^-	K^-
150°	1.72×10^{-31}	8.33×10^{-32}	1.00×10^{-31}	1.00×10^{-32}
120°	2.74×10^{-30}	1.21×10^{-30}	2.00×10^{-30}	3.40×10^{-31}
90°	3.80×10^{-30}	1.53×10^{-30}	5.30×10^{-30}	1.27×10^{-30}
60°	2.50×10^{-30}	8.72×10^{-31}	8.00×10^{-30}	1.92×10^{-30}
30°	1.27×10^{-31}	4.80×10^{-32}	1.40×10^{-30}	3.36×10^{-31}

* FFF is Reference 18

TABLE 21

ANGULAR DEPENDENCE OF π^-/π^+ TRIGGER RATIO IN π^--p COLLISIONS

90° (CM ANGLE)		79° (CM ANGLE)		67° (CM ANGLE)	
$P_\perp$ (GeV/c)	$\frac{\pi^-}{\pi^+}$	$P_\perp$ (GeV/c)	$\frac{\pi^-}{\pi^+}$	$P_\perp$ (GeV/c)	$\frac{\pi^-}{\pi^+}$
0.96	1.17±0.02				
1.44	1.21±0.02				
1.93	1.12±0.04			1.59	1.33±0.04
2.41	1.19±0.02	2.40	1.29±0.06	1.91	1.42±0.04
2.89	1.16±0.04	3.20	1.44±0.11	2.87	1.53±0.05
3.85	0.96±0.09	4.00	1.21±0.14	3.82	1.70±0.10
4.82	1.25±0.33	4.80	1.57±0.57	4.78	2.24±0.35
5.78	0.56±0.36			5.73	3.02±1.29

TABLE 22

ANGULAR DEPENDENCE OF K^-/K^+ TRIGGER RATIO IN π^--p COLLISIONS

90° (CM ANGLE)		79° (CM ANGLE)		67° (CM ANGLE)	
$P_\perp$ (GeV/c)	$\frac{K^-}{K^+}$	$P_\perp$ (GeV/c)	$\frac{K^-}{K^+}$	$P_\perp$ (GeV/c)	$\frac{K^-}{K^+}$
0.96	0.75±0.05				
1.44	0.78±0.03				
1.93	0.76±0.06			1.59	1.04±0.06
2.41	0.75±0.03	2.40	0.84±0.07	1.91	0.92±0.05
2.89	0.68±0.06	3.20	0.69±0.09	2.87	1.01±0.06
3.85	0.67±0.13	4.00	0.82±0.20	3.82	0.94±0.10
4.82	0.64±0.31	4.80	1.21±0.70	4.78	0.67±0.22
5.78	0.63±0.78			5.73	1.23±1.02

TABLE 23

ANGULAR DEPENDENCE OF $\bar{p}/p$ TRIGGER RATIO IN π^--p COLLISIONS

90° (CM ANGLE)		79° (CM ANGLE)		67° (CM ANGLE)	
$P_\perp$ (GeV/c)	$\frac{\bar{p}}{p}$	$P_\perp$ (GeV/c)	$\frac{\bar{p}}{p}$	$P_\perp$ (GeV/c)	$\frac{\bar{p}}{p}$
0.96	0.39±0.02				
1.44	0.41±0.01				
1.93	0.42±0.03			1.59	0.59±0.03
2.41	0.31±0.01	2.40	0.40±0.04	1.91	0.54±0.03
2.89	0.33±0.03	3.20	0.26±0.05	2.87	0.54±0.04
3.85	0.24±0.08	4.00	0.55±0.22	3.82	0.42±0.08
4.82	---------	4.80	---------	4.78	0.30±0.23
5.78	---------			5.73	---------

TABLE 24

ANGULAR DEPENDENCE OF K^+/π^+ TRIGGER RATIO IN π^--p COLLISIONS

90° (CM ANGLE)		79° (CM ANGLE)		67° (CM ANGLE)	
$P_\perp$ (GeV/c)	$\frac{K^+}{\pi^+}$	$P_\perp$ (GeV/c)	$\frac{K^+}{\pi^+}$	$P_\perp$ (GeV/c)	$\frac{K^+}{\pi^+}$
0.96	0.30±0.01				
1.44	0.32±0.01				
1.93	0.34±0.02			1.59	0.32±0.02
2.41	0.41±0.01	2.40	0.43±0.03	1.91	0.37±0.02
2.89	0.41±0.02	3.20	0.51±0.06	2.87	0.41±0.02
3.85	0.40±0.06	4.00	0.30±0.06	3.82	0.48±0.04
4.82	0.51±0.18	4.80	0.54±0.24	4.78	0.38±0.09
5.78	0.27±0.22			5.73	0.23±0.15

TABLE 25

ANGULAR DEPENDENCE OF K^-/π^- TRIGGER RATIO IN π^--p COLLISIONS

90° (CM ANGLE)		79° (CM ANGLE)		67° (CM ANGLE)	
$P_\perp$ (GeV/c)	$\frac{K^-}{\pi^-}$	$P_\perp$ (GeV/c)	$\frac{K^-}{\pi^-}$	$P_\perp$ (GeV/c)	$\frac{K^-}{\pi^-}$
0.96	0.19±0.01				
1.44	0.21±0.01				
1.93	0.23±0.02			1.59	0.25±0.01
2.41	0.26±0.01	2.40	0.28±0.02	1.91	0.24±0.01
2.89	0.24±0.02	3.20	0.24±0.03	2.87	0.27±0.01
3.85	0.28±0.05	4.00	0.20±0.04	3.82	0.27±0.02
4.82	0.26±0.10	4.80	0.41±0.22	4.78	0.11±0.03
5.78	0.30±0.34			5.73	0.09±0.06

TABLE 26

INVARIANT CROSS SECTIONS $Ed^3\sigma/dp^3(cm^2/GeV^2)$ per nucleus

BEAM: 200 GeV π^- : TARGET: Tungsten : CM ANGLE: 90°

Particle Produced	π^+	π^-	K^+	K^-	p	$\bar{p}$
$P_\perp$(GeV/c)						
0.96	$3.76\pm0.31\times10^{-26}$	$4.35\pm0.35\times10^{-26}$	$1.37\pm0.12\times10^{-26}$	$1.05\pm0.09\times10^{-26}$	$1.71\pm0.14\times10^{-26}$	$4.48\pm0.39\times10^{-27}$
1.44	$4.12\pm0.34\times10^{-27}$	$4.92\pm0.40\times10^{-27}$	$1.58\pm0.14\times10^{-27}$	$1.24\pm0.11\times10^{-27}$	$2.33\pm0.19\times10^{-27}$	$7.48\pm0.63\times10^{-28}$
1.93	$5.33\pm0.43\times10^{-28}$	$6.87\pm0.56\times10^{-28}$	$2.31\pm0.20\times10^{-28}$	$1.82\pm0.16\times10^{-28}$	$3.59\pm0.29\times10^{-28}$	$1.04\pm0.09\times10^{-28}$
2.41	$7.67\pm0.35\times10^{-29}$	$1.04\pm0.47\times10^{-28}$	$3.73\pm0.18\times10^{-29}$	$2.77\pm0.13\times10^{-29}$	$4.83\pm0.22\times10^{-29}$	$1.38\pm0.07\times10^{-29}$
2.89	$1.26\pm0.06\times10^{-29}$	$1.71\pm0.08\times10^{-29}$	$6.34\pm0.38\times10^{-30}$	$5.17\pm0.32\times10^{-30}$	$7.23\pm0.40\times10^{-30}$	$1.87\pm0.14\times10^{-30}$
3.85	$3.95\pm0.23\times10^{-31}$	$6.31\pm0.36\times10^{-31}$	$2.28\pm0.16\times10^{-31}$	$1.54\pm0.14\times10^{-31}$	$2.12\pm0.15\times10^{-31}$	$5.24\pm0.67\times10^{-32}$
4.82	$1.70\pm0.15\times10^{-32}$	$3.06\pm0.24\times10^{-32}$	$9.20\pm1.06\times10^{-33}$	$7.60\pm1.10\times10^{-33}$	$6.06\pm0.77\times10^{-33}$	$1.60\pm0.48\times10^{-33}$
5.78	$4.66\pm1.33\times10^{-34}$	$1.34\pm0.26\times10^{-33}$	$5.74\pm1.64\times10^{-34}$	$3.81\pm1.47\times10^{-34}$	$1.84\pm0.83\times10^{-34}$	----------

TABLE 27

INVARIANT CROSS SECTIONS $Ed^3\sigma/dp^3(cm^2/GeV^2)$ per nucleus

BEAM: 200 GeV π^- : TARGET: Beryllium : CM ANGLE: 90°

Particle Produced	π^+	π^-	K^+	K^-	p	$\bar{p}$
$P_\perp$(GeV/c)						
0.96	$2.68\pm0.22\times10^{-27}$	$3.40\pm0.28\times10^{-27}$	$7.55\pm0.69\times10^{-28}$	$6.10\pm0.58\times10^{-28}$	$9.46\pm0.79\times10^{-28}$	$3.40\pm0.31\times10^{-28}$
1.44	$2.42\pm0.20\times10^{-28}$	$3.18\pm0.26\times10^{-28}$	$8.25\pm0.70\times10^{-29}$	$6.37\pm0.54\times10^{-29}$	$1.14\pm0.09\times10^{-28}$	$4.53\pm0.38\times10^{-29}$
1.93	$2.82\pm0.23\times10^{-29}$	$3.53\pm0.28\times10^{-29}$	$1.04\pm0.09\times10^{-29}$	$8.89\pm0.74\times10^{-30}$	$1.44\pm0.12\times10^{-29}$	$5.12\pm0.43\times10^{-30}$
2.41	$3.21\pm0.15\times10^{-30}$	$4.60\pm0.21\times10^{-30}$	$1.40\pm0.07\times10^{-30}$	$1.13\pm0.06\times10^{-30}$	$1.47\pm0.07\times10^{-30}$	$5.02\pm0.29\times10^{-31}$
2.89	$4.32\pm0.26\times10^{-31}$	$6.73\pm0.38\times10^{-31}$	$2.22\pm0.17\times10^{-31}$	$1.69\pm0.15\times10^{-31}$	$1.89\pm0.14\times10^{-31}$	$4.65\pm0.61\times10^{-32}$
3.85	$1.76\pm0.27\times10^{-32}$	$2.21\pm0.30\times10^{-32}$	$6.92\pm1.77\times10^{-33}$	$7.47\pm1.85\times10^{-33}$	$7.63\pm1.76\times10^{-33}$	$2.72\pm2.74\times10^{-34}$
4.82	$1.01\pm0.30\times10^{-33}$	$1.21\pm0.33\times10^{-33}$	$3.82\pm1.94\times10^{-34}$	$3.18\pm1.86\times10^{-34}$	$9.15\pm9.13\times10^{-35}$	----------
5.78	$1.23\pm1.24\times10^{-35}$	$7.55\pm3.85\times10^{-35}$	----------	----------	----------	----------

TABLE 28

INVARIANT CROSS SECTIONS $Ed^3\sigma/dp^3(cm^2/GeV^2)$ per nucleus

BEAM: 200 GeV π^- : TARGET: Copper : CM ANGLE: 90°

Particle Produced	π^+	π^-	K^+	K^-	p	$\bar{p}$
$P_\perp$(GeV/c)						
0.96	----------	----------	----------	----------	----------	----------
1.44	----------	----------	----------	----------	----------	----------
1.93	----------	----------	----------	----------	----------	----------
2.40	$2.31\pm0.11\times10^{-29}$	$3.13\pm0.15\times10^{-29}$	$1.12\pm0.06\times10^{-29}$	$8.16\pm0.44\times10^{-30}$	$1.36\pm0.07\times10^{-29}$	$4.10\pm0.23\times10^{-30}$
2.89	$3.94\pm0.20\times10^{-30}$	$5.56\pm0.27\times10^{-30}$	$1.98\pm0.12\times10^{-30}$	$1.40\pm0.09\times10^{-30}$	$2.14\pm0.12\times10^{-30}$	$6.30\pm0.47\times10^{-31}$
3.85	----------	----------	----------	----------	----------	----------
4.82	----------	----------	----------	----------	----------	----------
5.78	----------	----------	----------	----------	----------	----------

TABLE 29

INVARIANT CROSS SECTIONS $Ed^3\sigma/dp^3(cm^2/GeV^2)$ per nucleus

BEAM: 300 GeV π^- : TARGET: Tungsten : CM ANGLE: 90°

Particle Produced	π^+	π^-	K^+	K^-	p	$\bar{p}$
P(GeV/c)						
0.80	$1.01\pm0.08\times10^{-25}$	$1.13\pm0.09\times10^{-25}$	$2.99\pm0.29\times10^{-26}$	$2.67\pm0.26\times10^{-26}$	$3.39\pm0.29\times10^{-26}$	$1.04\pm0.10\times10^{-26}$
1.20	$1.45\pm0.12\times10^{-26}$	$1.66\pm0.14\times10^{-26}$	$5.12\pm0.45\times10^{-27}$	$3.98\pm0.35\times10^{-27}$	$6.74\pm0.56\times10^{-27}$	$2.53\pm0.22\times10^{-27}$
1.60	$2.52\pm0.21\times10^{-27}$	$3.06\pm0.25\times10^{-27}$	$1.05\pm0.09\times10^{-27}$	$8.71\pm0.75\times10^{-28}$	$1.37\pm0.11\times10^{-27}$	$5.29\pm0.46\times10^{-28}$
2.00	$5.10\pm0.25\times10^{-28}$	$6.62\pm0.32\times10^{-28}$	$2.22\pm0.12\times10^{-28}$	$1.85\pm0.11\times10^{-28}$	$2.98\pm0.15\times10^{-28}$	$1.14\pm0.07\times10^{-28}$
2.40	$1.24\pm0.06\times10^{-28}$	$1.63\pm0.08\times10^{-28}$	$5.63\pm0.34\times10^{-29}$	$4.47\pm0.28\times10^{-29}$	$7.01\pm0.38\times10^{-29}$	$2.47\pm0.17\times10^{-29}$
3.20	$7.17\pm0.43\times10^{-30}$	$1.01\pm0.06\times10^{-29}$	$3.71\pm0.28\times10^{-30}$	$3.45\pm0.27\times10^{-30}$	$3.72\pm0.27\times10^{-30}$	$1.20\pm0.13\times10^{-30}$
4.00	$6.38\pm0.43\times10^{-31}$	$8.75\pm0.53\times10^{-31}$	$3.09\pm0.27\times10^{-31}$	$2.48\pm0.23\times10^{-31}$	$2.61\pm0.23\times10^{-31}$	$6.90\pm1.02\times10^{-32}$
4.80	$5.63\pm0.61\times10^{-32}$	$7.91\pm0.82\times10^{-32}$	$2.22\pm0.36\times10^{-32}$	$2.82\pm0.48\times10^{-32}$	$1.72\pm0.31\times10^{-32}$	$3.36\pm1.53\times10^{-33}$
5.60	----------	$9.71\pm1.76\times10^{-33}$	----------	$1.97\pm0.76\times10^{-33}$	----------	----------
6.40	----------	$1.60\pm0.40\times10^{-33}$	----------	----------	----------	----------

TABLE 30

THE EXPONENT $\alpha_i(P_i)$ FOR THE PRODUCTION OF HADRONS WITH 200 GeV π^-'s

P_i (GeV/c)	α_{π^+}	α_{π^-}	α_{K^+}	α_{K^-}	α_p	$\alpha_{\bar{p}}$
0.96	0.88±0.01	0.85±0.01	0.96±0.02	0.94±0.02	0.96±0.01	0.86±0.02
1.44	0.94±0.01	0.91±0.01	0.98±0.02	0.98±0.02	1.00±0.01	0.93±0.02
1.93	0.97±0.01	0.99±0.01	1.03±0.02	1.00±0.02	1.07±0.01	1.00±0.02
2.41	1.05±0.01	1.03±0.01	1.09±0.01	1.06±0.01	1.16±0.01	1.10±0.02
2.89	1.12±0.02	1.07±0.02	1.11±0.03	1.13±0.03	1.21±0.02	1.22±0.05
3.85	1.03±0.05	1.11±0.04	1.16±0.09	1.00±0.09	1.10±0.08	1.74±0.34
4.82	.94±0.10	1.10±0.09	1.06±0.17	1.05±0.20	1.39±0.33	---------
5.78	1.21±0.35	0.99±0.18	---------	---------	---------	---------

Figure 1.--Diagram of deep inelastic electron proton scattering.

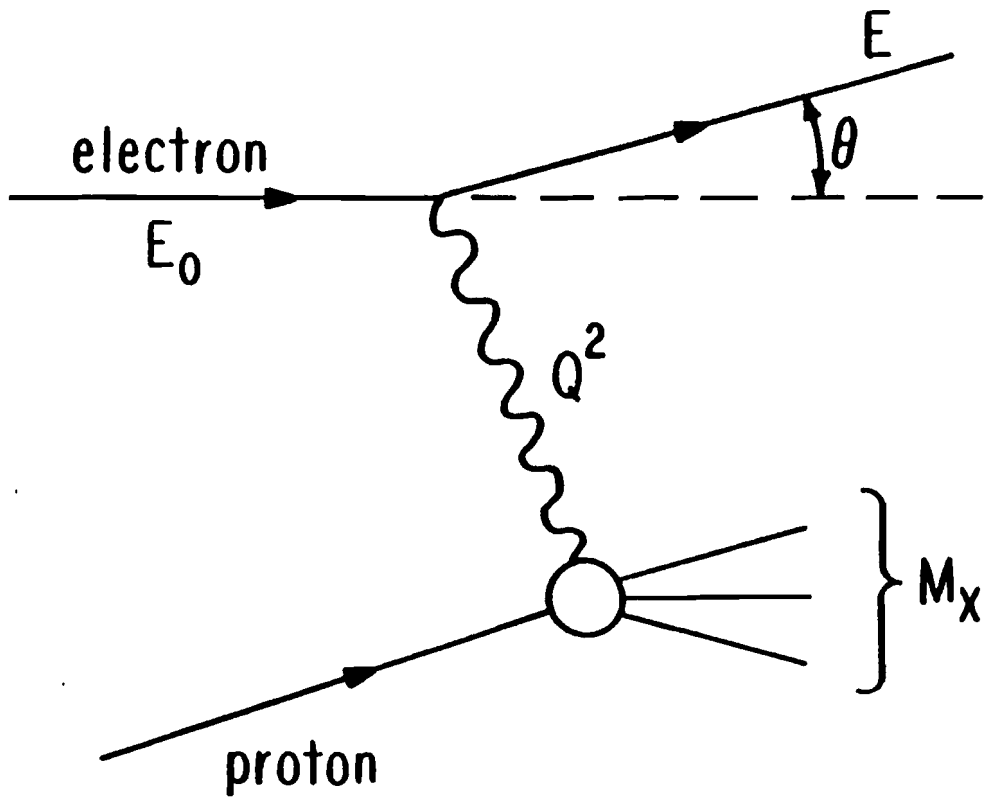
E
electron
θ
E_0
Q^2
M_X
proton

Figure 2.--Illustration of hard scattering models of large $P_\perp$ hadronic processes (From Reference 18).

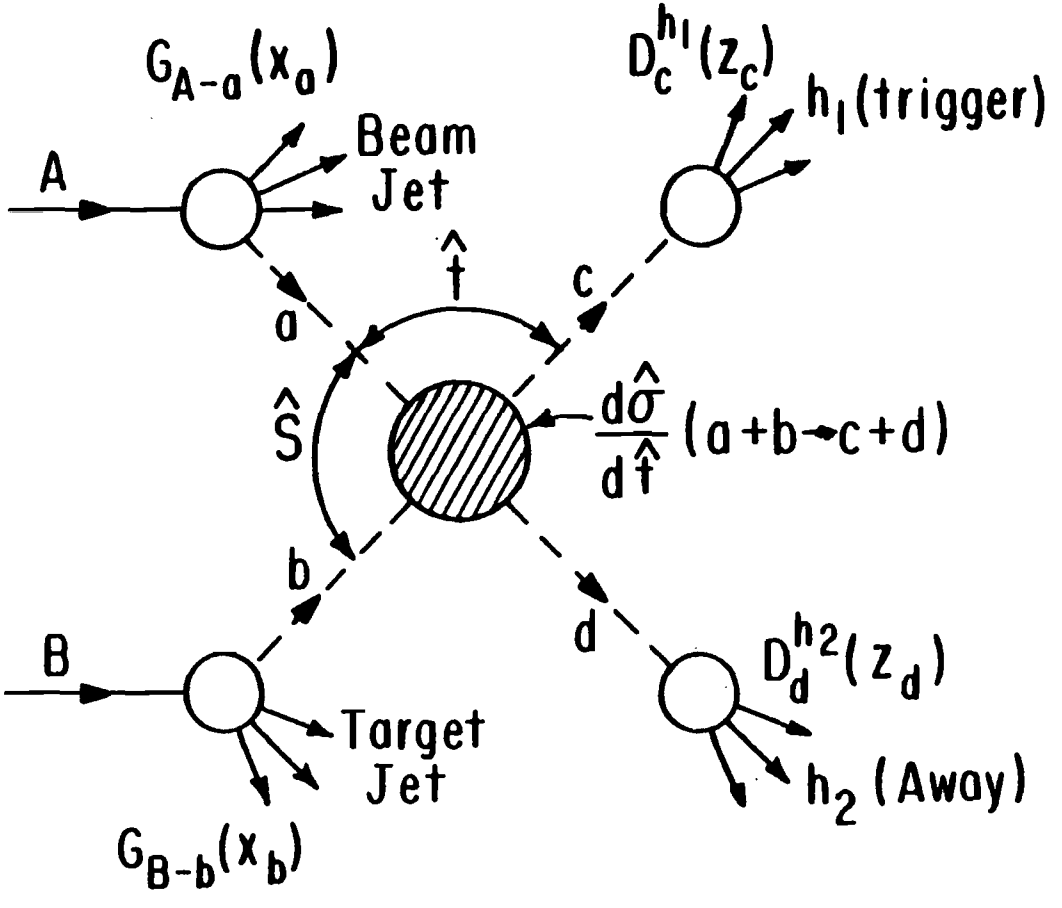
$G_{A-a}(x_a)$
A
Beam Jet
a
$\hat{t}$
c
$D_c^{h_1}(z_c)$
h_1(trigger)
$\hat{S}$
$\frac{d\hat{\sigma}}{d\hat{t}}(a+b\to c+d)$
b
B
Target Jet
$G_{B-b}(x_b)$
d
$D_d^{h_2}(z_d)$
h_2 (Away)

Figure 3.--Constituent Interchange Model (CIM) type diagram for high transverse momentum processes.

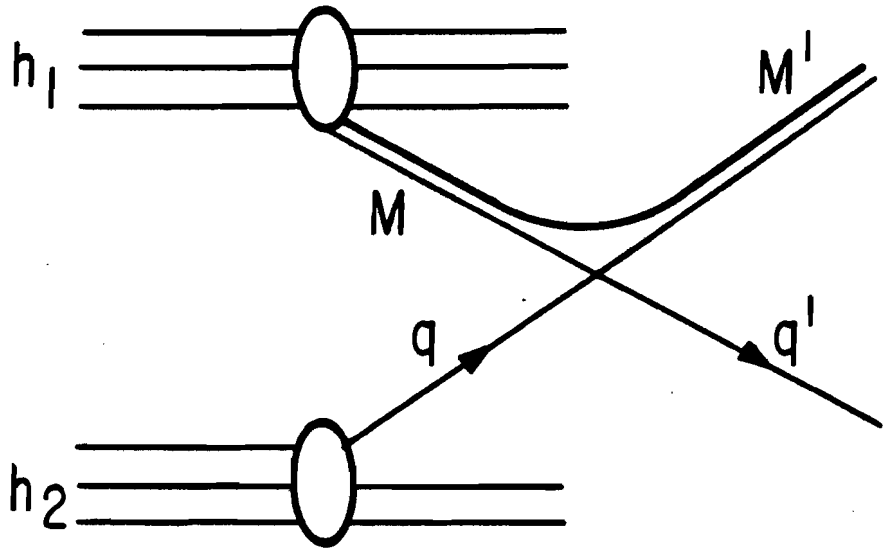

h_1 , h_2 : Hadrons

M , M' : Mesons

q , q' : quarks

Figure 4.--The invariant cross section for inclusive π° production versus $x_\parallel$ in $\pi^- p$ and pp collisions at 200 GeV (Reference 30). For display purposes, the cross sections in alternate $P_\perp$ intervals are labelled. The curves are parametrizations of the data points to the form: $E\, d^3\sigma/dp^3 = A(1-x_b)^m/(P^2+M^2)^n$, where $x_D = [x_\perp^2+(x_\parallel-x_0)^2]^{1/2}$ with x_0 the value of $x_\parallel$ at the peak in the $x_\parallel$ distribution. The parameters A, M, x_0, m and n are determined from the fit (this Figure was taken from Reference 30).

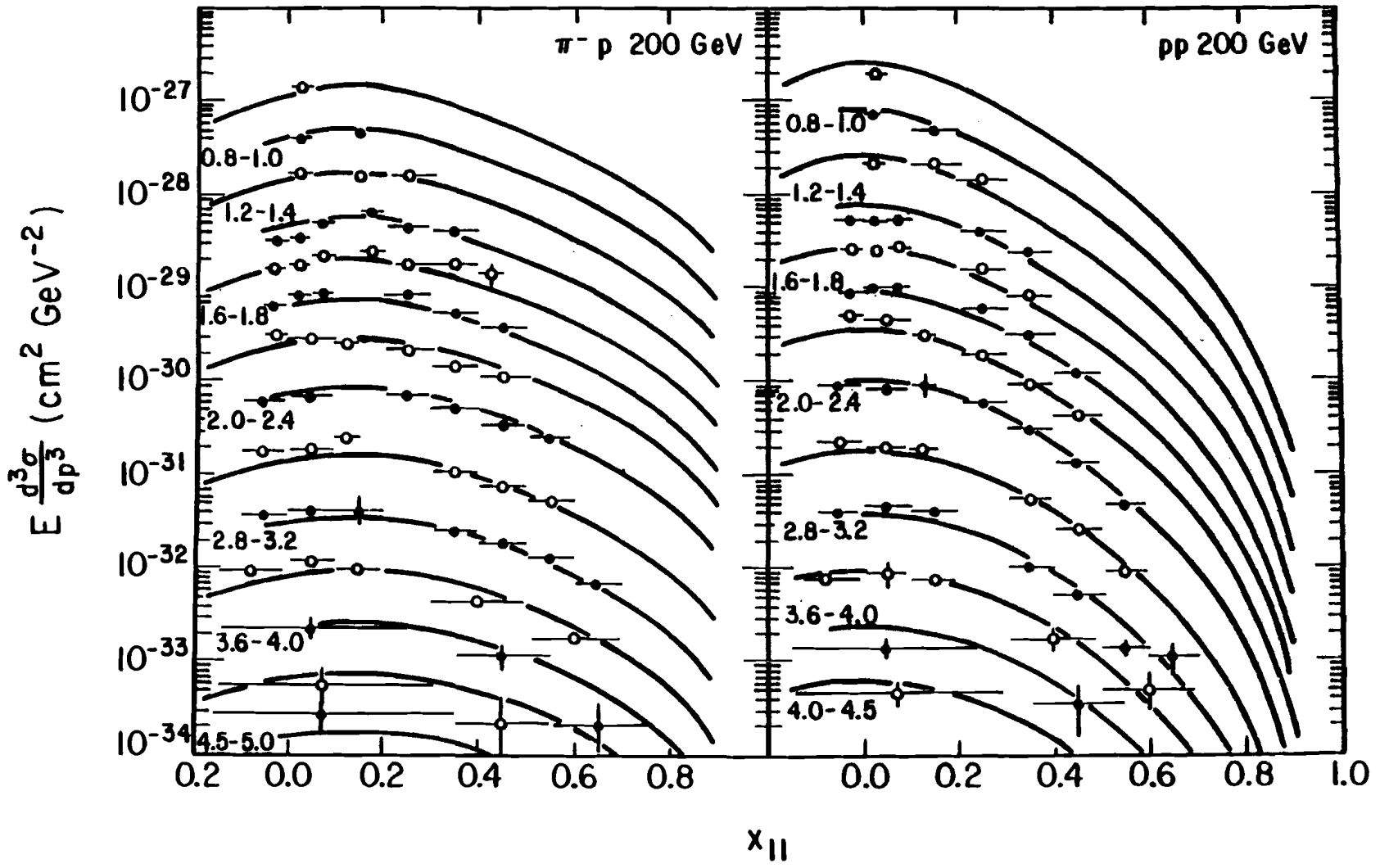
π⁻ p 200 GeV
pp 200 GeV
0.8-1.0
1.2-1.4
1.6-1.8
2.0-2.4
2.8-3.2
3.6-4.0
4.0-4.5
4.5-5.0
$E\frac{d^3\sigma}{dp^3}$ (cm^2 GeV^{-2})
10^{-27}
10^{-28}
10^{-29}
10^{-30}
10^{-31}
10^{-32}
10^{-33}
10^{-34}
0.2
0.0
0.2
0.4
0.6
0.8
1.0
$x_{\parallel}$

Figure 5.--Invariant cross section for inclusive π° production in pp collisions at $\sqrt{s}$ = 53 GeV versus the center of mass angle (Reference 27). Solid circles are data at $P_{\perp}$ = 3 GeV/c and open circles are data at $P_{\perp}$ = 4 GeV/c. The curves are predictions of the FFF model (this Figure was taken from Reference 27).

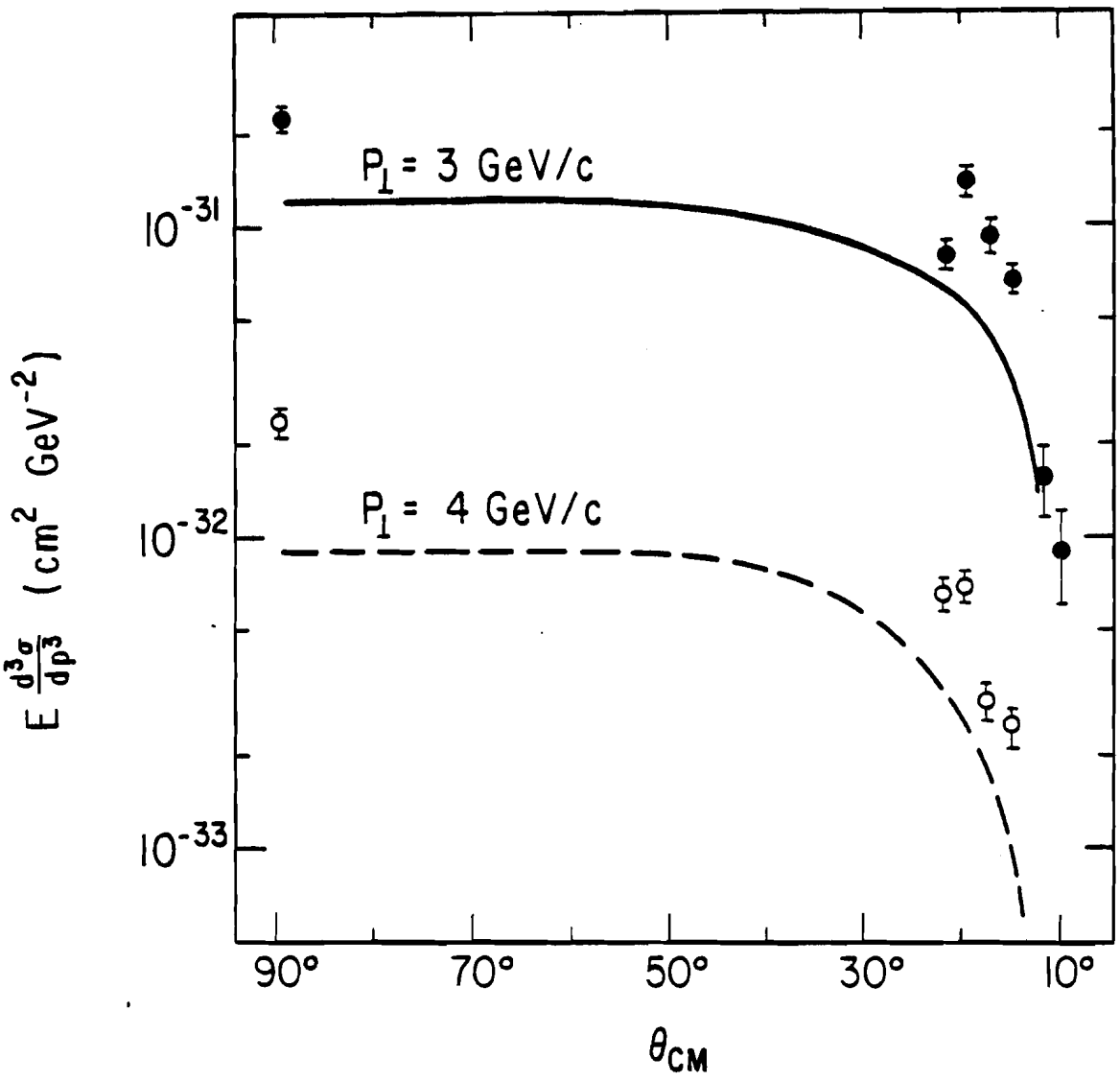
$P_\perp$ = 3 GeV/c
$P_\perp$ = 4 GeV/c
10^{-31}
10^{-32}
10^{-33}
$E\frac{d^3\sigma}{dp^3}$ (cm^2 GeV^{-2})
90°
70°
50°
30°
10°
θ_{CM}

Figure 6.--Proton West High Intensity Secondary Beam Line at FNAL. Both the dimensions and the bending angles have not been drawn to scale. Magnets connected with the same line were connected electrically in series.

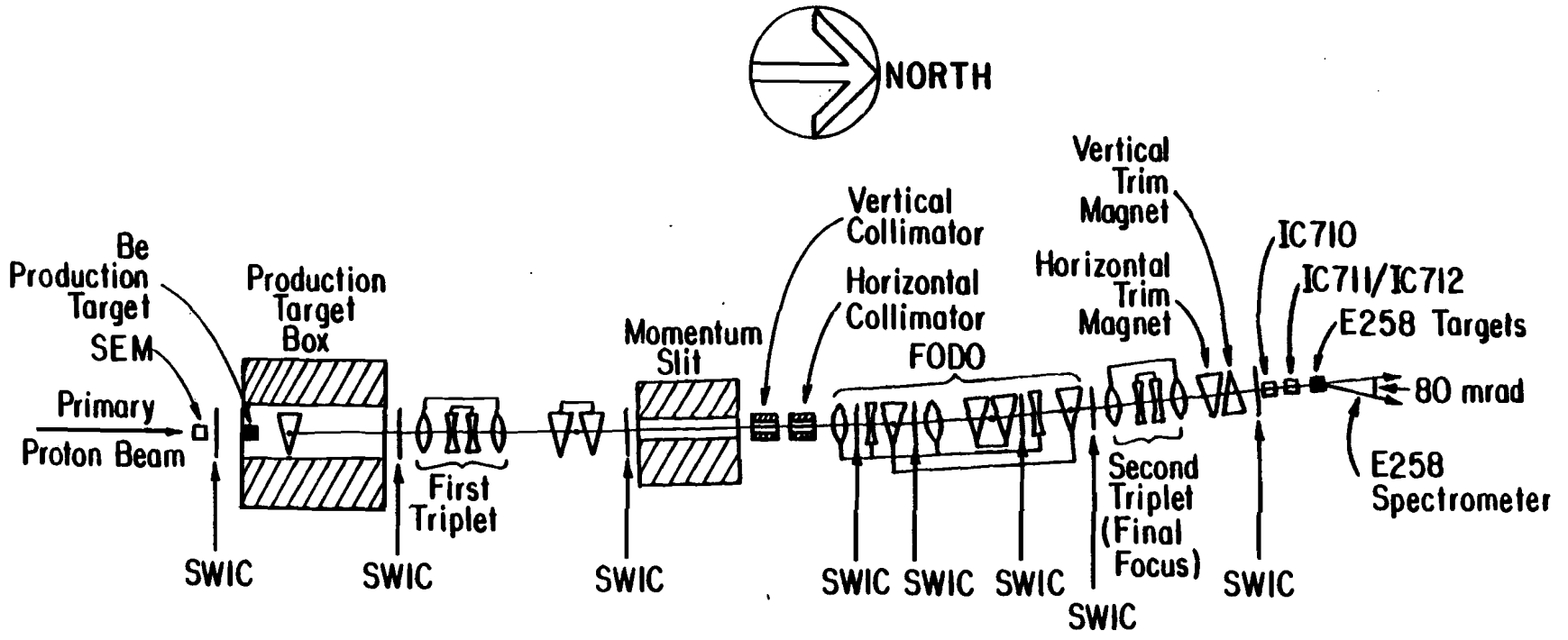

Quadrupole Focussing in the Horizontal Plane

Quadrupole Focussing in the Vertical Plane

Dipole

Steel Collimator

Figure 7.--Momentum bite of the secondary π^- beam at the experimental target as obtained by the Halo Monte Carlo program (Reference 49). The central momentum of the beam was 200 GeV/c. The average momentum of the distribution is 202 GeV/c and its sigma is 10 GeV/c. Therefore the momentum bite is ~10% (RMSFW).

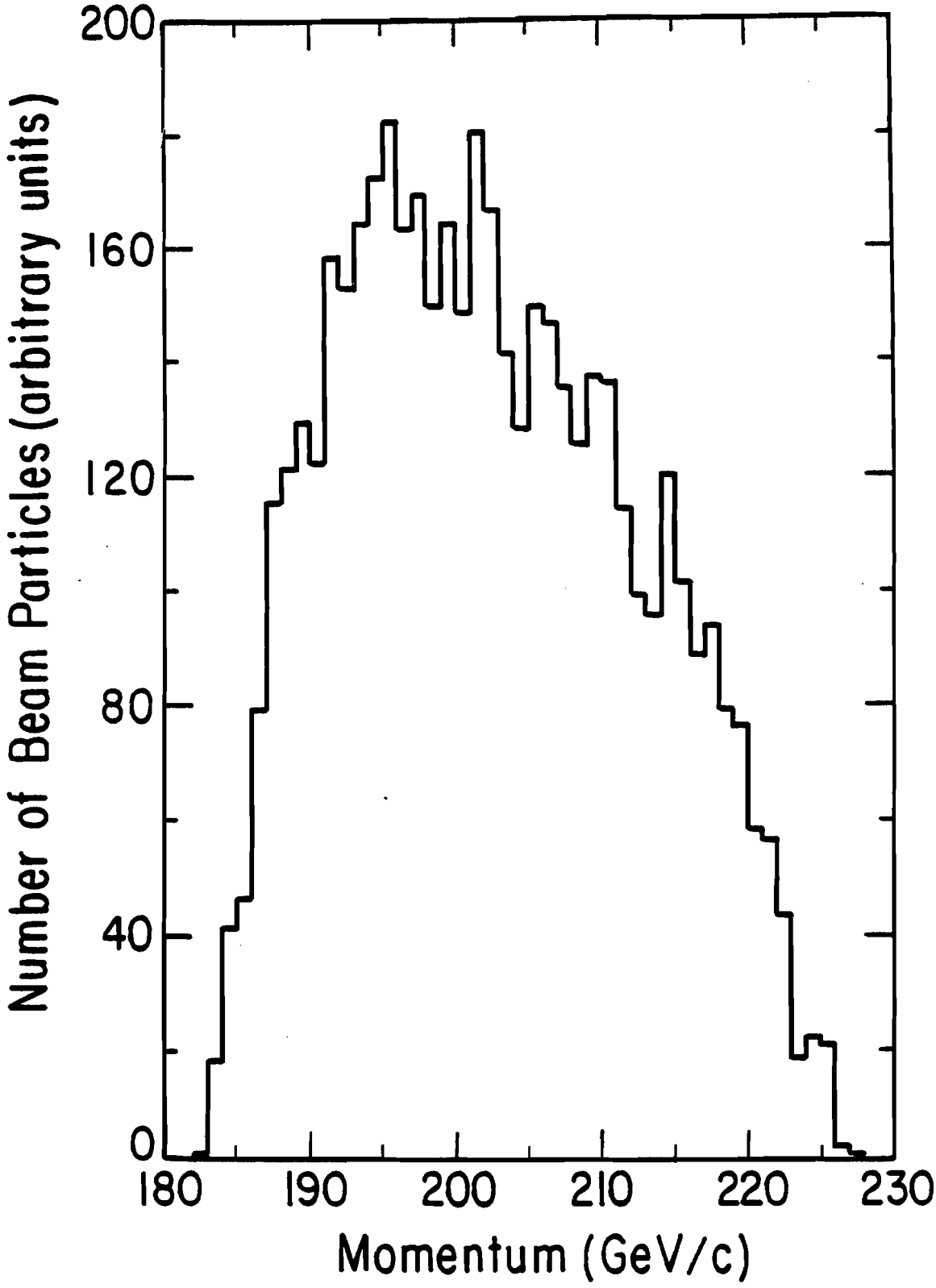
200
160
120
80
40
0
Number of Beam Particles (arbitrary units)
180
190
200
210
220
230
Momentum (GeV/c)

Figure 8.--Detail of the surrounding of the experimental target area.

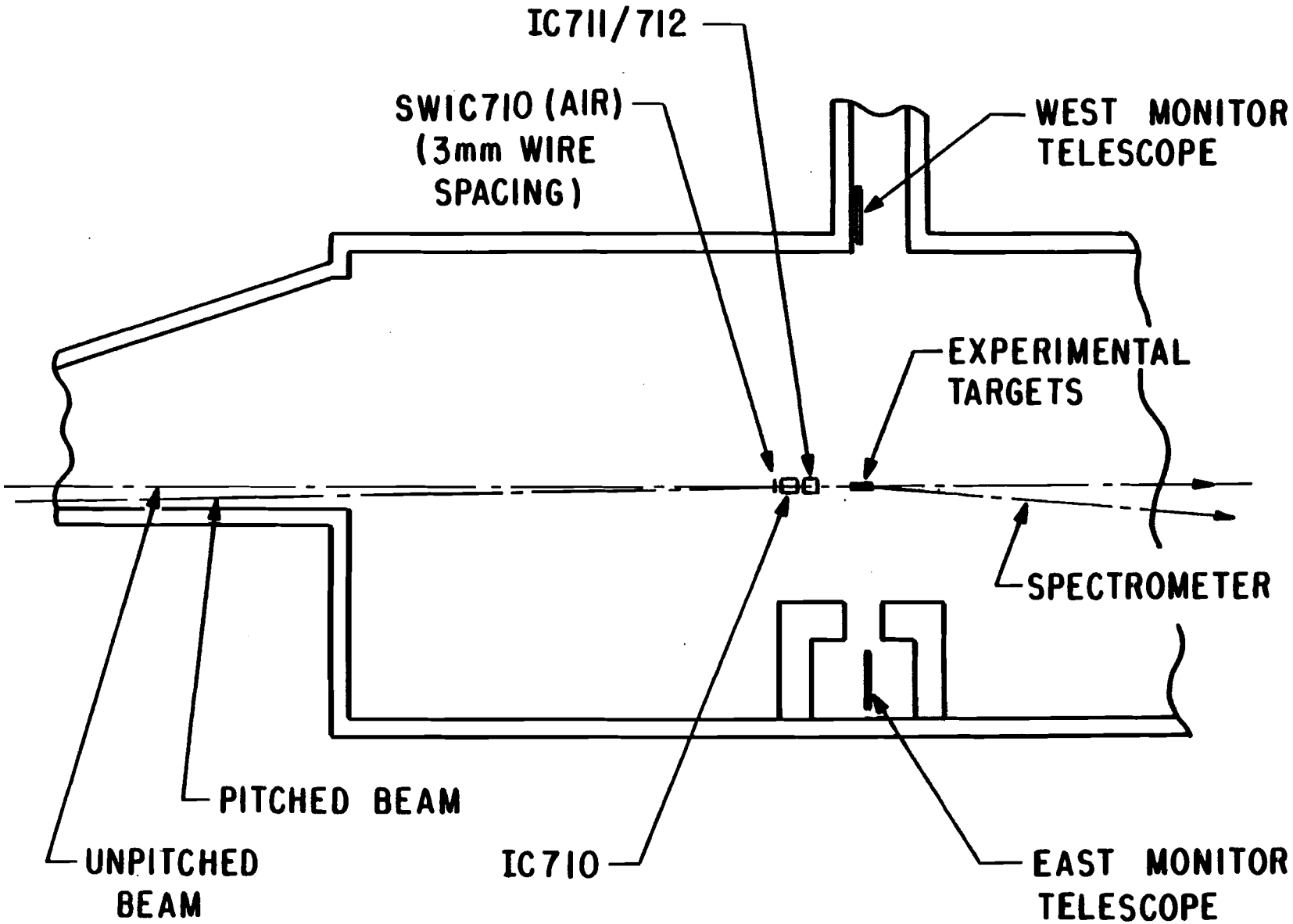
IC711/712
SWIC710 (AIR)
(3mm WIRE
SPACING)
WEST MONITOR
TELESCOPE
EXPERIMENTAL
TARGETS
SPECTROMETER
PITCHED BEAM
UNPITCHED
BEAM
IC710
EAST MONITOR
TELESCOPE

Figure 9.--E258 spectrometer.

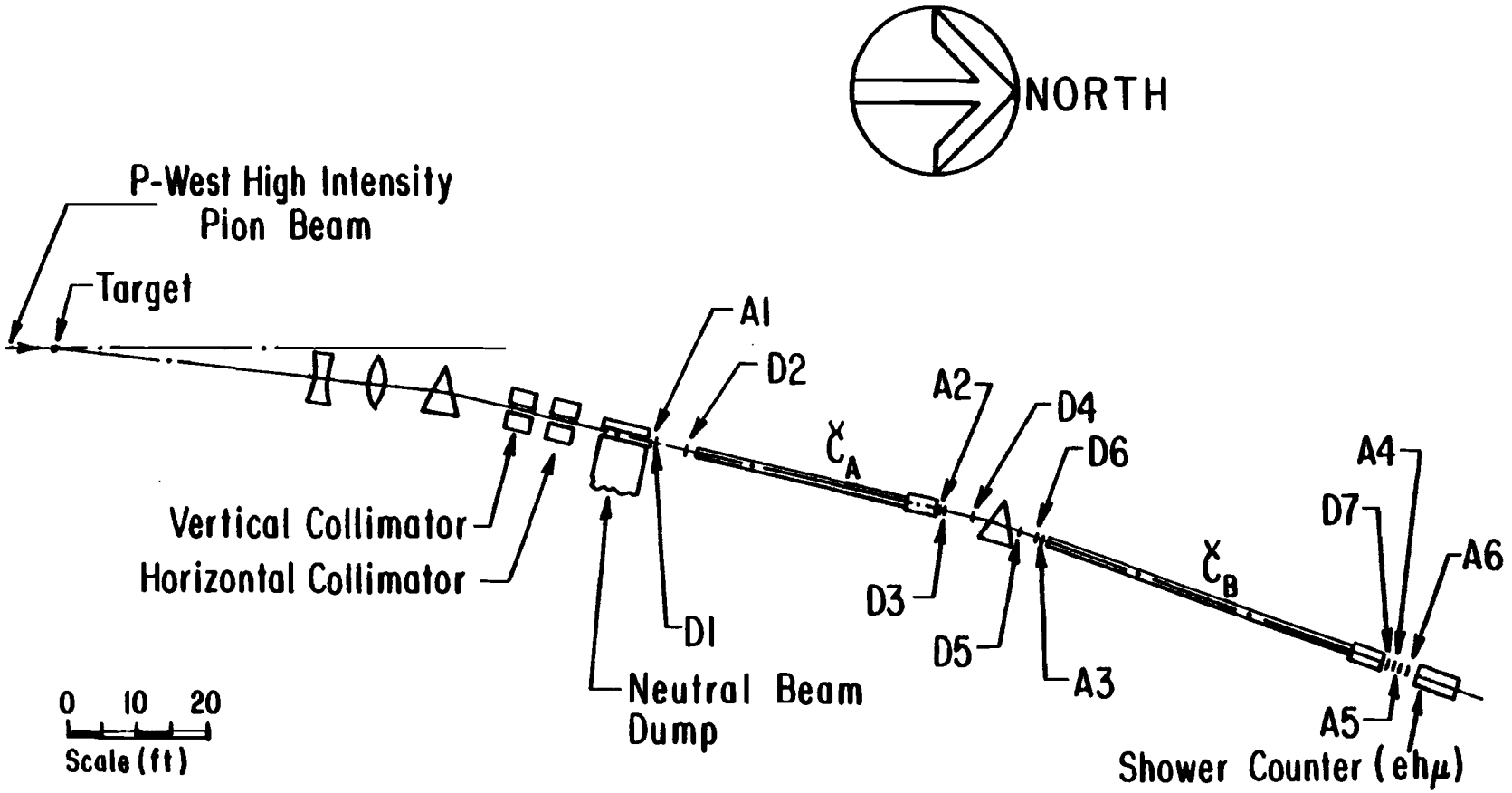

◊ Quadrupole Focussing in the Horizontal Plane

▯ Quadrupole Focussing in the Vertical Plane

▽ Dipole

Figure 10.--The liquid hydrogen target.

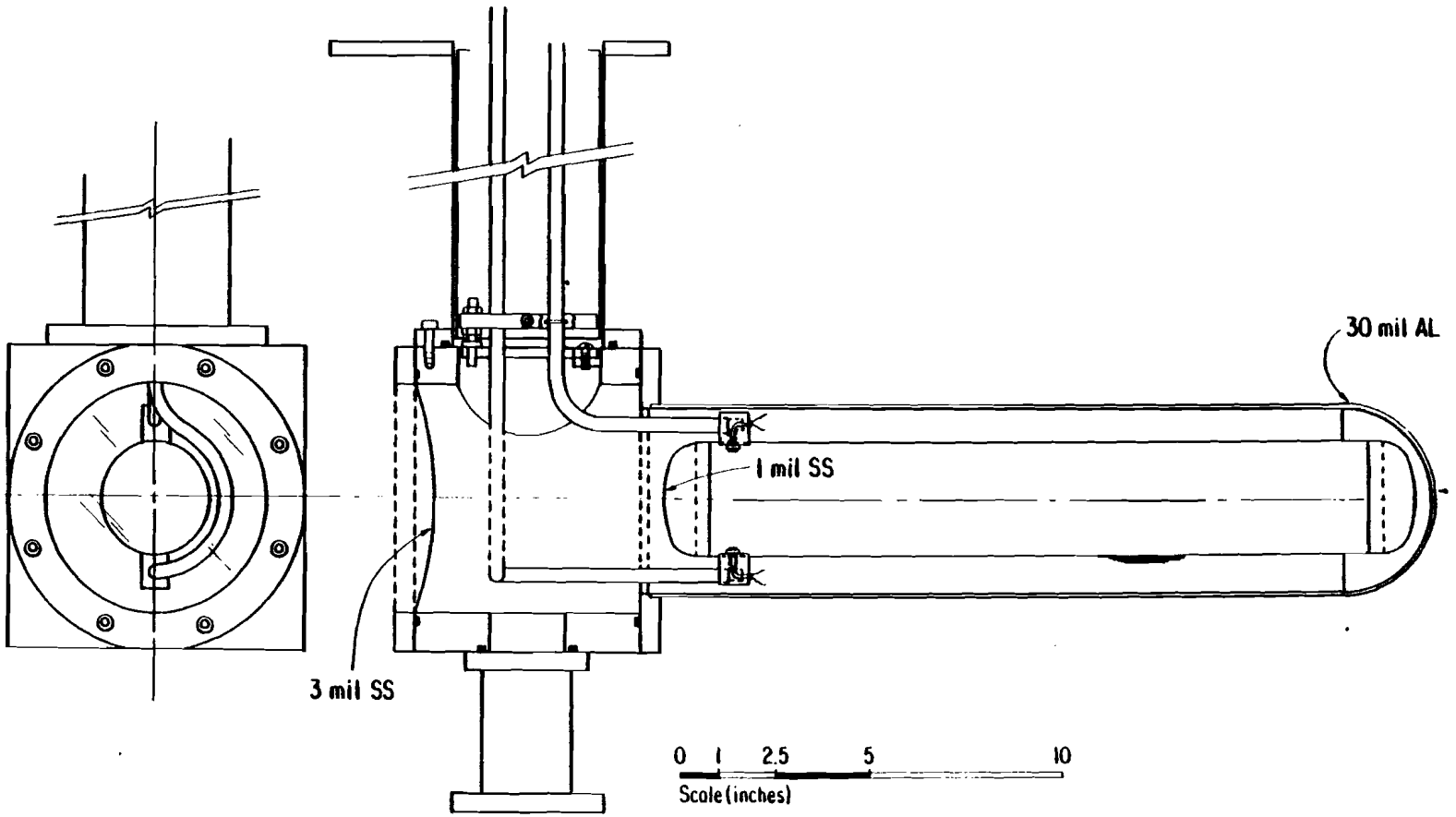
30 mil AL
1 mil SS
15 mil AL
3 mil SS
0 1 2.5 5 10
Scale (inches)

Figure 11.--Two dimensional Čerenkov counter plot for a -25 GeV/c run with the W target.

ČA1 is the inner channel of counter ČA
ČA2 is the outer channel of counter ČA
ČB1 is the inner channel of counter ČB
ČB2 is the outer channel of counter ČB

For an explanation of what the ERRORS are see page 37.

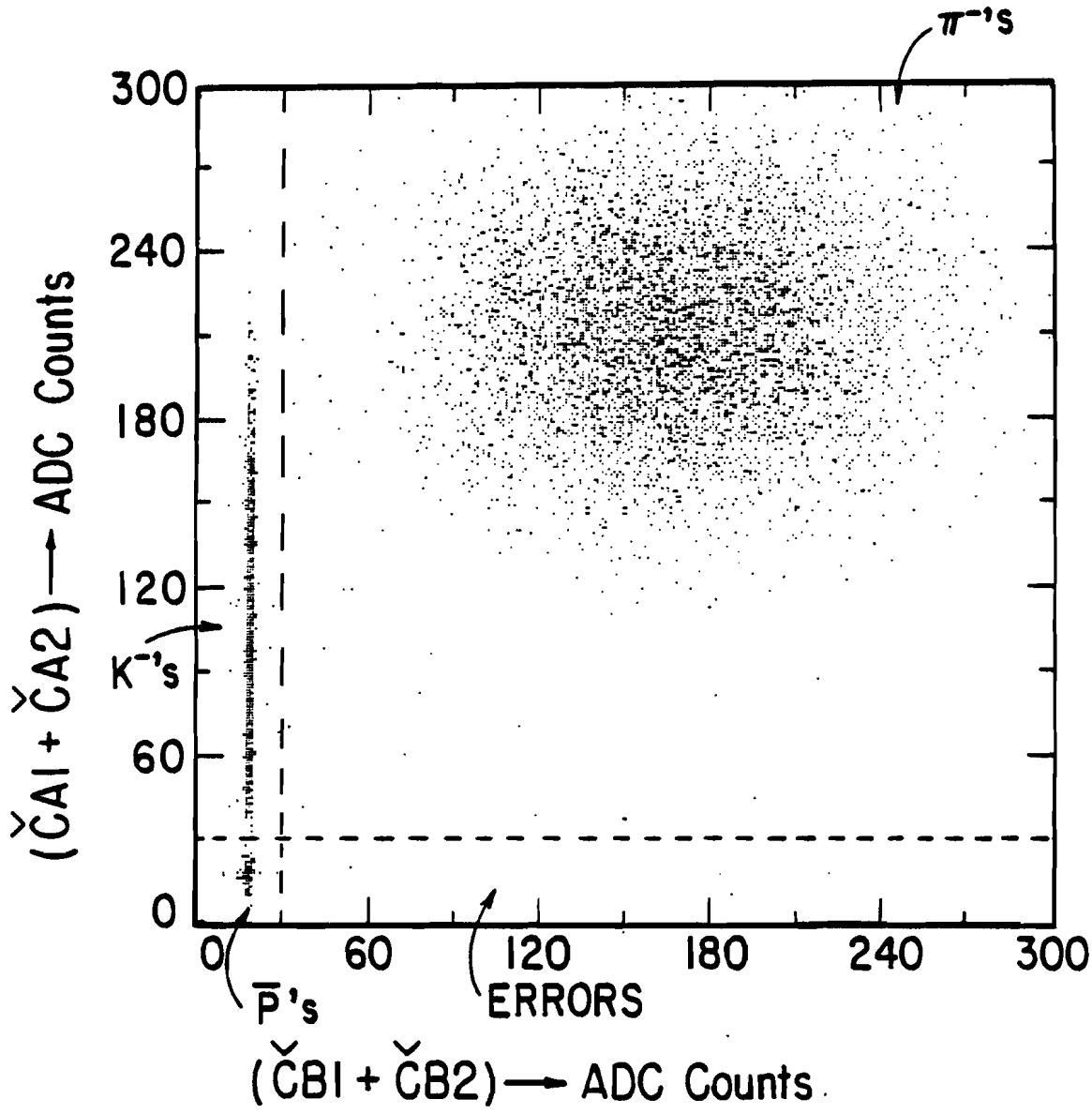
π^{-}'s
300
240
180
120
60
0
K^{-}'s
$(\check{C}A1 + \check{C}A2) \rightarrow$ ADC Counts
0
60
120
180
240
300
$\bar{p}$'s
ERRORS
$(\check{C}B1 + \check{C}B2) \rightarrow$ ADC Counts

Figure 12.--Two dimensional Čerenkov counter plot for a -15 GeV/c run with the W target (For an explanation of the symbols see Figure 11).

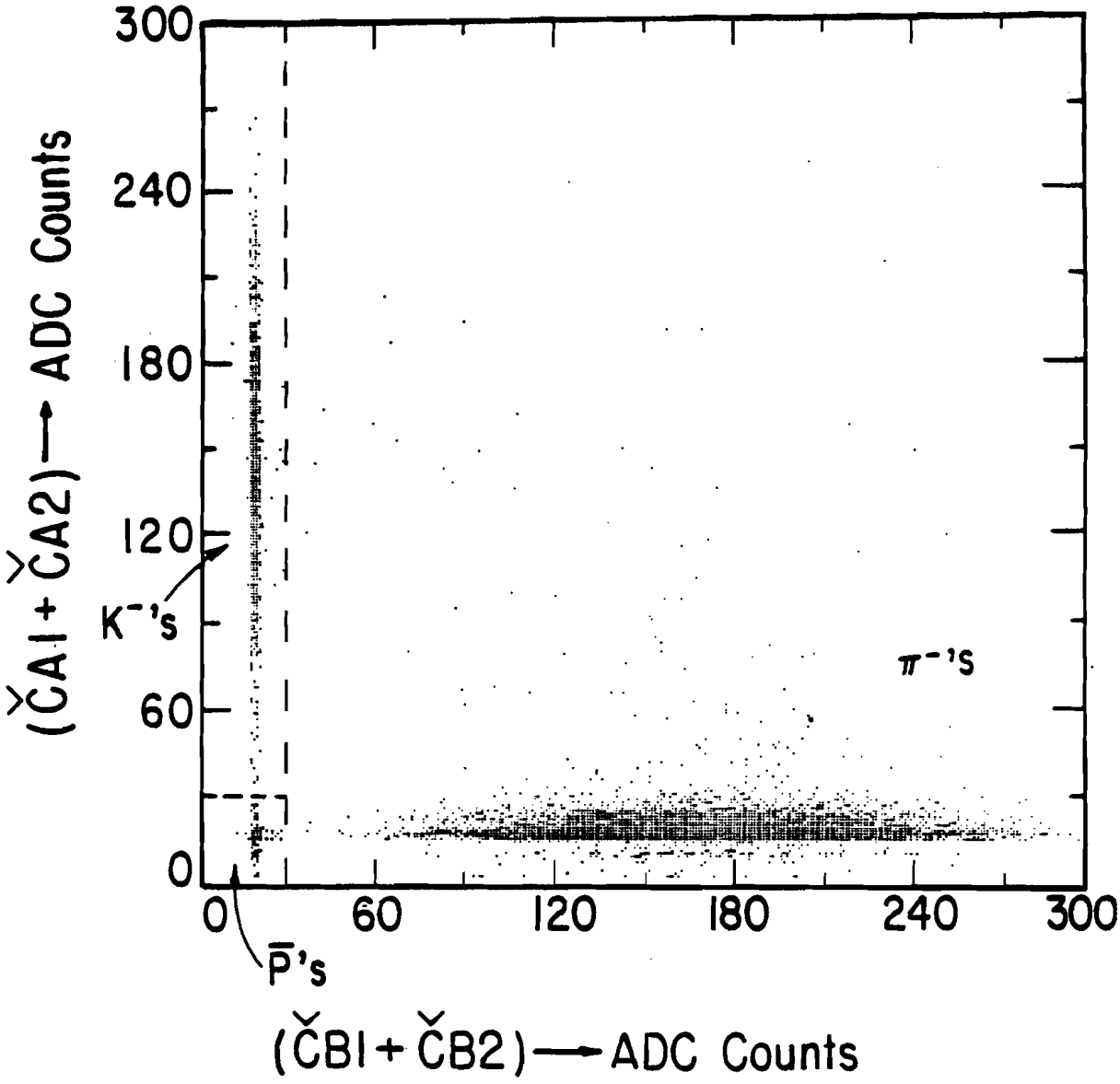
300
240
180
120
60
0
0
60
120
180
240
300
(ČA1 + ČA2) → ADC Counts
(ČB1 + ČB2) → ADC Counts
K⁻'s
π⁻'s
P̄'s

Figure 13.--Electron, hadron, muon identifier (ehμ).

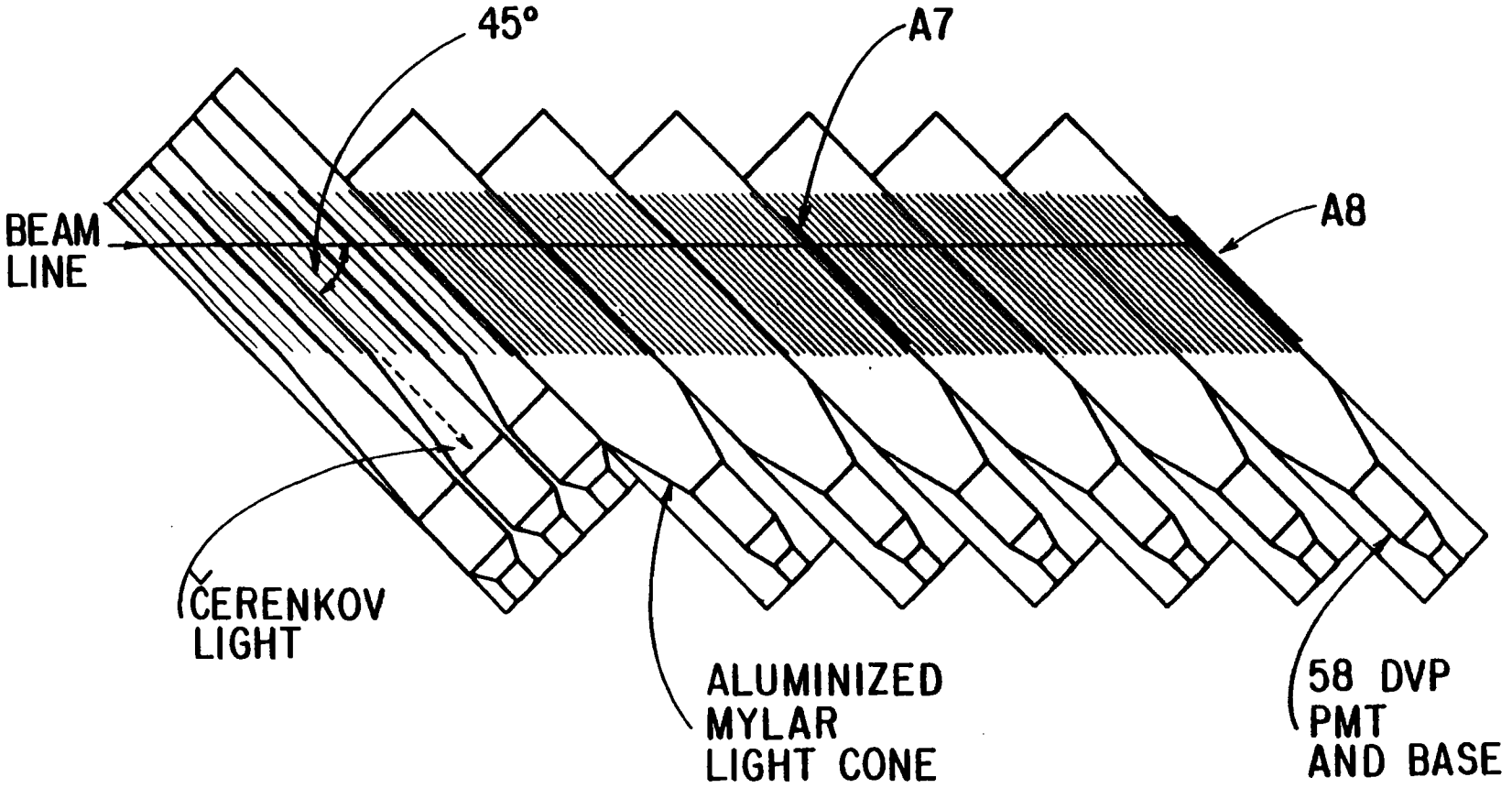
45°
A7
A8
BEAM
LINE
CERENKOV
LIGHT
ALUMINIZED
MYLAR
LIGHT CONE
58 DVP
PMT
AND BASE

Figure 14.--Plot of the number of triggers divided by the number of beam particles as a function of run number for a series of runs with the hydrogen target. The spectrometer momentum was set at -25 GeV/c. The vertical scale is arbitrary.

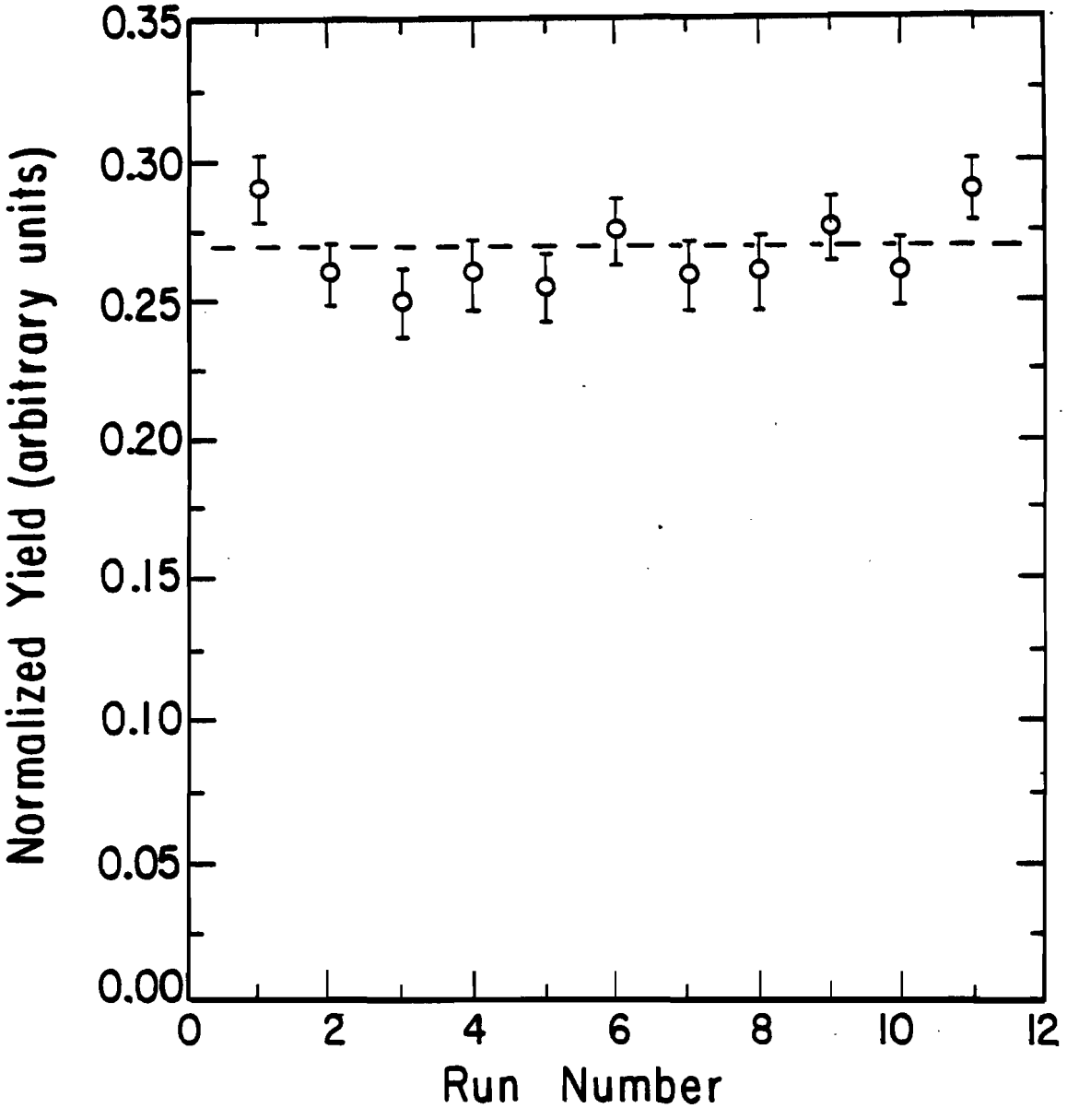
0.35
0.30
0.25
0.20
0.15
0.10
0.05
0.00
Normalized Yield (arbitrary units)
0
2
4
6
8
10
12
Run Number

Figure 15.--Logic diagram of the trigger electronics.

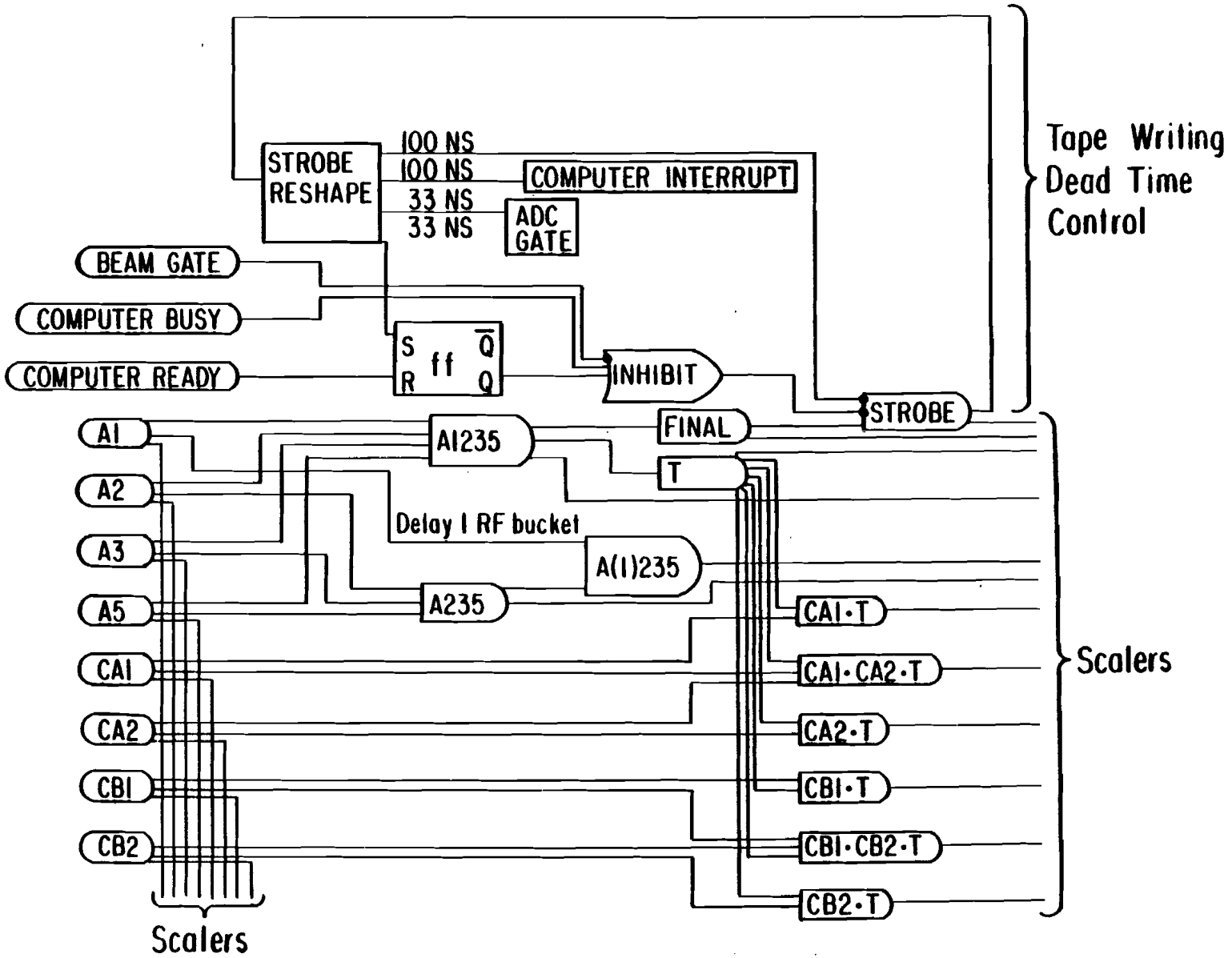
STROBE RESHAPE
100 NS
100 NS
33 NS
33 NS
COMPUTER INTERRUPT
ADC GATE
BEAM GATE
COMPUTER BUSY
COMPUTER READY
S
R
ff
Q̄
Q
INHIBIT
STROBE
Tape Writing Dead Time Control
A1
A2
A3
A5
CA1
CA2
CB1
CB2
A1235
FINAL
T
Delay 1 RF bucket
A(1)235
A235
CA1·T
CA1·CA2·T
CA2·T
CB1·T
CB1·CB2·T
CB2·T
Scalers
Scalers

Figure 16.--Pressure curve for Čerenkov counter ČA.

T is the number of triggers.
n is the index of refraction.

The efficiency $\frac{\check{C}A1 \cdot T}{T}$ of the inner channel (squares) should be read off the right hand scale.

The efficiency $\frac{\check{C}A2 \cdot T}{T}$ of the outer channel (circles) should be read off the left hand scale.

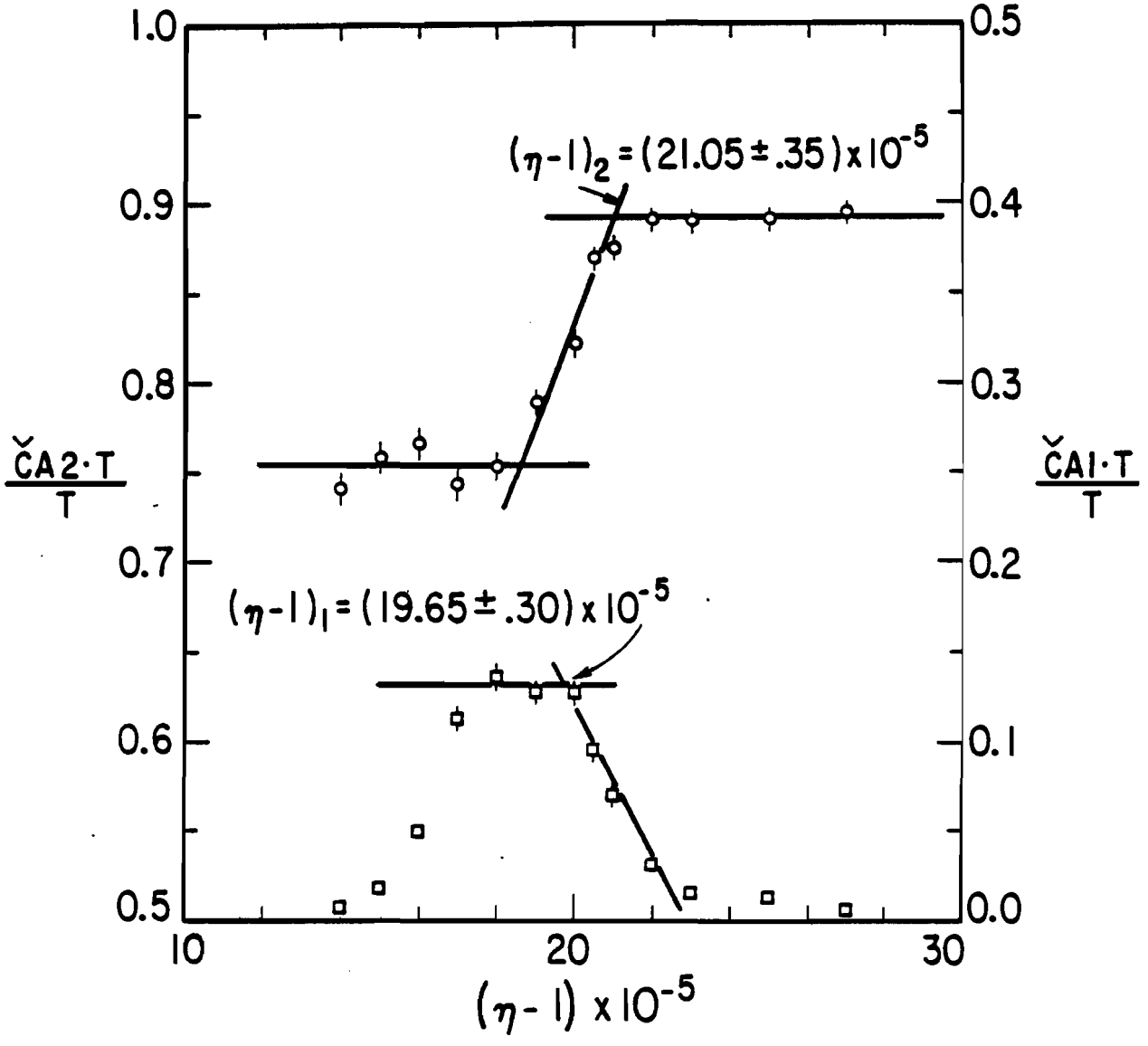
1.0
0.9
0.8
0.7
0.6
0.5
0.5
0.4
0.3
0.2
0.1
0.0
10
20
30
$(\eta-1)_2 = (21.05 \pm .35) \times 10^{-5}$
$(\eta-1)_1 = (19.65 \pm .30) \times 10^{-5}$
$\frac{\check{C}A2 \cdot T}{T}$
$\frac{\check{C}A1 \cdot T}{T}$
$(\eta-1) \times 10^{-5}$

Figure 17.--A diagram showing how the beam was pitched to the West. Dimensions and angles are not drawn to scale.

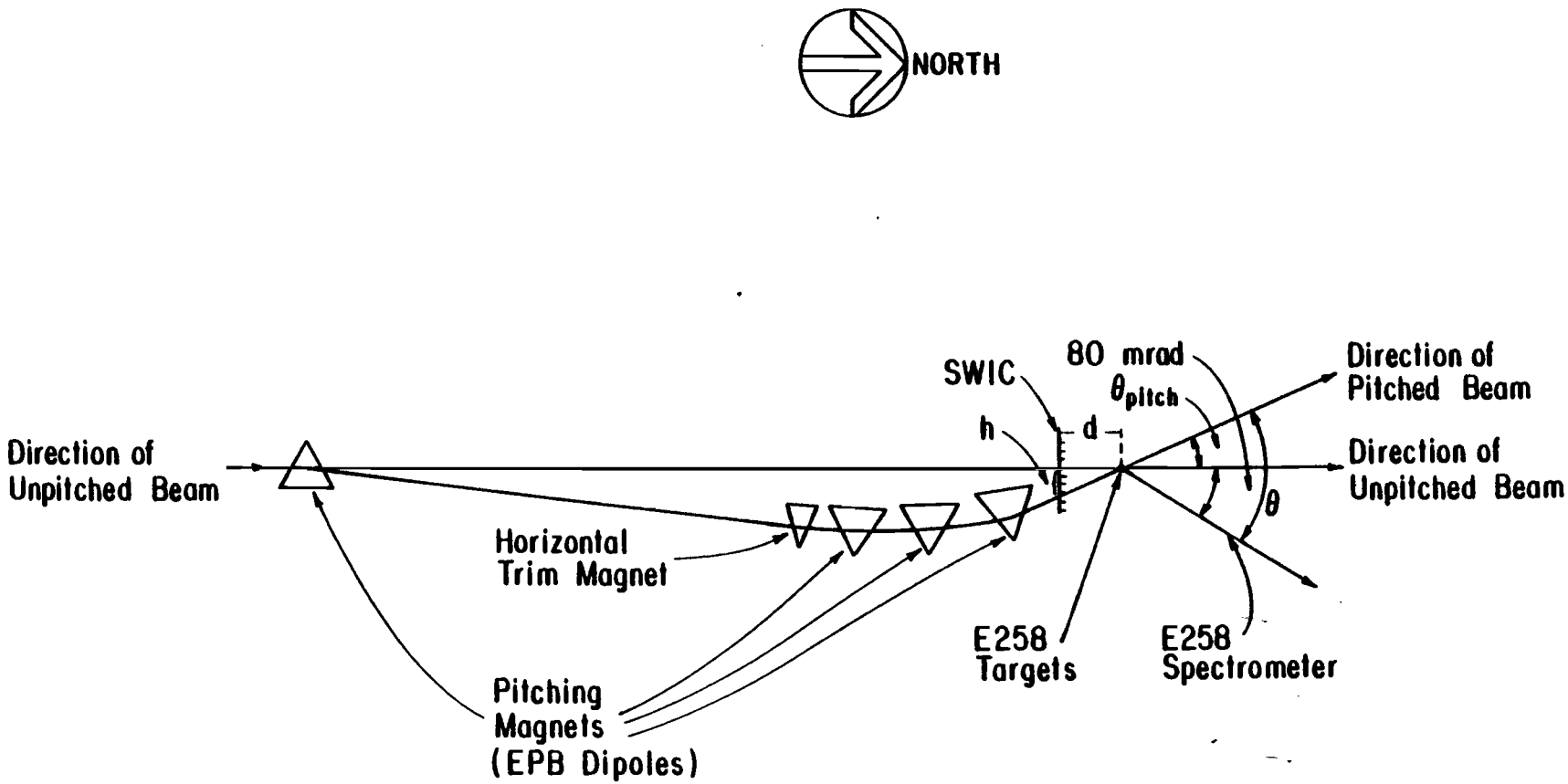
NORTH
Direction of Unpitched Beam
Horizontal Trim Magnet
Pitching Magnets (EPB Dipoles)
SWIC
h
d
80 mrad
θ_{pitch}
θ
E258 Targets
E258 Spectrometer
Direction of Pitched Beam
Direction of Unpitched Beam

Figure 18.--Distribution of the difference ΔX of the X-positions between all possible combinations of upstream and downstream X-tracks at the middle of the downstream dipole for a 20 GeV/c run.

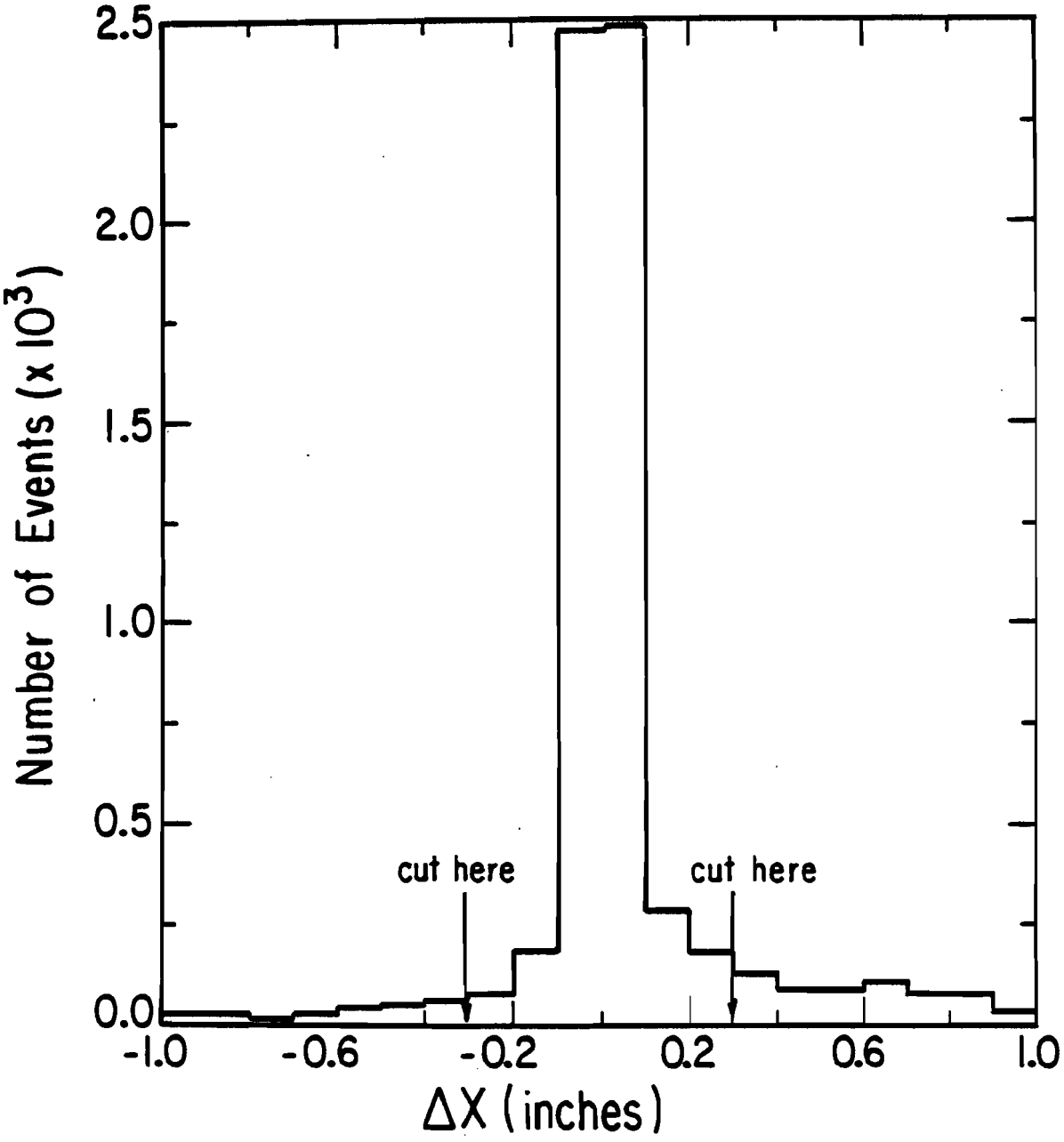
2.5
2.0
1.5
1.0
0.5
0.0
Number of Events (x 10^3)
cut here
cut here
-1.0
-0.6
-0.2
0.2
0.6
1.0
ΔX (inches)

Figure 19.--χ^2 distribution of the shower counter (ehμ) for a 25 GeV/c run.

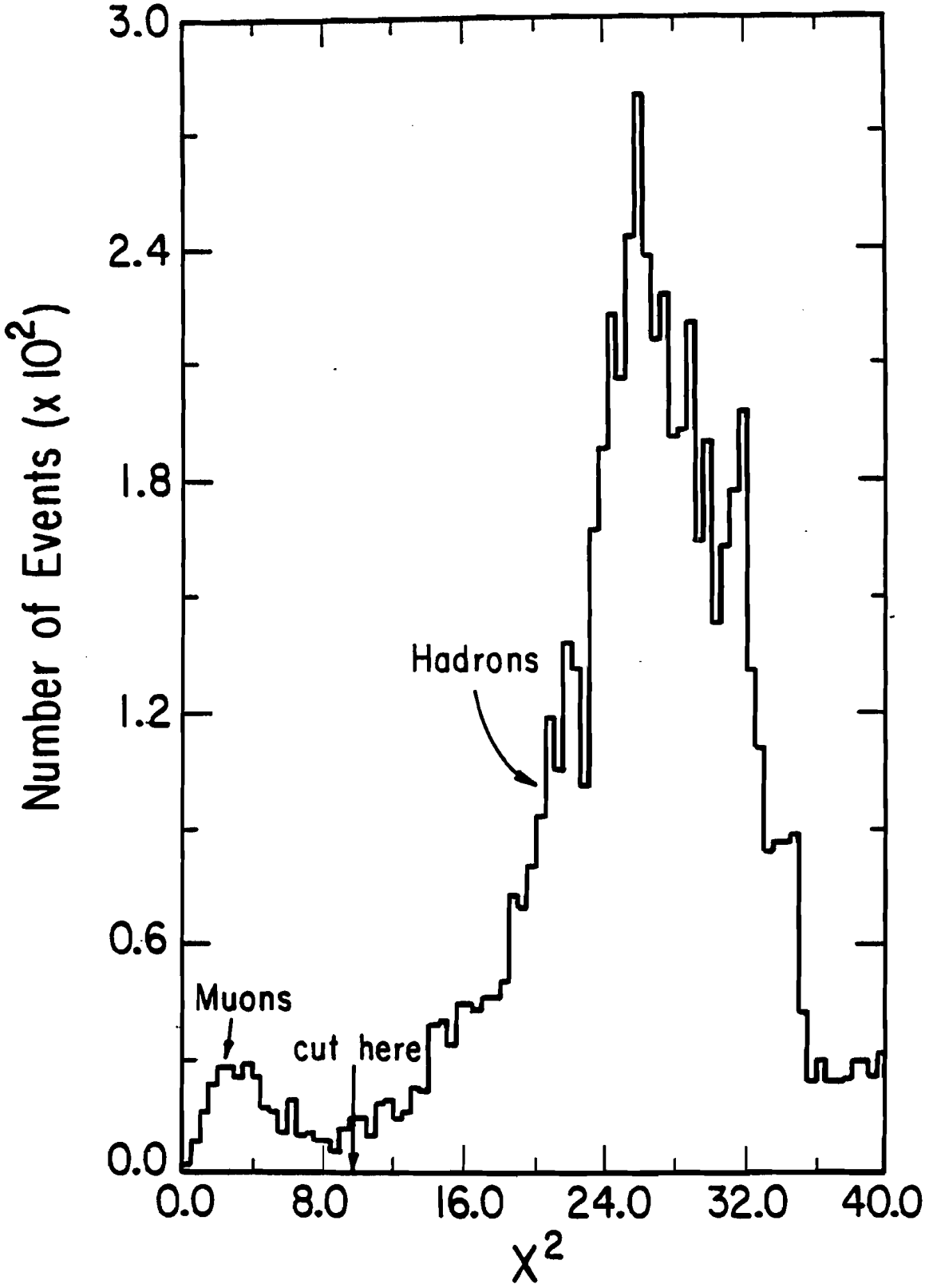
3.0
2.4
1.8
1.2
0.6
0.0
Number of Events (x 10²)
Hadrons
Muons
cut here
0.0
8.0
16.0
24.0
32.0
40.0
X²

Figure 20.--χ^2/DOF distributions in the horizontal and vertical planes for tracks with the best fit for a 25 GeV/c run. No DST cuts were applied to the data. The χ^2 cuts are shown.

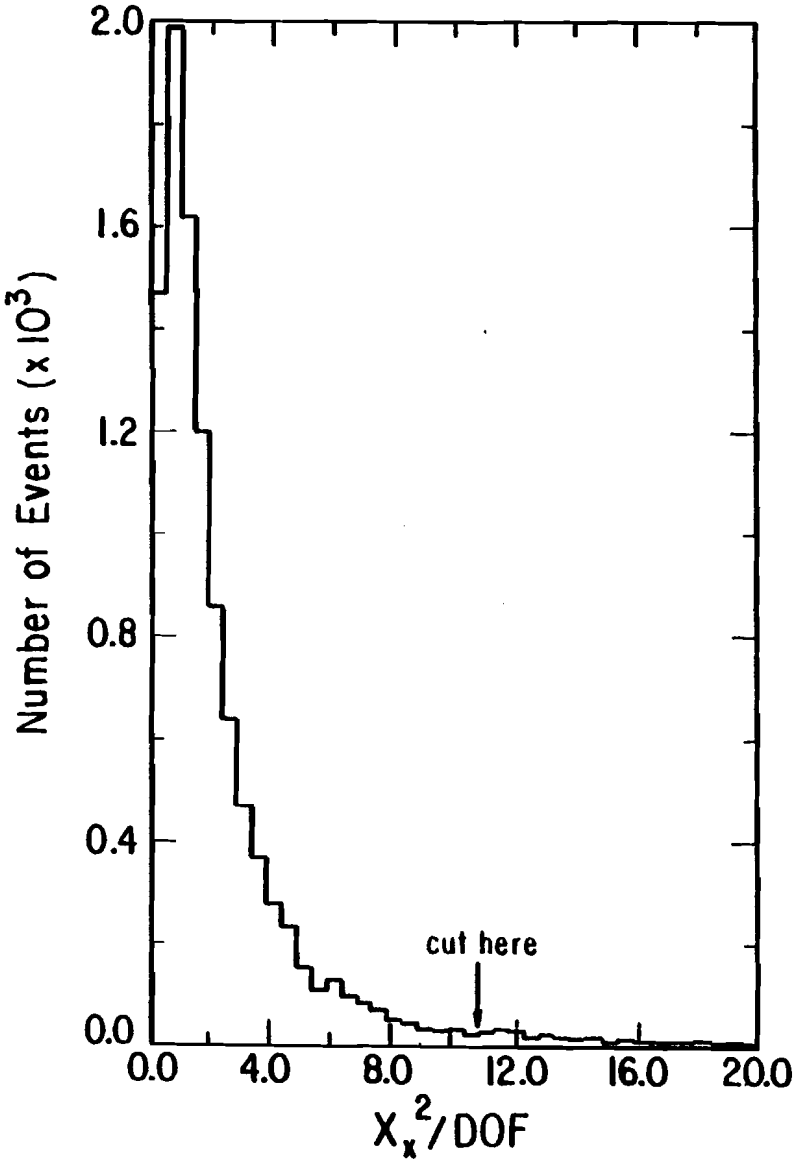
2.0
1.6
1.2
0.8
0.4
0.0
Number of Events (x 10^3)
cut here
0.0
4.0
8.0
12.0
16.0
20.0
X_x^2/DOF

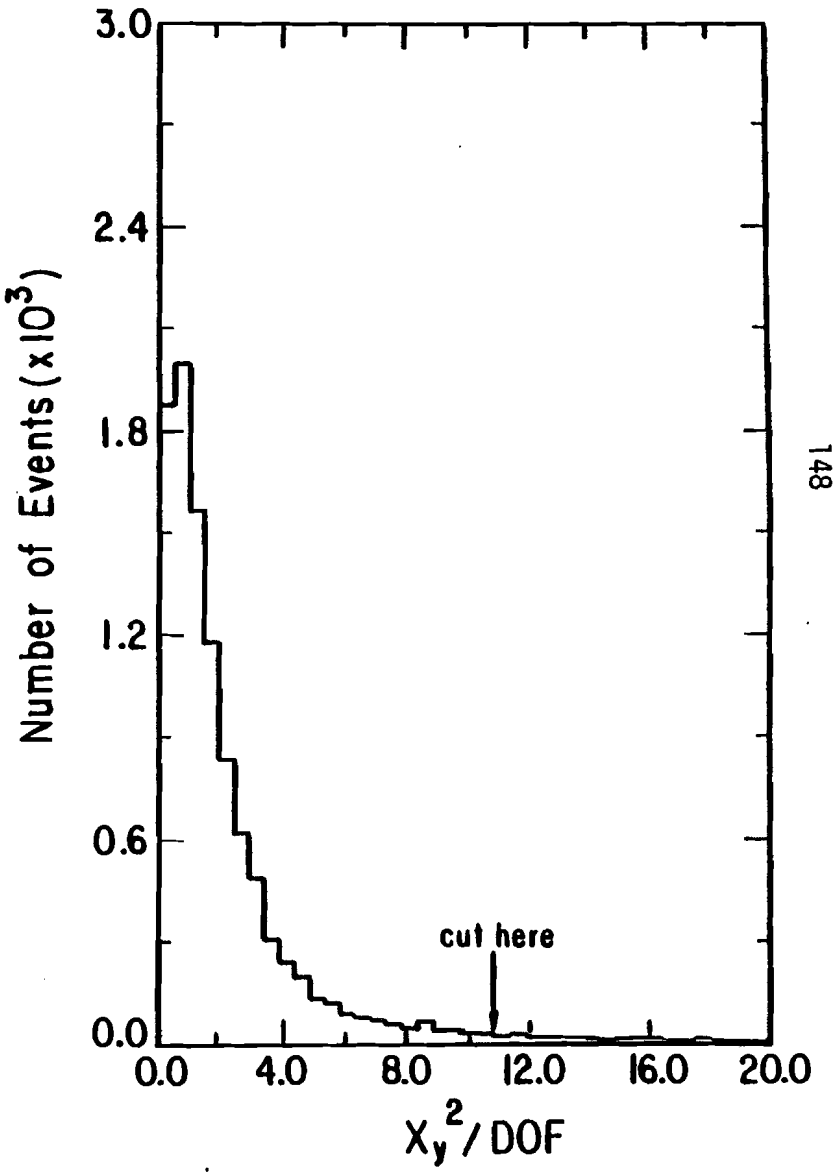
3.0
2.4
1.8
1.2
0.6
0.0
Number of Events (x 10^3)
cut here
0.0
4.0
8.0
12.0
16.0
20.0
X_y^2/DOF

Figure 21.--$\Delta P/P_0$ distribution for a 25 GeV/c run. All but the $\Delta P/P_0$ and target cuts were applied to the data. The $\Delta P/P_0$ cut is shown.

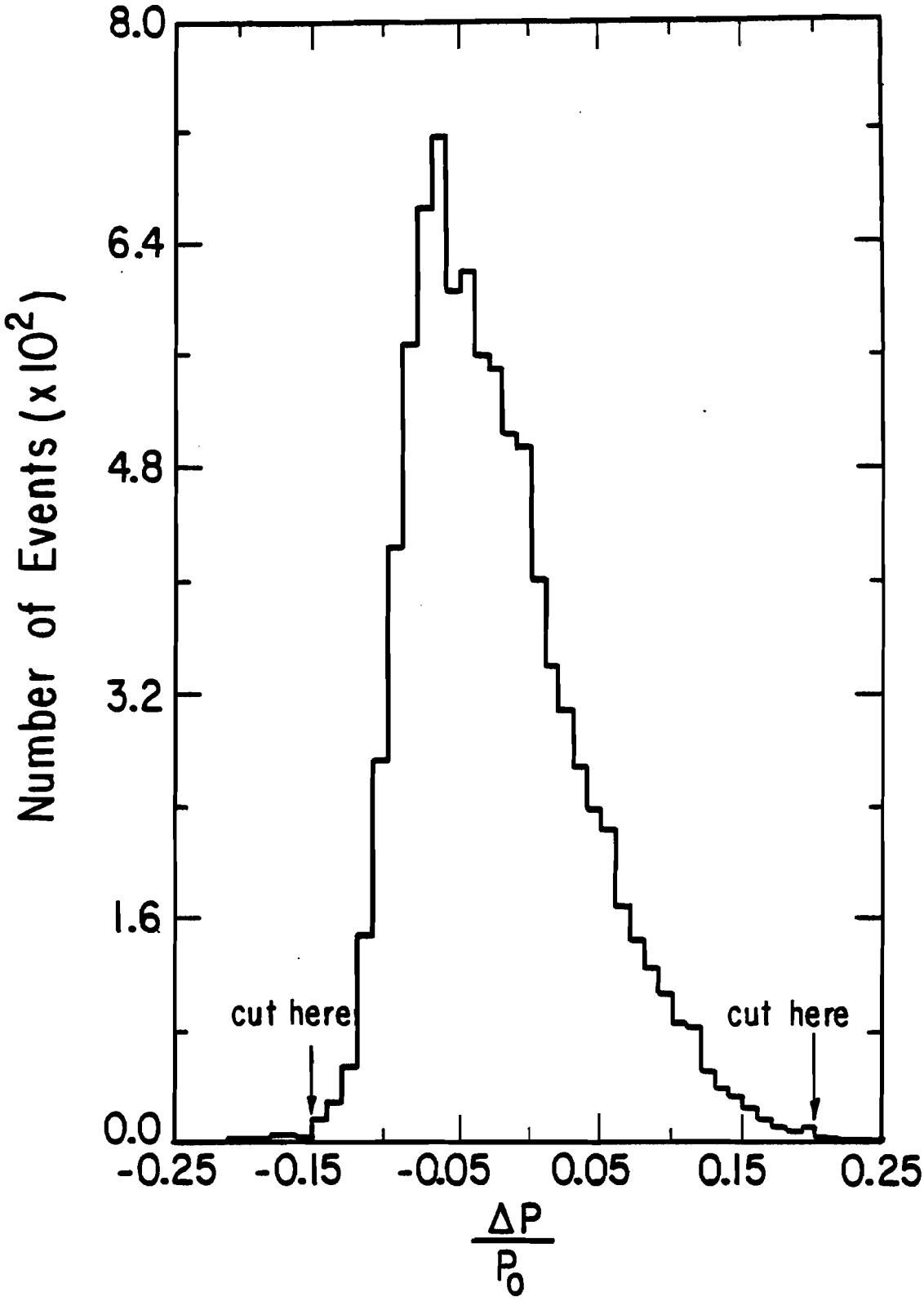
8.0
6.4
4.8
3.2
1.6
0.0
Number of Events (x 10²)
cut here
cut here
-0.25
-0.15
-0.05
0.05
0.15
0.25
ΔP / P₀

Figure 22.--Horizontal versus vertical positions of tracks at the experimental target for 25 GeV/c runs with the hydrogen and tungsten targets. All but the target cuts were applied to the data. The hydrogen and nuclear target cuts on the verteces are shown.

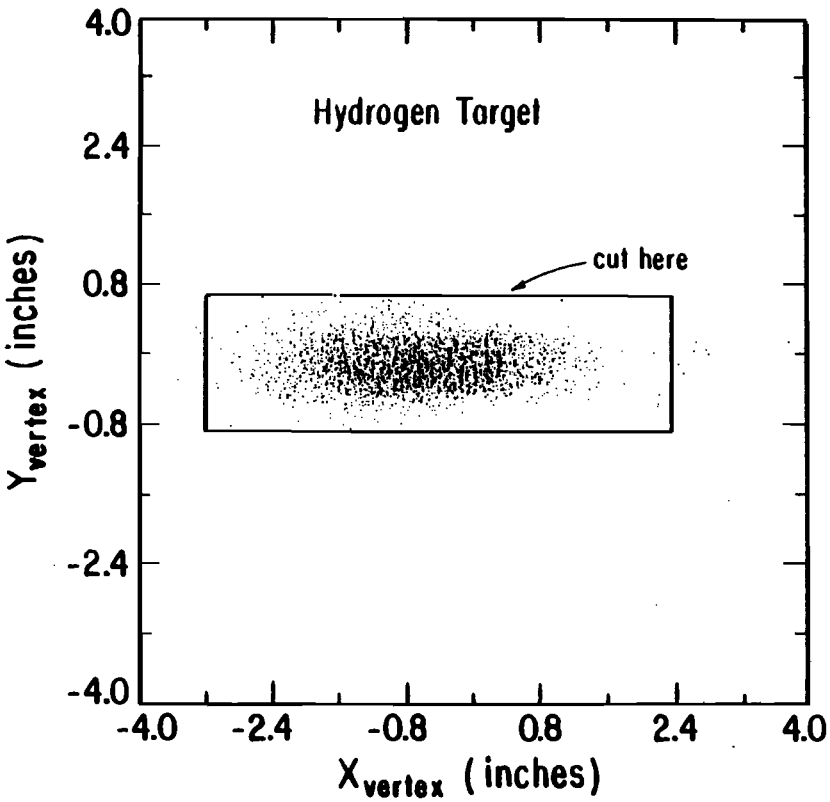
Hydrogen Target
cut here
4.0
2.4
0.8
-0.8
-2.4
-4.0
-4.0
-2.4
-0.8
0.8
2.4
4.0
Y_{vertex} (inches)
X_{vertex} (inches)

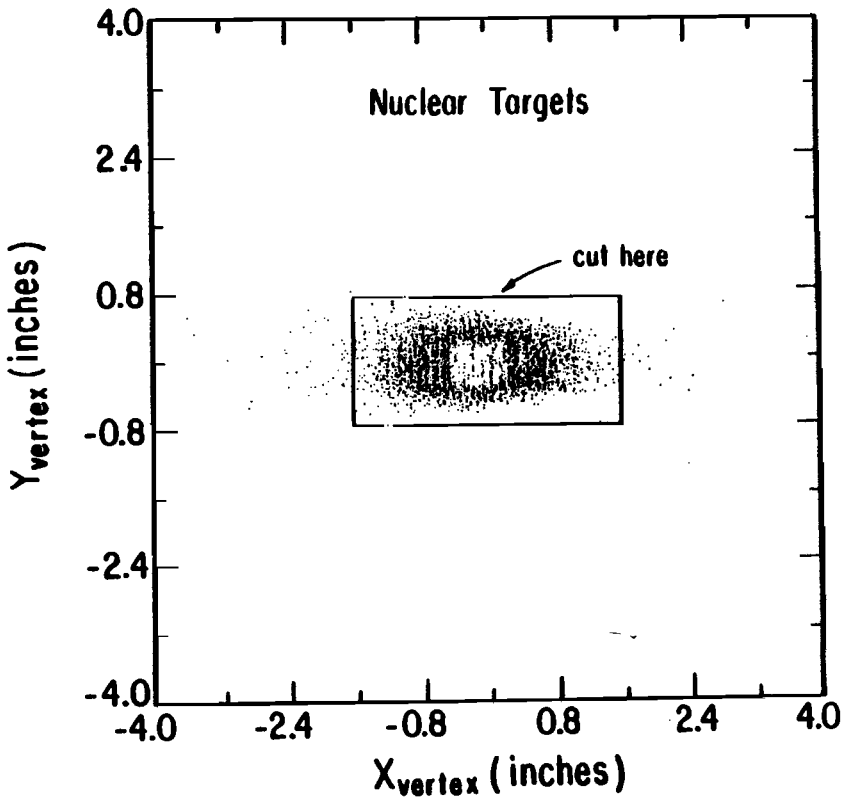
Nuclear Targets
cut here
4.0
2.4
0.8
-0.8
-2.4
-4.0
-4.0
-2.4
-0.8
0.8
2.4
4.0
Y_{vertex} (inches)
X_{vertex} (inches)

Figure 23.--(Number of Reconstructed Events/Number of Strobes) ratio versus the spectrometer momentum for randomly chosen runs with 200 GeV π^- beam (pitched to the West) incident on the tungsten target. No DST cuts were applied to the reconstructed events.

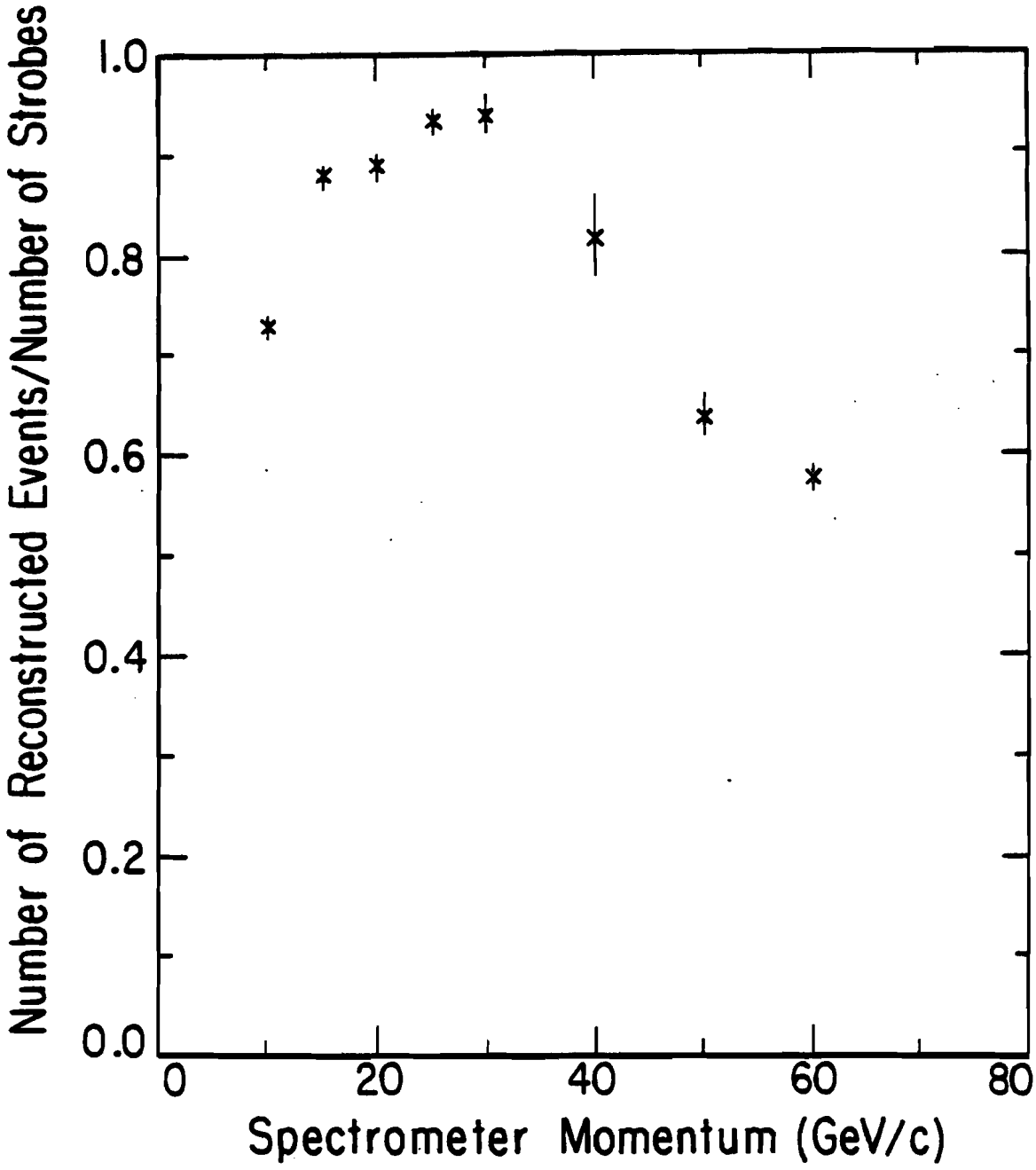
Number of Reconstructed Events/Number of Strobes
1.0
0.8
0.6
0.4
0.2
0.0
0
20
40
60
80
Spectrometer Momentum (GeV/c)

Figure 24.--Horizontal and vertical profiles of the 200 π^- beam, pitched to the West, at the position of SC710. Each SC710 wire corresponds to 3 mm.

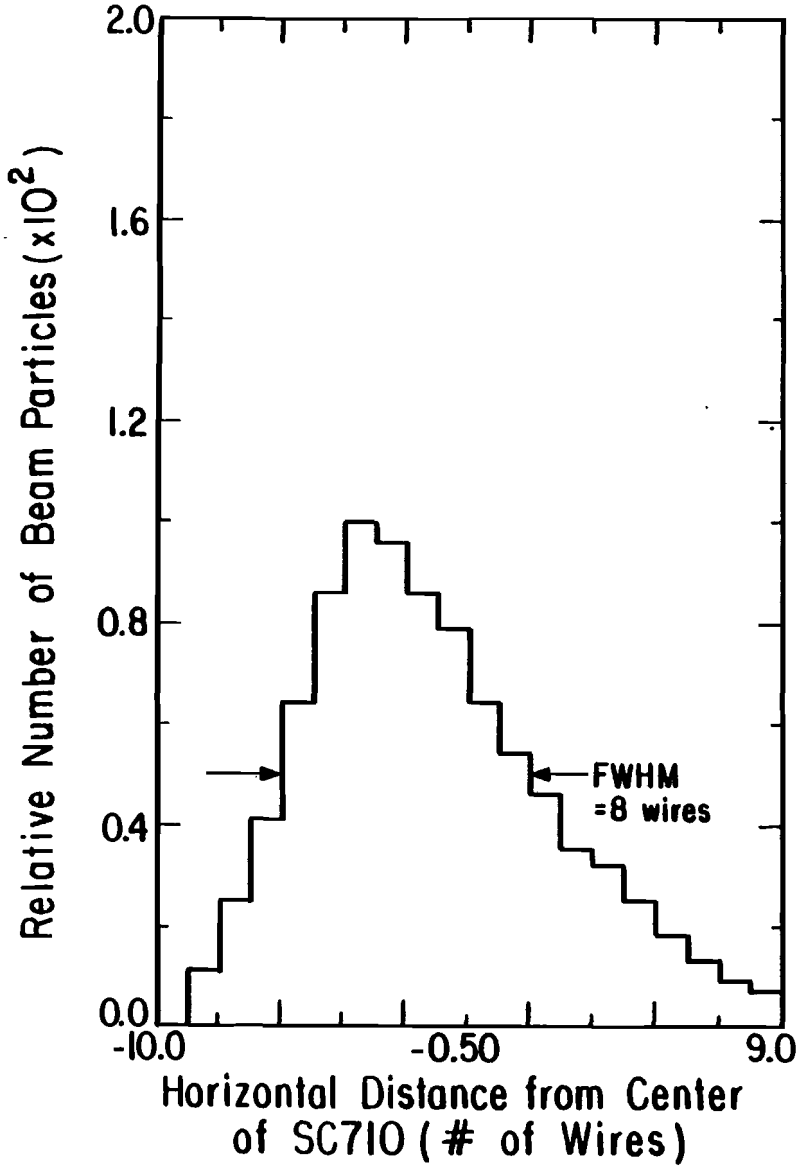
2.0
1.6
1.2
0.8
0.4
0.0
Relative Number of Beam Particles (x10²)
FWHM
=8 wires
-10.0
-0.50
9.0
Horizontal Distance from Center
of SC710 (# of Wires)

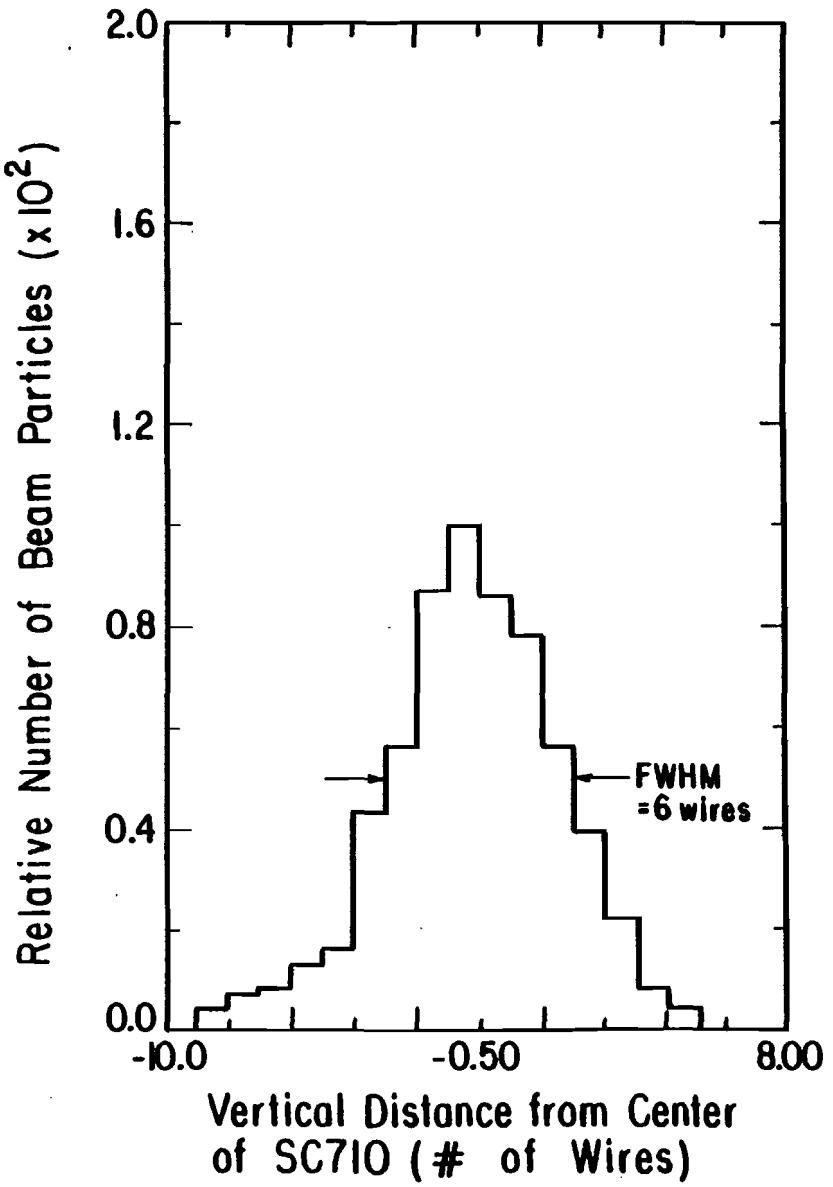
2.0
1.6
1.2
0.8
0.4
0.0
Relative Number of Beam Particles (x10²)
FWHM
=6 wires
-10.0
-0.50
8.00
Vertical Distance from Center
of SC710 (# of Wires)

Figure 25.--Monte Carlo acceptances for each momentum bin versus momentum for spectrometer settings of 25, 27.5 and 30 GeV.

x: For a spectrometer setting of 25.0 GeV/c.
o: For a spectrometer setting of 27.5 GeV/c.
□: For a spectrometer setting of 30.0 GeV/c.

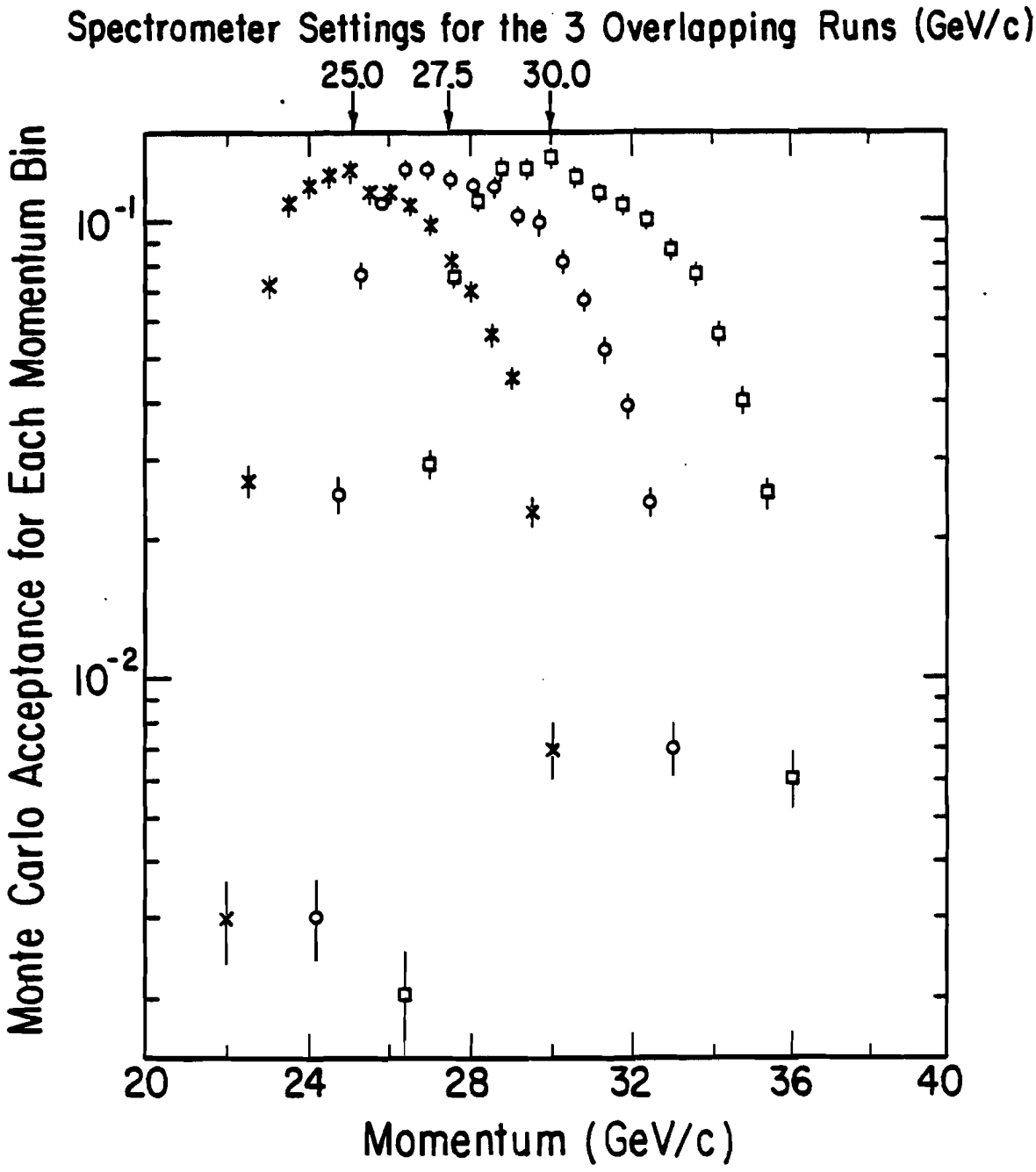
Spectrometer Settings for the 3 Overlapping Runs (GeV/c)
25.0
27.5
30.0
Monte Carlo Acceptance for Each Momentum Bin
10^{-1}
10^{-2}
20
24
28
32
36
40
Momentum (GeV/c)

Figure 26.--The invariant cross section (arbitrary units) versus momentum bin for the three overlapping runs. The errors are statistical only.

x: For a spectrometer setting of 25.0 GeV/c.
o: For a spectrometer setting of 27.5 GeV/c.
□: For a spectrometer setting of 30.0 GeV/c.

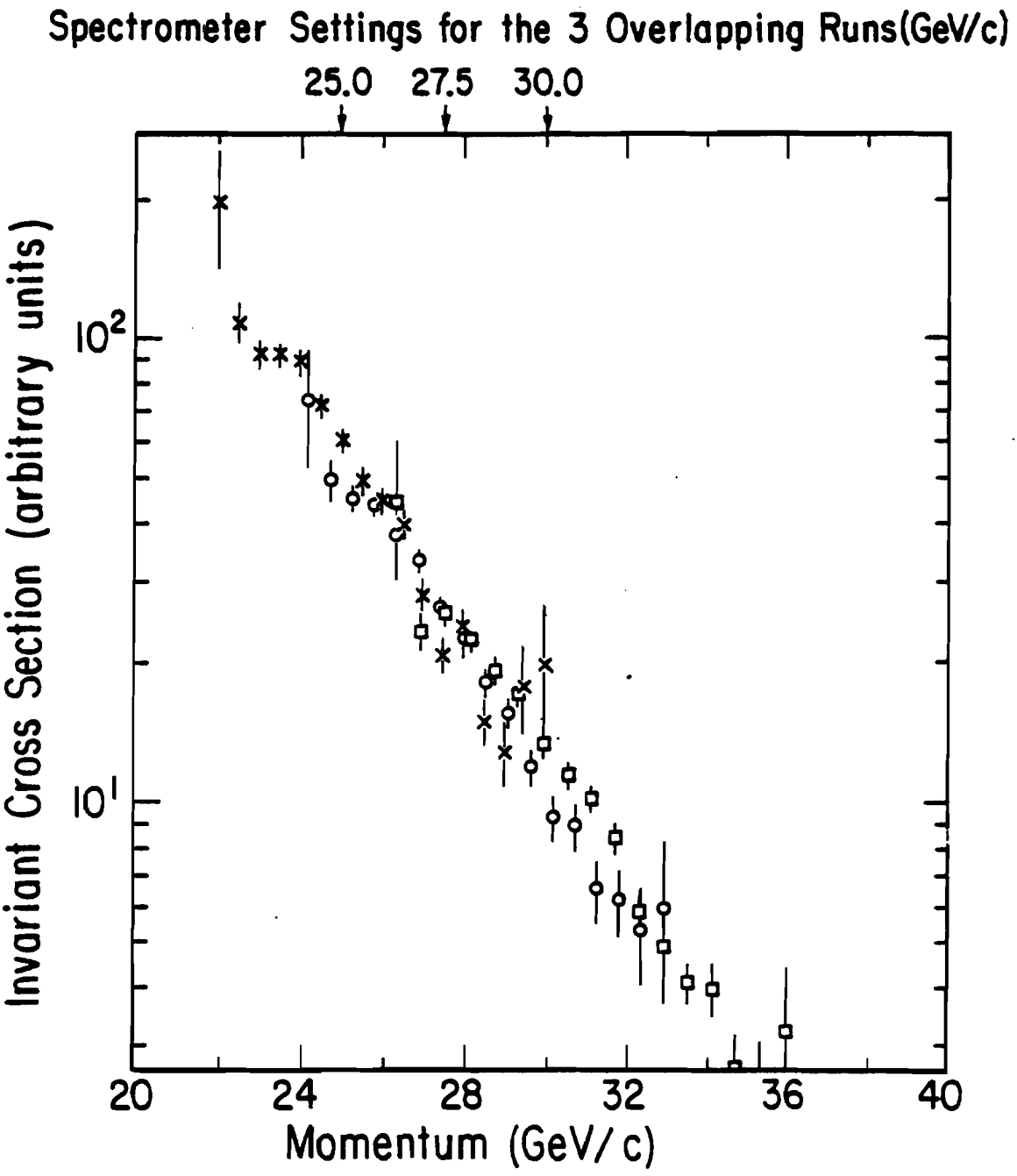
Spectrometer Settings for the 3 Overlapping Runs(GeV/c)
25.0
27.5
30.0
Invariant Cross Section (arbitrary units)
10^2
10^1
20
24
28
32
36
40
Momentum (GeV/c)

Figure 27.--Spectrometer acceptances versus the horizontal and vertical reconstructed angles of the particles at the target. The target was hydrogen and the spectrometer setting was 30 GeV/c.

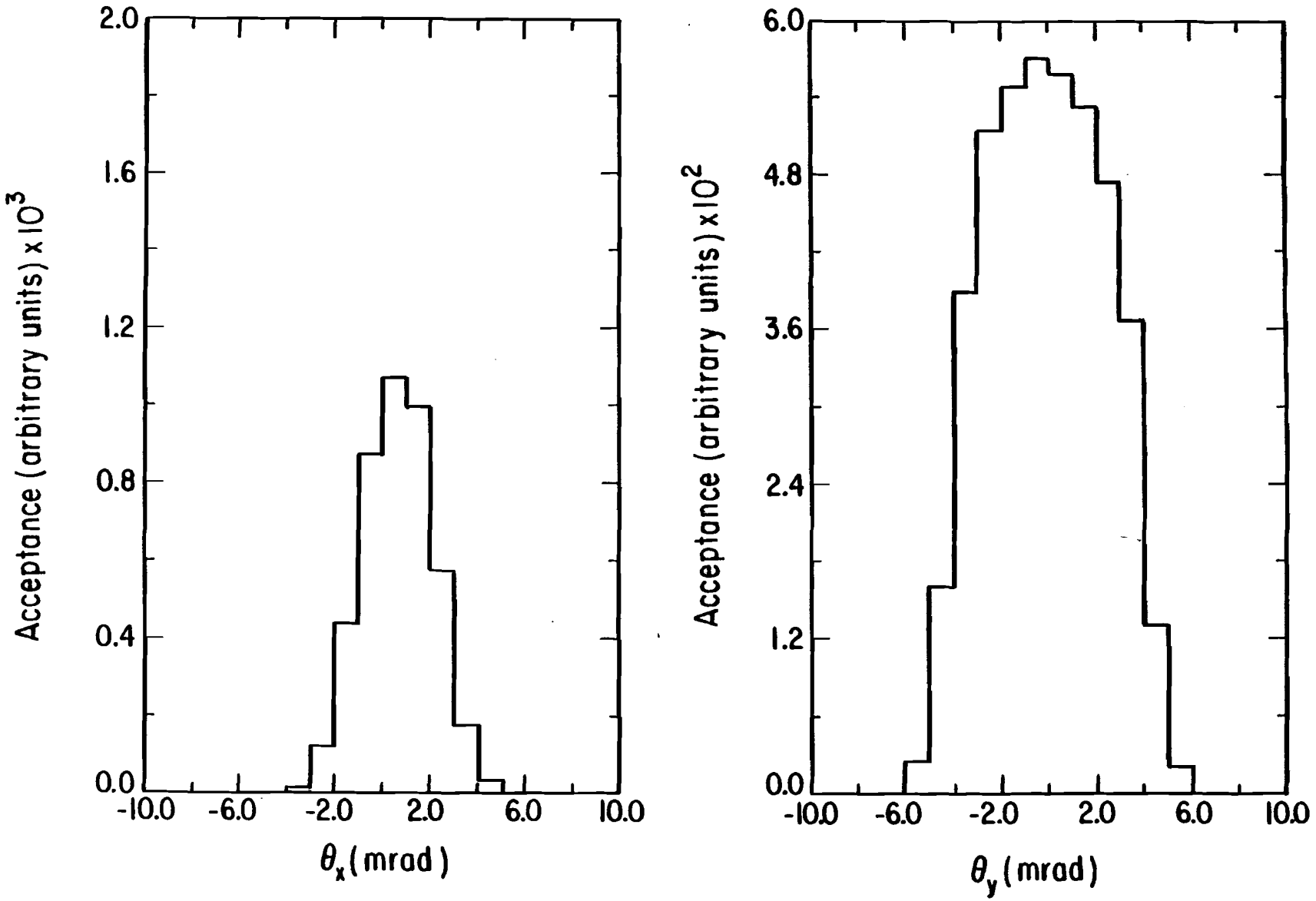
Acceptance (arbitrary units) x 10^3
2.0
1.6
1.2
0.8
0.4
0.0
-10.0
-6.0
-2.0
2.0
6.0
10.0
θx (mrad)
Acceptance (arbitrary units) x 10^2
6.0
4.8
3.6
2.4
1.2
0.0
-10.0
-6.0
-2.0
2.0
6.0
10.0
θy (mrad)

Figure 28.--Comparison of Monte Carlo and data distributions. From left to right they are:

reconstructed horizontal position at the experimental target
reconstructed horizontal position at D7
$\Delta P/P_o$ for 2% bins.

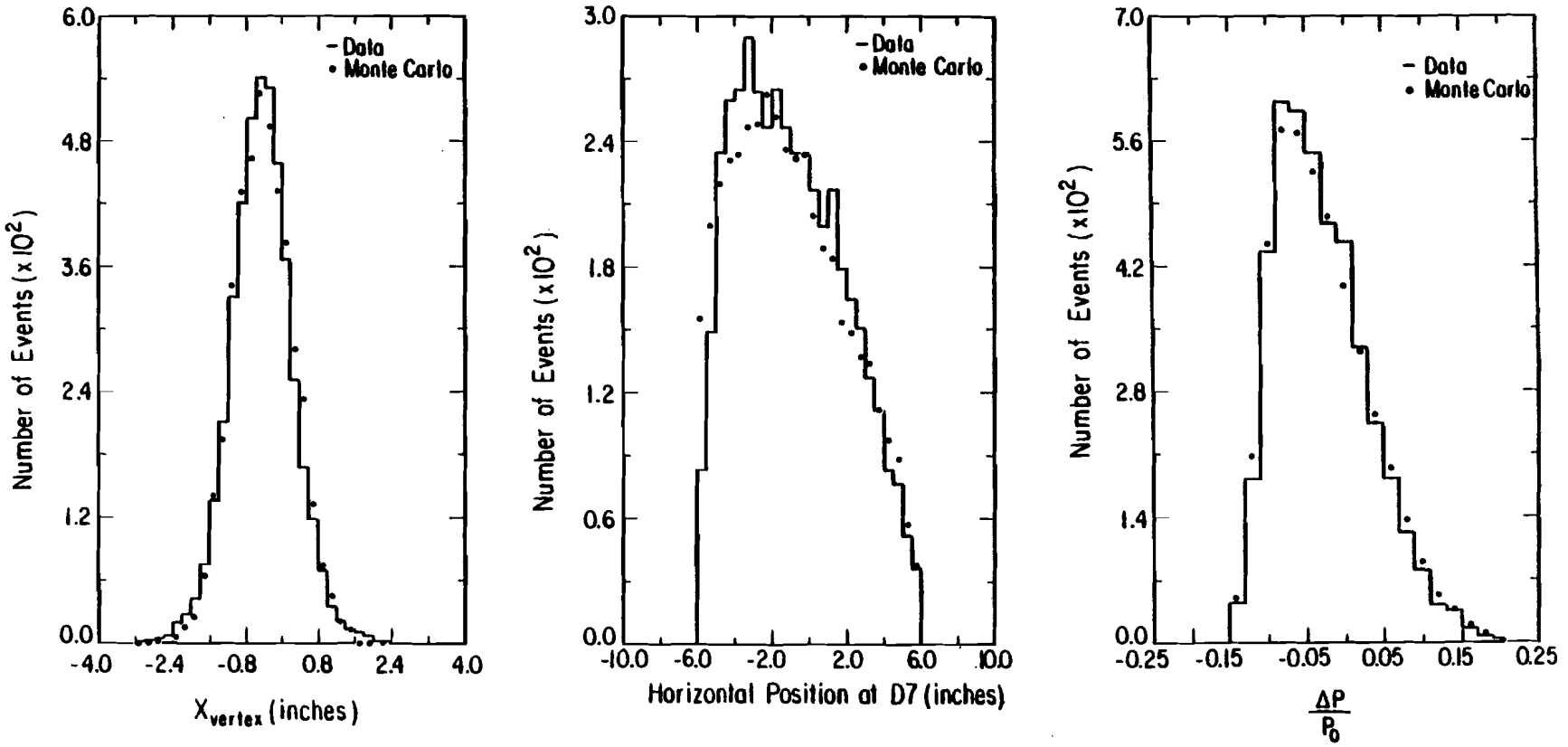
Number of Events (x10²)
6.0
4.8
3.6
2.4
1.2
0.0
-4.0
-2.4
-0.8
0.8
2.4
4.0
X vertex (inches)
– Data
• Monte Carlo
3.0
2.4
1.8
1.2
0.6
0.0
-10.0
-6.0
-2.0
2.0
6.0
10.0
Horizontal Position at D7 (inches)
7.0
5.6
4.2
2.8
1.4
0.0
-0.25
-0.15
-0.05
0.05
0.15
0.25
ΔP/P₀

Figure 29.--Integrated acceptance versus momentum for the nuclear targets and for the 200 GeV π^-, 97 mrad running period.

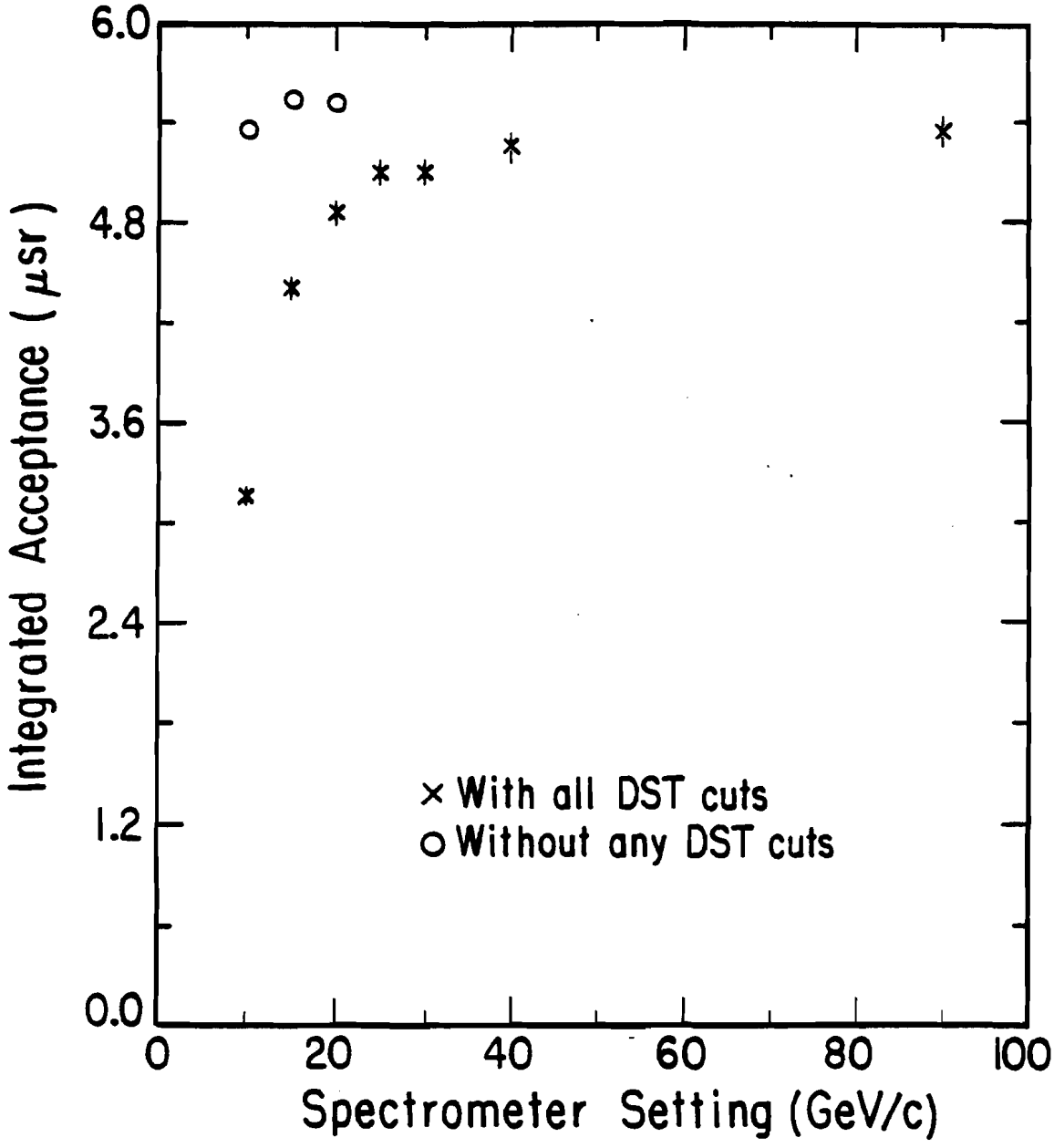
6.0
4.8
3.6
2.4
1.2
0.0
Integrated Acceptance (μsr)
0
20
40
60
80
100
Spectrometer Setting (GeV/c)
× With all DST cuts
o Without any DST cuts

Figure 30.--The momentum resolution of the spectrometer versus the momentum as found by the Monte Carlo program.

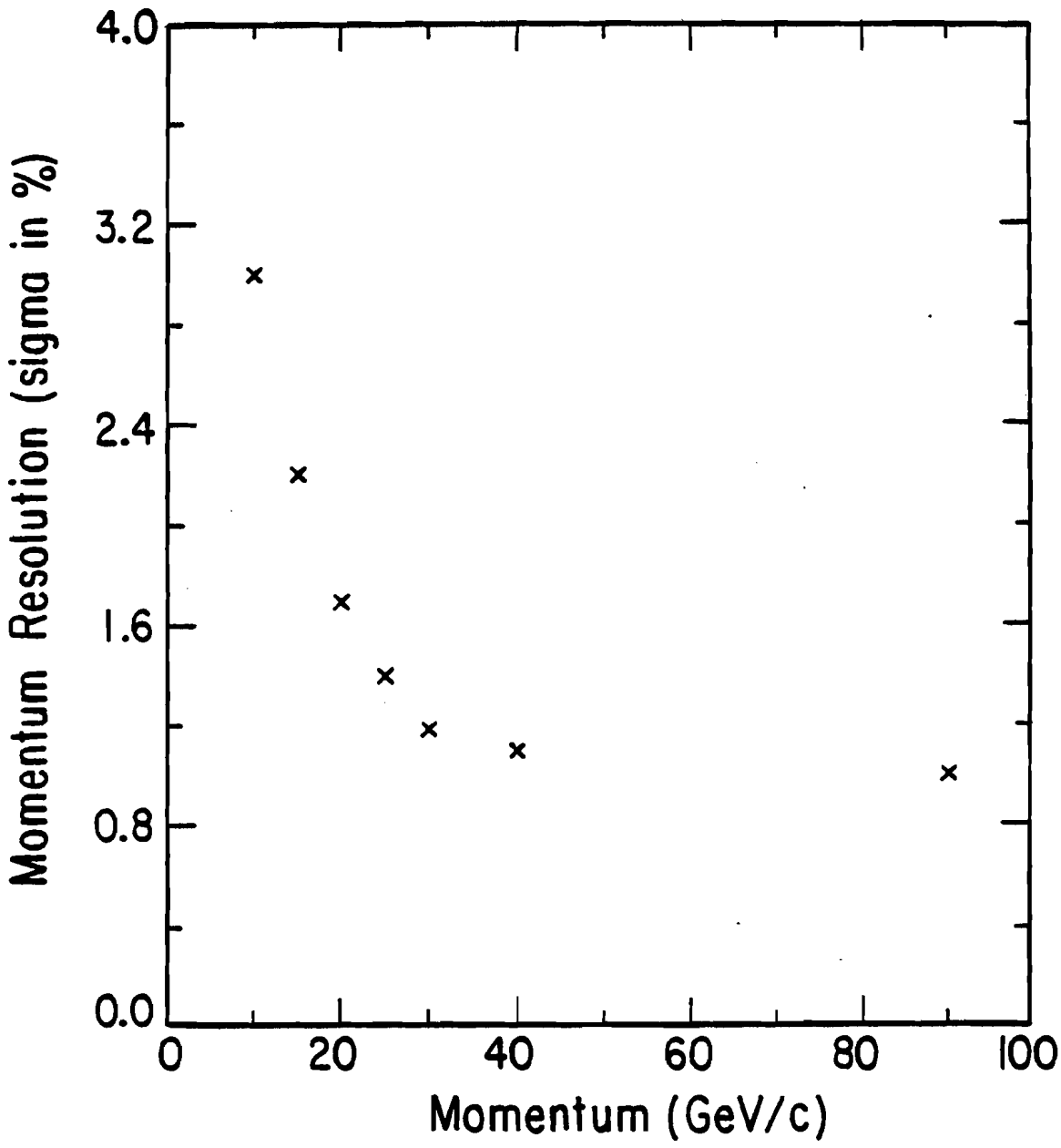
4.0
3.2
2.4
1.6
0.8
0.0
Momentum Resolution (sigma in %)
0
20
40
60
80
100
Momentum (GeV/c)

Figure 31.--Zero iteration invariant cross section for the reaction $\pi^- + Be \rightarrow \pi^- + X$ with 200 GeV beam. The errors are statistical only. The straight line is a fit by eye to the first three points.

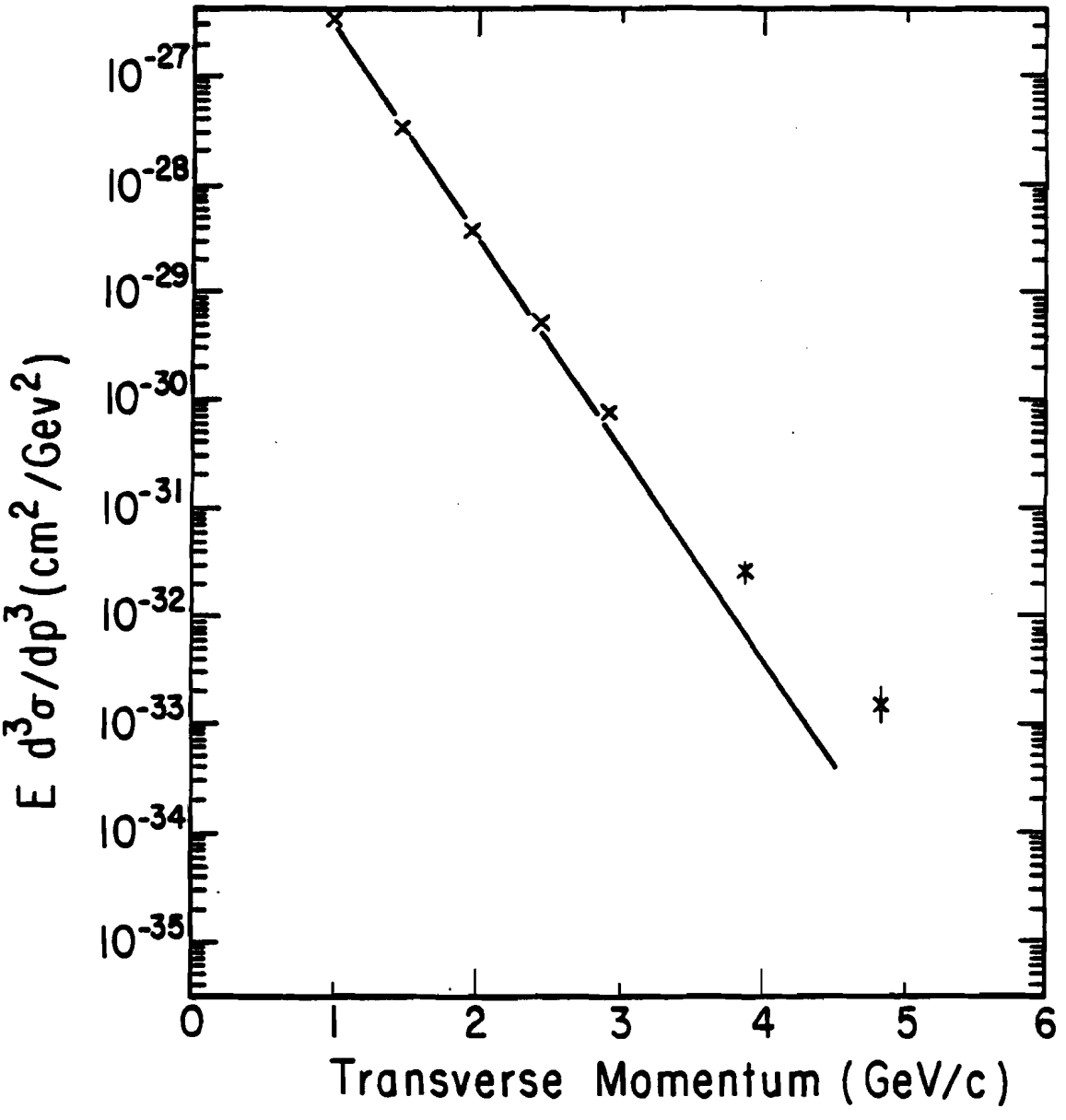
10^{-27}
10^{-28}
10^{-29}
10^{-30}
10^{-31}
10^{-32}
10^{-33}
10^{-34}
10^{-35}
$E\ d^3\sigma/dp^3 (cm^2/Gev^2)$
0
1
2
3
4
5
6
Transverse Momentum (GeV/c)

Figure 32.--Measured and fitted local slopes of the invariant cross section for π^- production versus $P_\perp$. The line drawn through the fitted points is only to guide the eye.

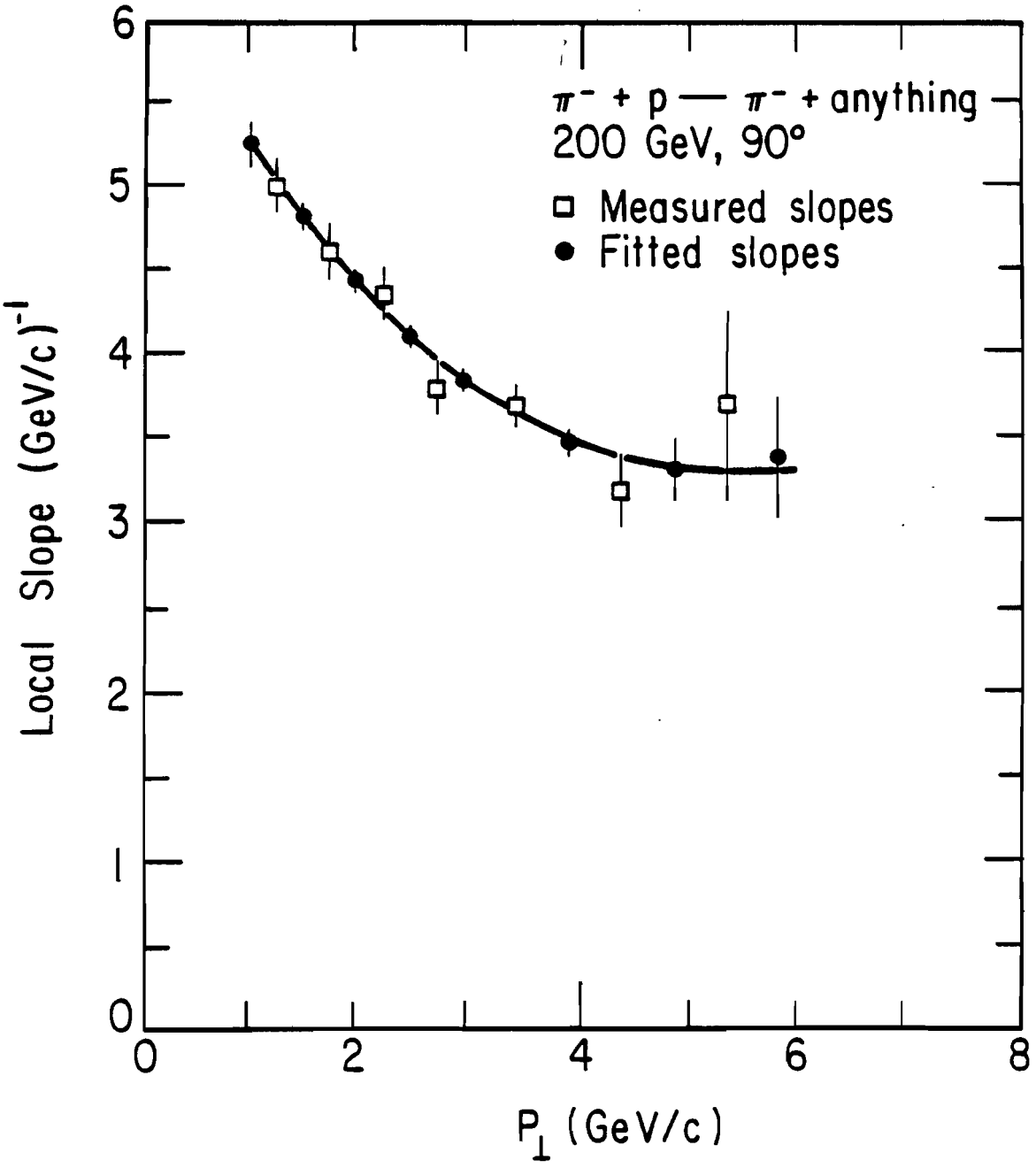
$\pi^- + p \rightarrow \pi^- +$ anything
200 GeV, 90°
Measured slopes
Fitted slopes
Local Slope $(GeV/c)^{-1}$
$P_\perp$ (GeV/c)
0
1
2
3
4
5
6
0
2
4
6
8

Figure 33.--$\pi^- p \rightarrow \pi^+, \pi^-$ + anything invariant cross sections versus $P_\perp$ for the three CM angles. The line is to guide the eye through the 90° data points.

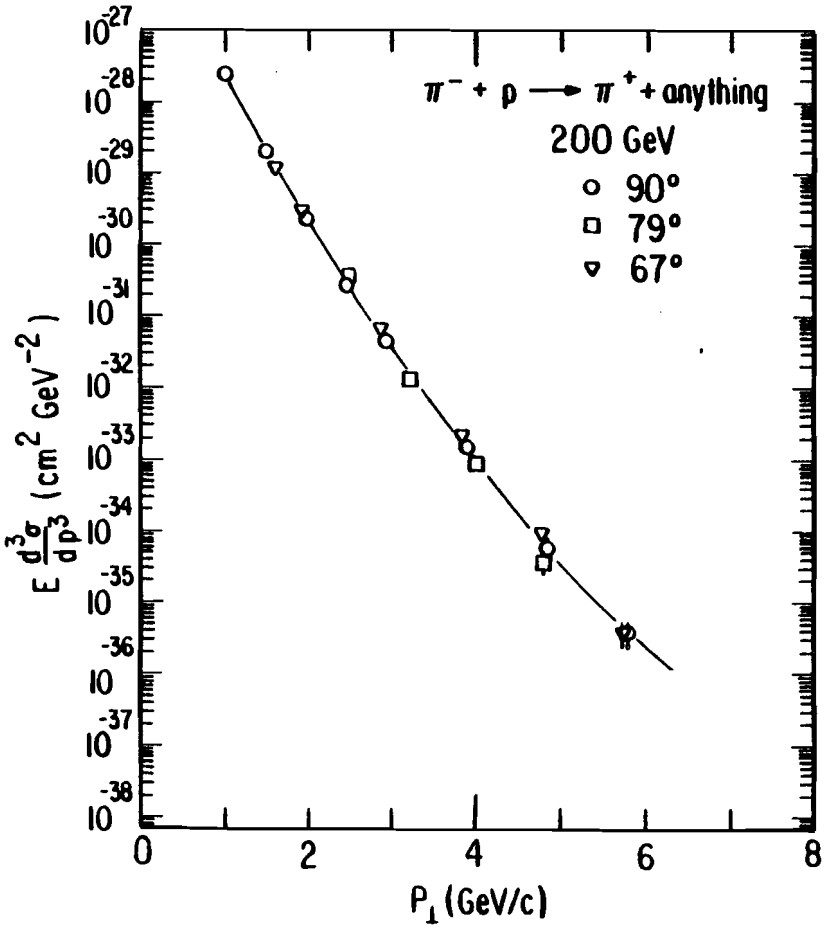
$\pi^- + p \rightarrow \pi^+ +$ anything
200 GeV
○ 90°
□ 79°
▽ 67°
$E\frac{d^3\sigma}{dp^3}$ (cm^2 GeV^{-2})
$P_\perp$ (GeV/c)

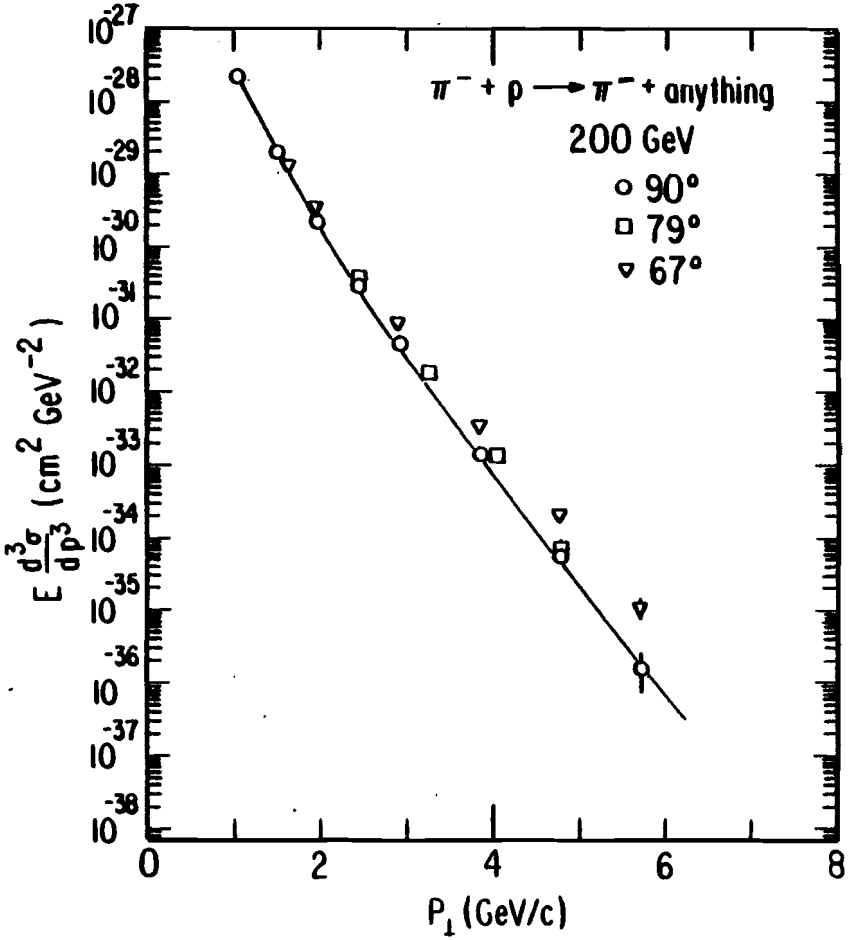
$\pi^- + p \rightarrow \pi^- +$ anything
200 GeV
○ 90°
□ 79°
▽ 67°
$E\frac{d^3\sigma}{dp^3}$ (cm^2 GeV^{-2})
$P_\perp$ (GeV/c)

Figure 34.--$\pi^- p \rightarrow K^+, K^-$ + anything invariant cross sections versus $P_\perp$ for the three CM angles. The line is to guide the eye through the 90° data points.

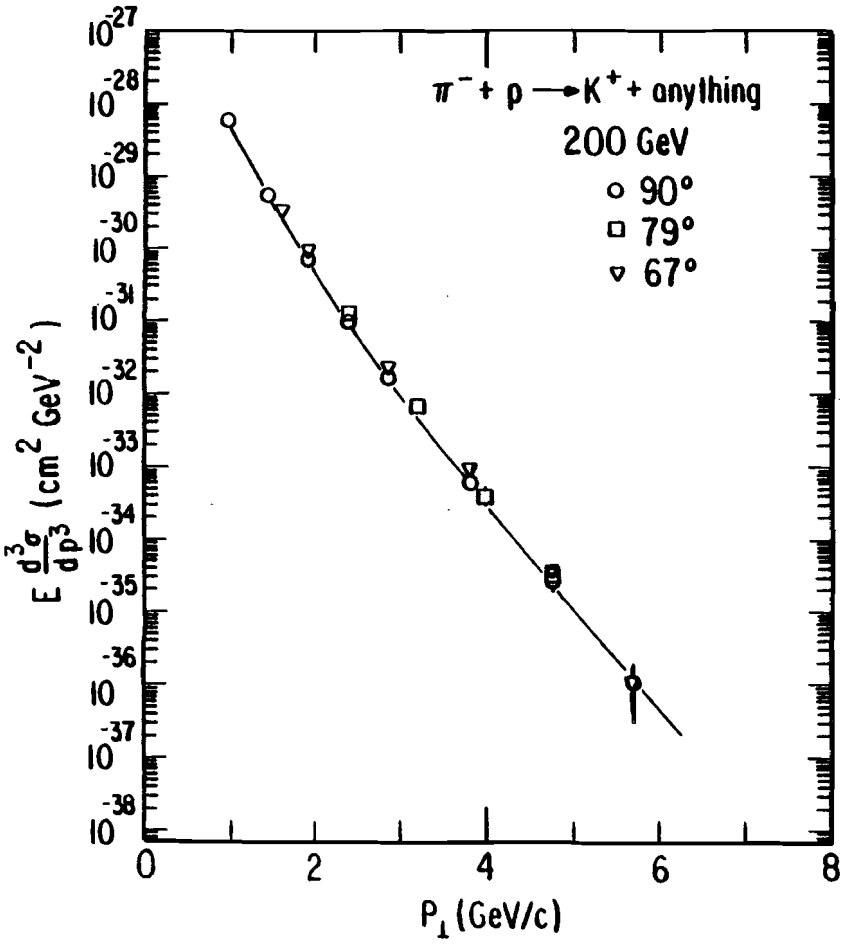
$\pi^- + p \rightarrow K^+ +$ anything
200 GeV
○ 90°
□ 79°
▽ 67°
$E\frac{d^3\sigma}{dp^3}$ (cm^2 GeV^{-2})
$P_\perp$ (GeV/c)

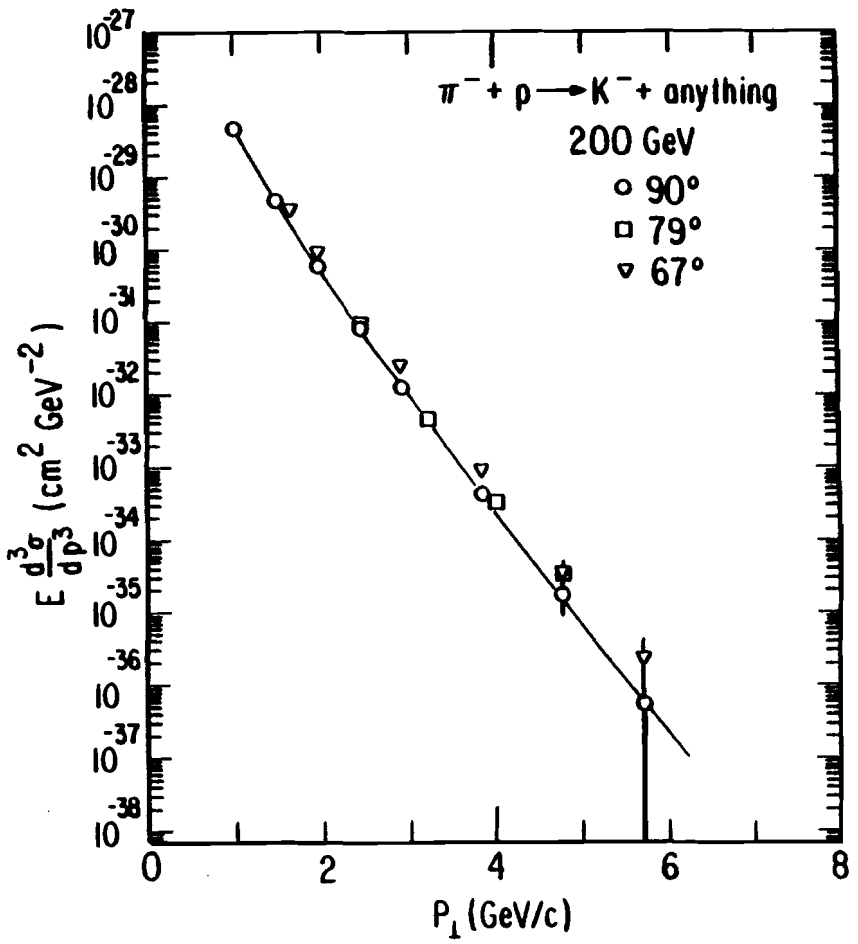
$\pi^- + p \rightarrow K^- +$ anything
200 GeV
○ 90°
□ 79°
▽ 67°
$E\frac{d^3\sigma}{dp^3}$ (cm^2 GeV^{-2})
$P_\perp$ (GeV/c)

Figure 35.--$\pi^- p \rightarrow p, \bar{p}$ + anything invariant cross sections versus $P_\perp$ for the three CM angles. The line is to guide the eye through the 90° data points.

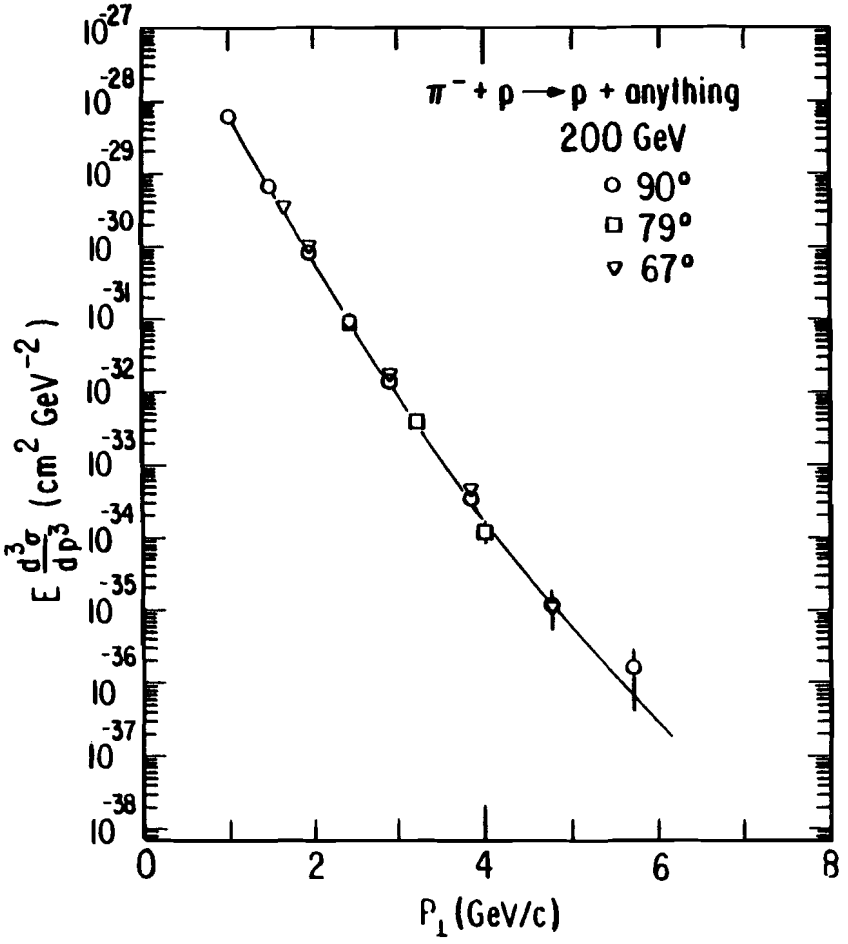
$\pi^- + p \rightarrow p$ + anything
200 GeV
○ 90°
□ 79°
▽ 67°
$E \frac{d^3\sigma}{dp^3}$ (cm^2 GeV^{-2})
$P_\perp$ (GeV/c)

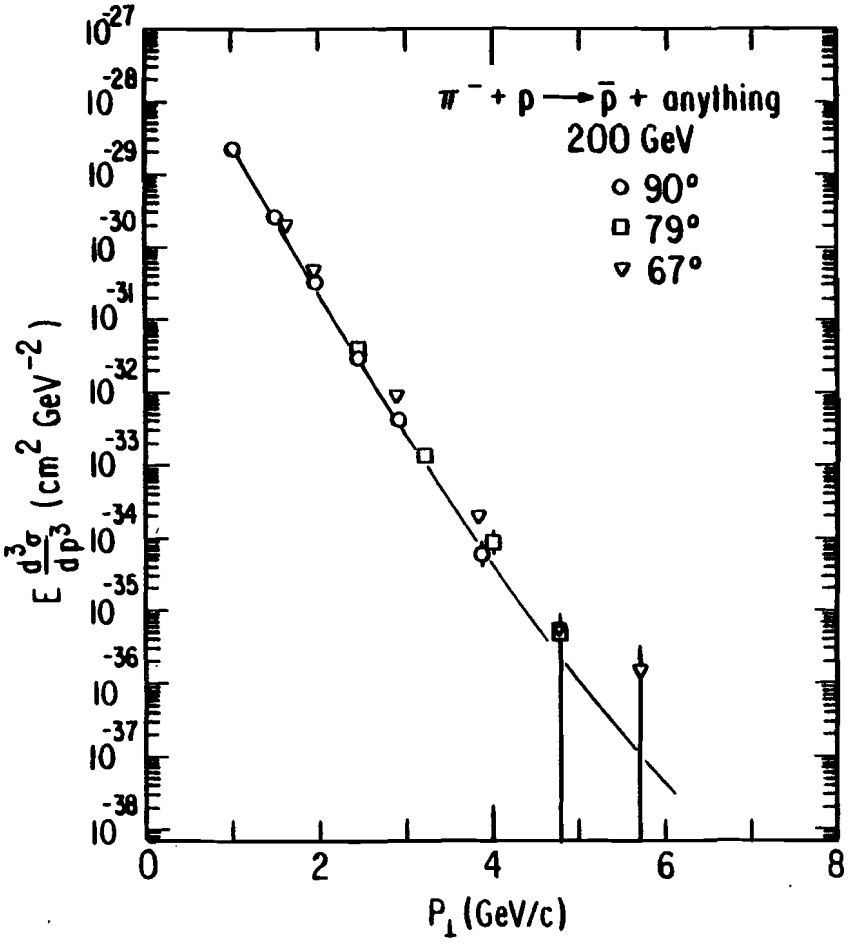
$\pi^- + p \rightarrow \bar{p}$ + anything
200 GeV
○ 90°
□ 79°
▽ 67°
$E \frac{d^3\sigma}{dp^3}$ (cm^2 GeV^{-2})
$P_\perp$ (GeV/c)

Figure 36.--Comparison of the $\pi^- + p \rightarrow \pi^+, \pi^-$ + anything invariant cross sections versus $P_\perp$ with the predictions of the FFF model.

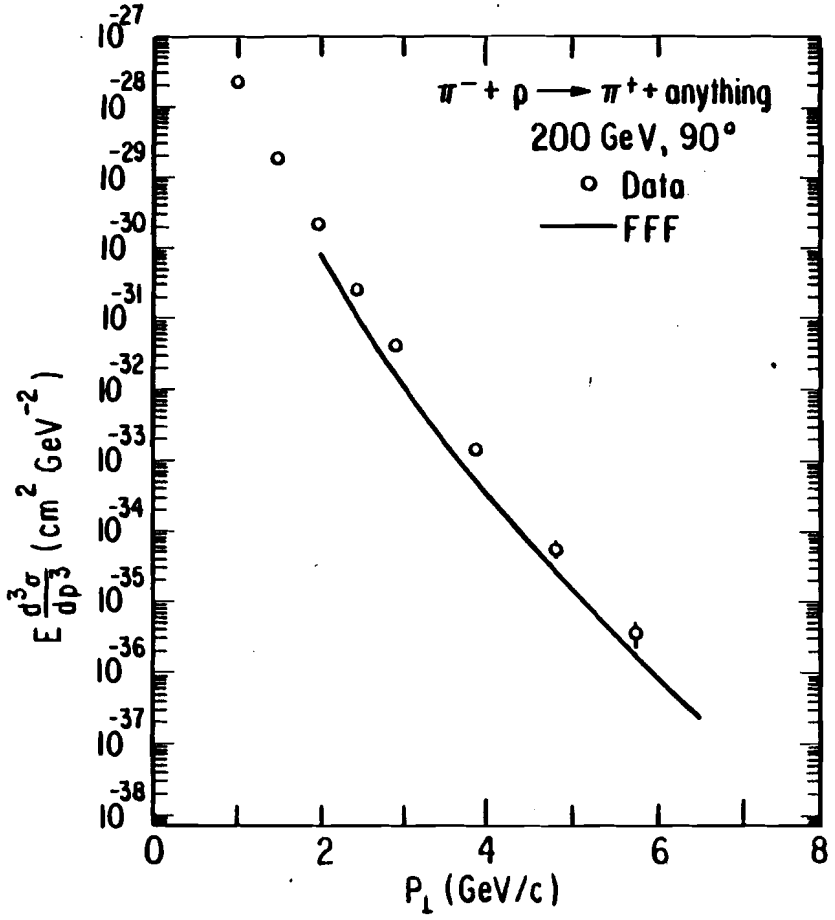
$\pi^- + p \rightarrow \pi^+ +$ anything
200 GeV, 90°
o Data
FFF
$E\frac{d^3\sigma}{dp^3}$ (cm^2 GeV^{-2})
$P_\perp$ (GeV/c)

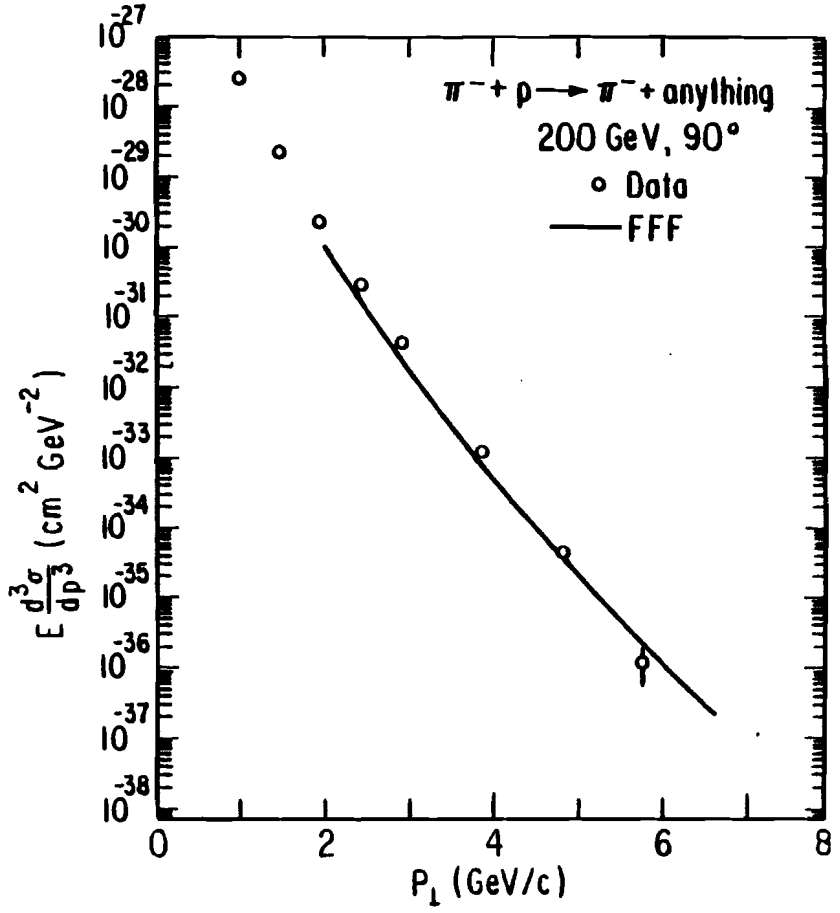
$\pi^- + p \rightarrow \pi^- +$ anything
200 GeV, 90°
o Data
FFF
$E\frac{d^3\sigma}{dp^3}$ (cm^2 GeV^{-2})
$P_\perp$ (GeV/c)

Figure 37.--Comparison of the $\pi^- + p \rightarrow K^+, K^-$ + anything cross sections versus $P_\perp$ with the predictions of the FFF model.

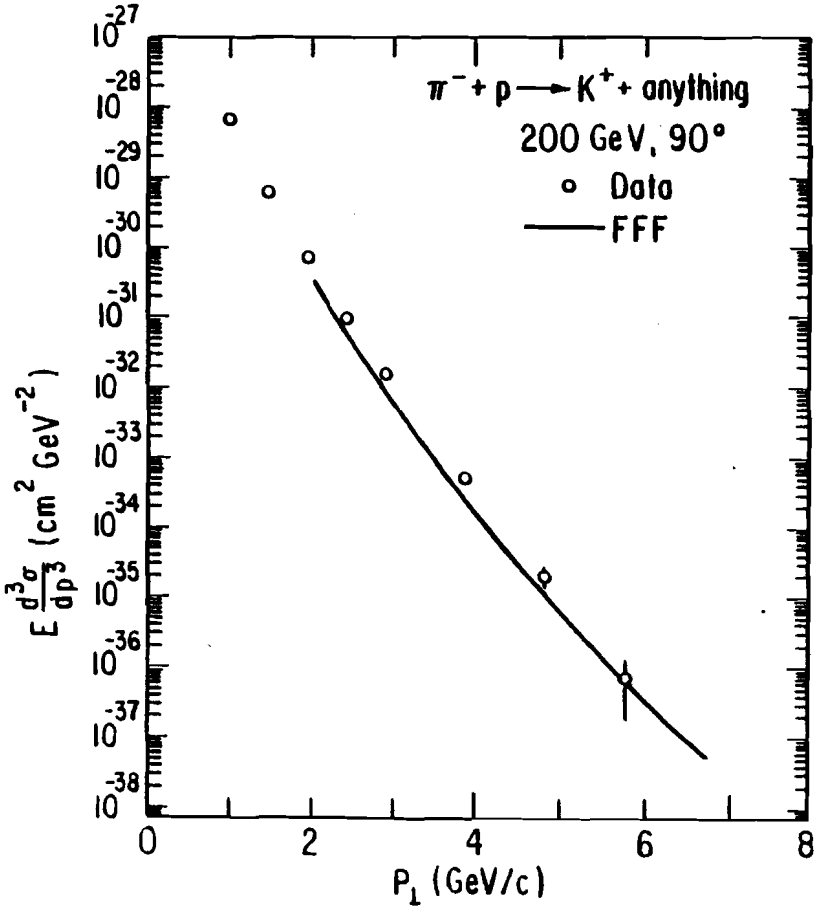
$\pi^- + p \rightarrow K^+ +$ anything
200 GeV, 90°
Data
FFF
$E\frac{d^3\sigma}{dp^3}$ (cm^2 GeV^{-2})
$P_\perp$ (GeV/c)

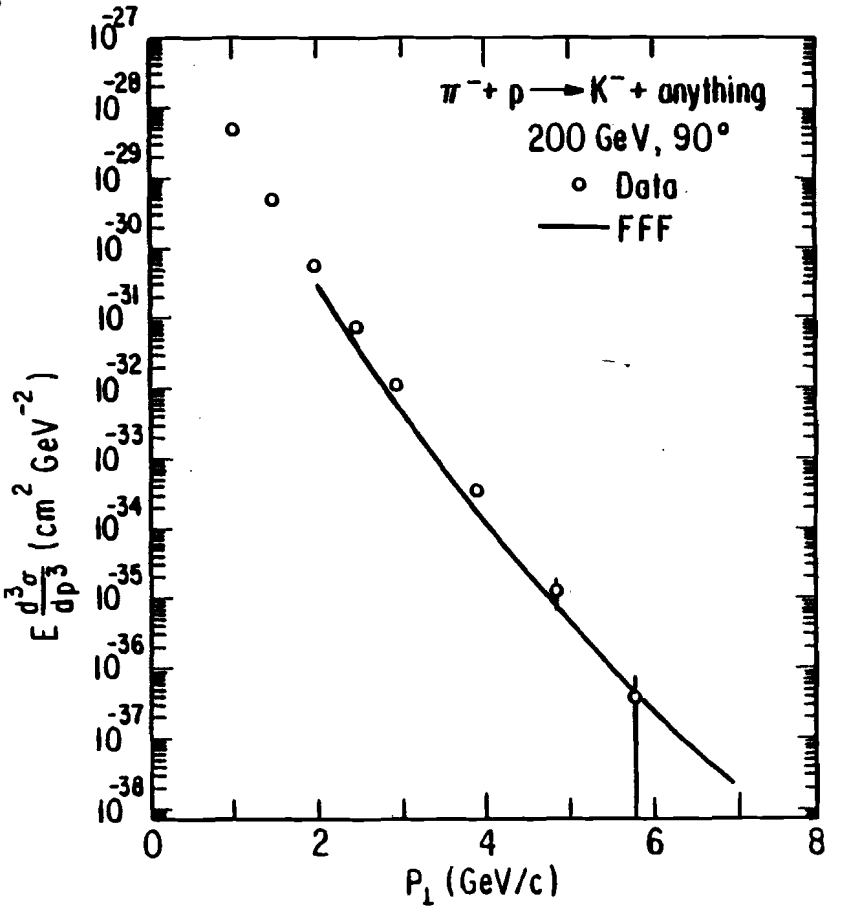
$\pi^- + p \rightarrow K^- +$ anything
200 GeV, 90°
Data
FFF
$E\frac{d^3\sigma}{dp^3}$ (cm^2 GeV^{-2})
$P_\perp$ (GeV/c)

Figure 38.--The three antiparticle/particle trigger ratios, $\frac{\pi^- + p \rightarrow h_1 + \text{anything}}{\pi^- + p \rightarrow h_2 + \text{anything}}$, versus $P_\perp$ for the three CM angles. Also the predictions of the FFF model for the π^-/π^+ and K^-/K^+ ratios are shown.

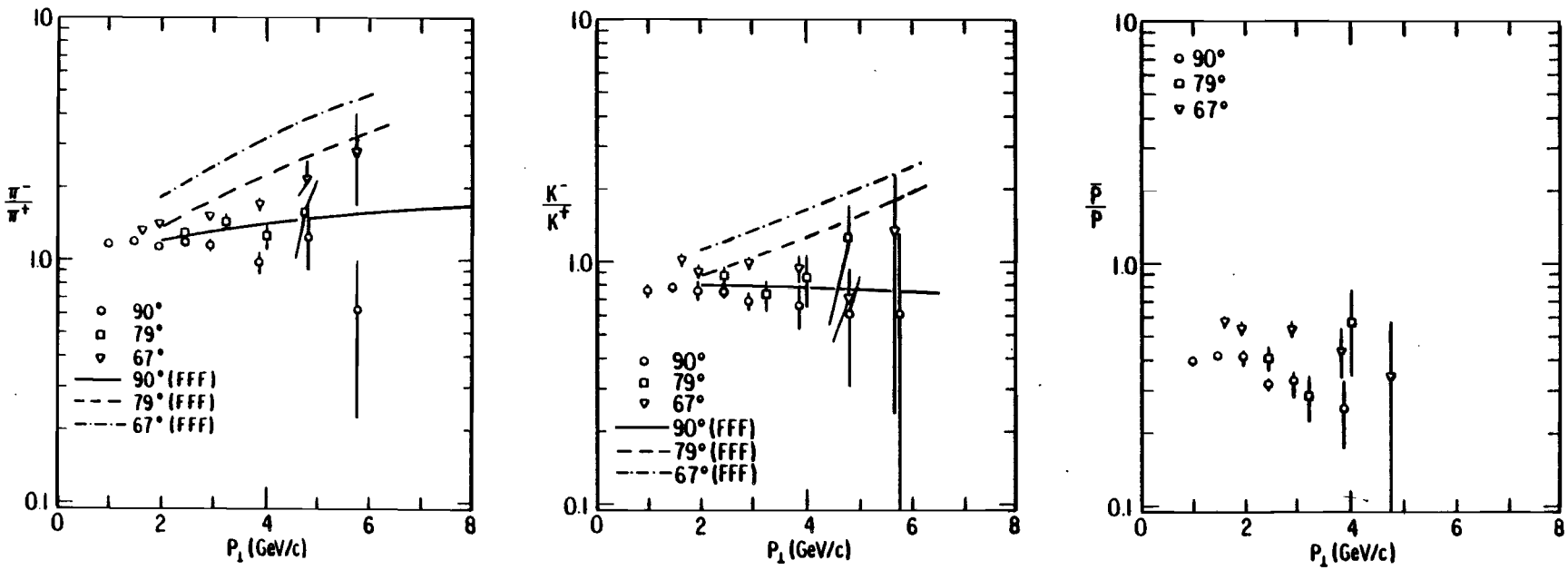
10
1.0
0.1
π^-/π^+
90°
79°
67°
90° (FFF)
79° (FFF)
67° (FFF)
0
2
4
6
8
$P_\perp$ (GeV/c)
K^-/K^+
$\bar{p}/p$

Figure 39.--The K^+/π^+ and K^-/π^- trigger ratios, $\frac{\pi^- + p \rightarrow h_1 + \text{anything}}{\pi^- + p \rightarrow h_2 + \text{anything}}$, versus $P_\perp$ for the three CM angles. Also the predictions of the FFF model are shown.

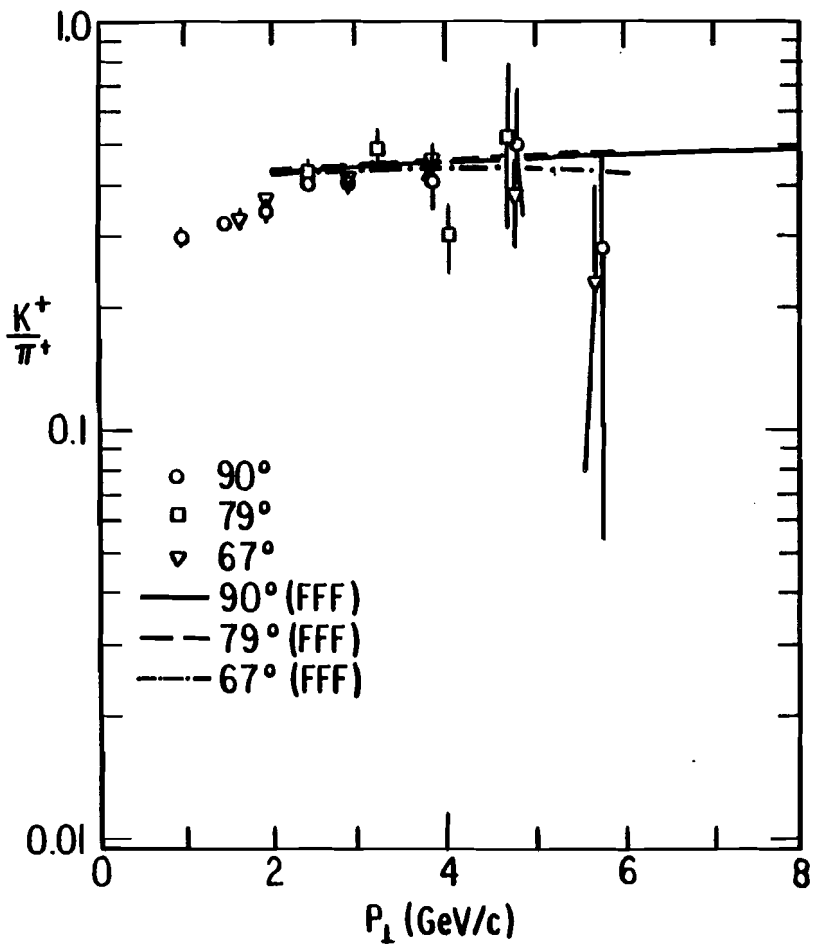
1.0
0.1
0.01
K^+/π^+
0
2
4
6
8
$P_\perp$ (GeV/c)
90°
79°
67°
90° (FFF)
79° (FFF)
67° (FFF)

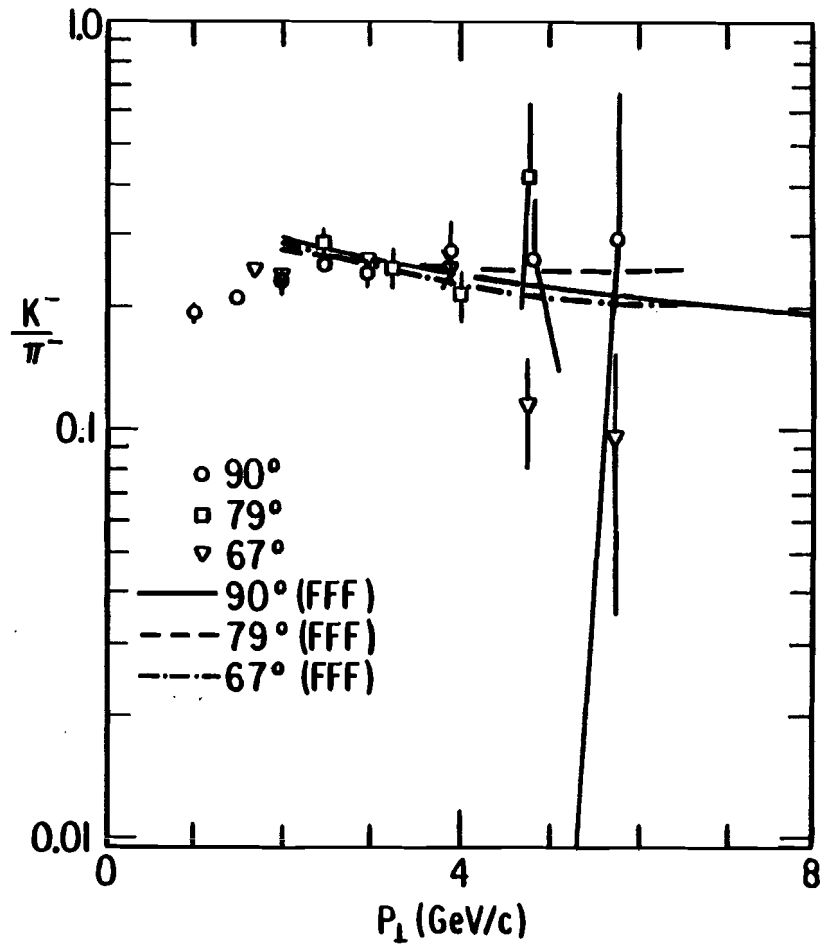
1.0
0.1
0.01
K^-/π^-
0
4
8
$P_\perp$ (GeV/c)
90°
79°
67°
90° (FFF)
79° (FFF)
67° (FFF)

Figure 40.--The π^-/π^+, K^-/π^+ and K^-/π^- trigger ratios, $\frac{\pi^- + p \rightarrow h_1 + \text{anything}}{\pi^- + p \rightarrow h_2 + \text{anything}}$, versus the CM angle at $P_\perp = 4$ GeV/c and with 200 GeV π^- and proton (only at 90° CM angle) beams. Also the predictions of the FFF model are shown (for the distinction between FFF and New FFF see text, page 68).

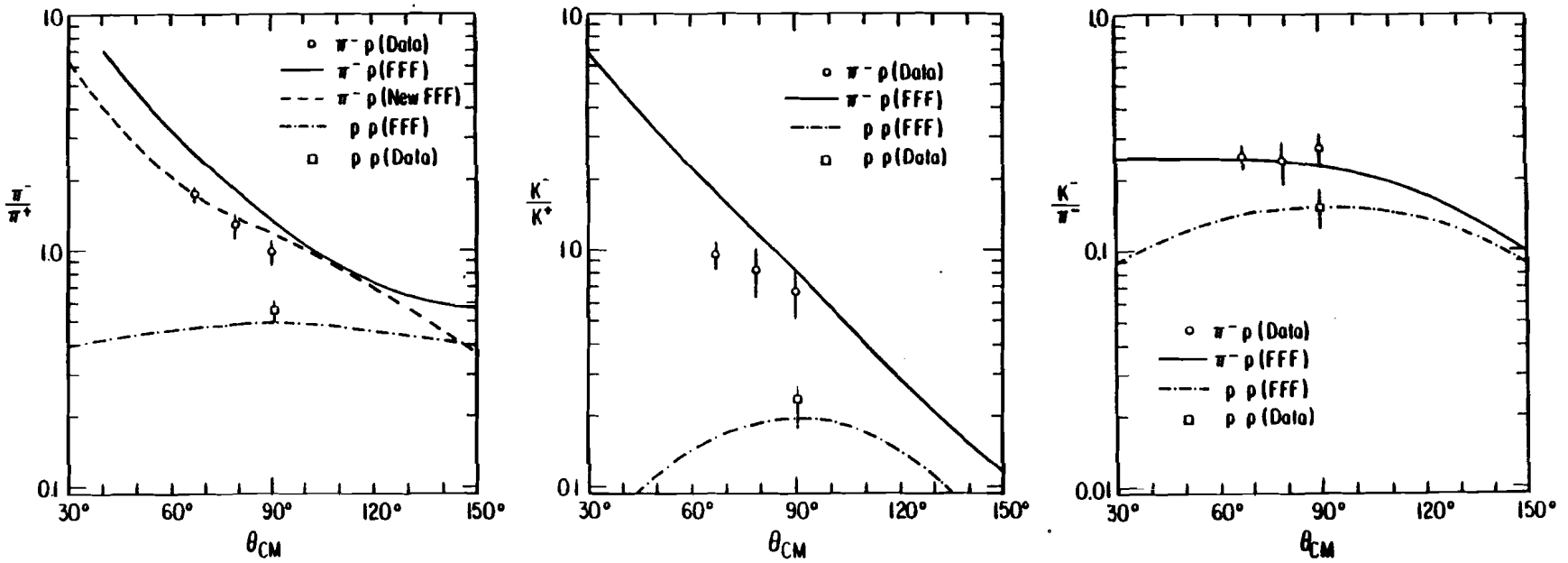
1.0
0.1
$\frac{\pi^-}{\pi^+}$
30°
60°
90°
120°
150°
θ_{CM}
$\pi^- p$ (Data)
$\pi^- p$ (FFF)
$\pi^- p$ (New FFF)
$p\,p$ (FFF)
$p\,p$ (Data)
10
1.0
0.1
$\frac{K^-}{K^+}$
30°
60°
90°
120°
150°
θ_{CM}
$\pi^- p$ (Data)
$\pi^- p$ (FFF)
$p\,p$ (FFF)
$p\,p$ (Data)
1.0
0.1
0.01
$\frac{K^-}{\pi^-}$
30°
60°
90°
120°
150°
θ_{CM}
$\pi^- p$ (Data)
$\pi^- p$ (FFF)
$p\,p$ (FFF)
$p\,p$ (Data)

Figure 41.--Invariant cross sections per nucleus versus $P_\perp$ for the production of each of the $\pi^\pm$, $K^\pm$, p and $\bar{p}$ in π^-W and π^-Be 200 GeV collisions. The 90° angle refers to the π^--nucleon CM system. The lines drawn through the proton points are only to guide the eye.

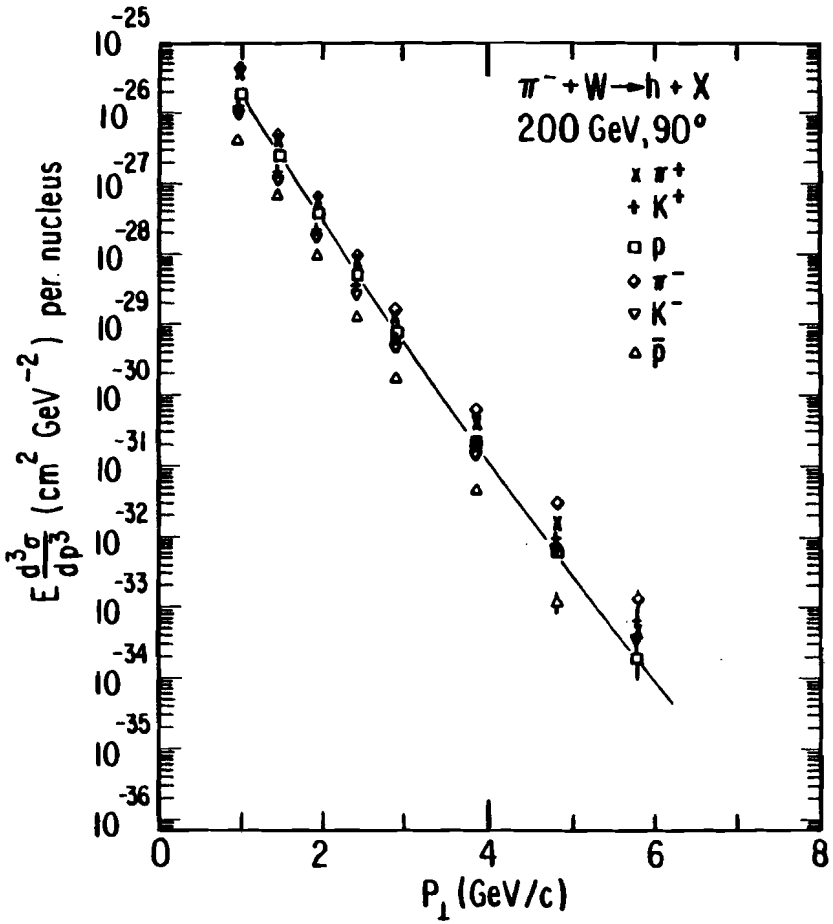
$\pi^- + W \rightarrow h + X$
200 GeV, 90°
x π^+
+ K^+
□ p
◇ π^-
▽ K^-
△ $\bar{p}$
$E\frac{d^3\sigma}{dp^3}$ (cm^2 GeV^{-2}) per nucleus
$P_\perp$ (GeV/c)

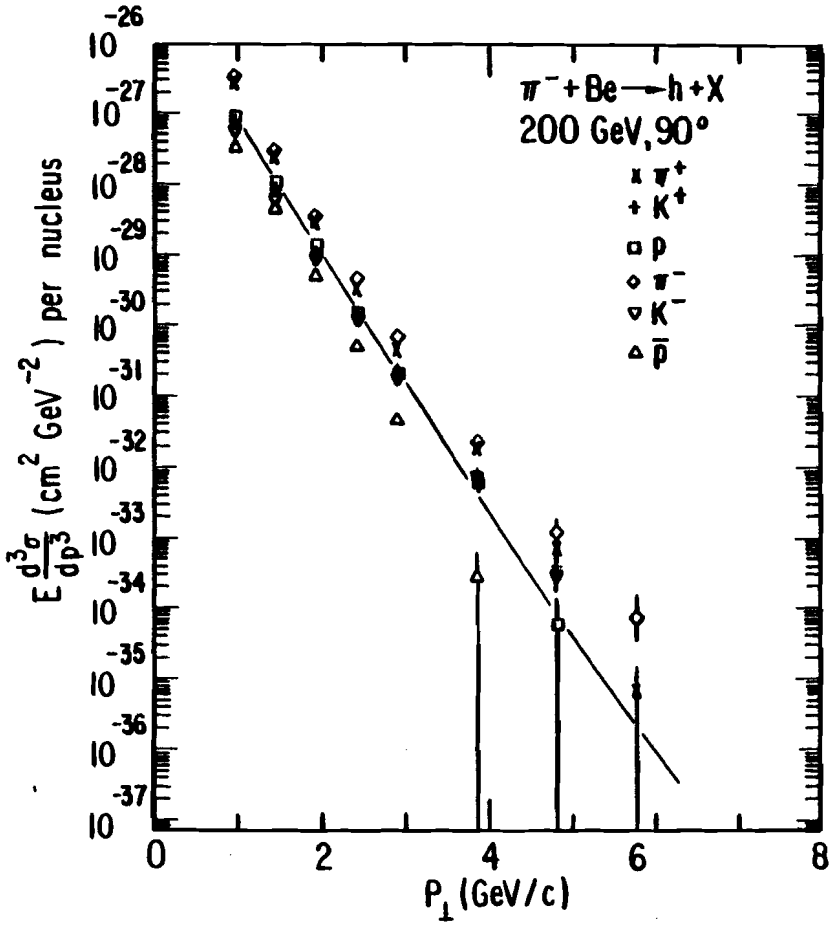
$\pi^- + Be \rightarrow h + X$
200 GeV, 90°
x π^+
+ K^+
□ p
◇ π^-
▽ K^-
△ $\bar{p}$
$E\frac{d^3\sigma}{dp^3}$ (cm^2 GeV^{-2}) per nucleus
$P_\perp$ (GeV/c)

Figure 42.--Comparison of the invariant cross sections per nucleus versus $P_\perp$ for the production of each of π^+, π^-, K^+, K^-, p and $\bar{p}$ with W and Be targets. The 90° angle refers to the π^--nucleon CM system. The lines are to guide the eye through the data points.

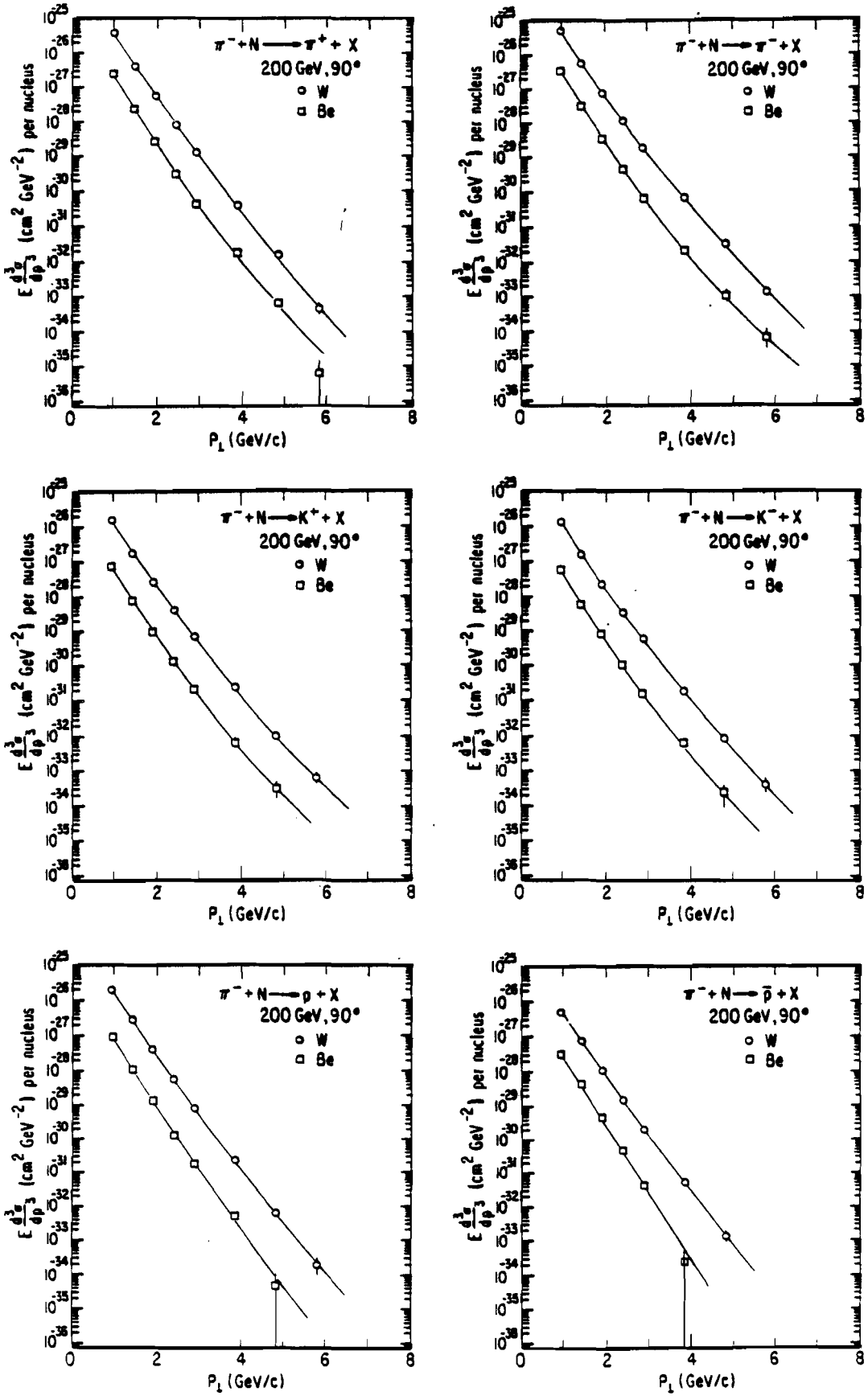
$\pi^- + N \longrightarrow \pi^+ + X$
200 GeV, 90°
W
Be
$\pi^- + N \longrightarrow \pi^- + X$
200 GeV, 90°
W
Be
$\pi^- + N \longrightarrow K^+ + X$
200 GeV, 90°
W
Be
$\pi^- + N \longrightarrow K^- + X$
200 GeV, 90°
W
Be
$\pi^- + N \longrightarrow p + X$
200 GeV, 90°
W
Be
$\pi^- + N \longrightarrow \bar{p} + X$
200 GeV, 90°
W
Be
$E\frac{d^3\sigma}{dp^3}$ (cm^2 GeV^{-2}) per nucleus
$P_\perp$ (GeV/c)

Figure 43.--Invariant cross sections per nucleus versus $P_\perp$ for the inclusive reaction $\pi^- + W \rightarrow \pi^+, \pi^-$ + anything with 200 and 300 GeV beams. The 90° angle refers to the π^--nucleon CM system. The lines are to guide the eye through the data points.

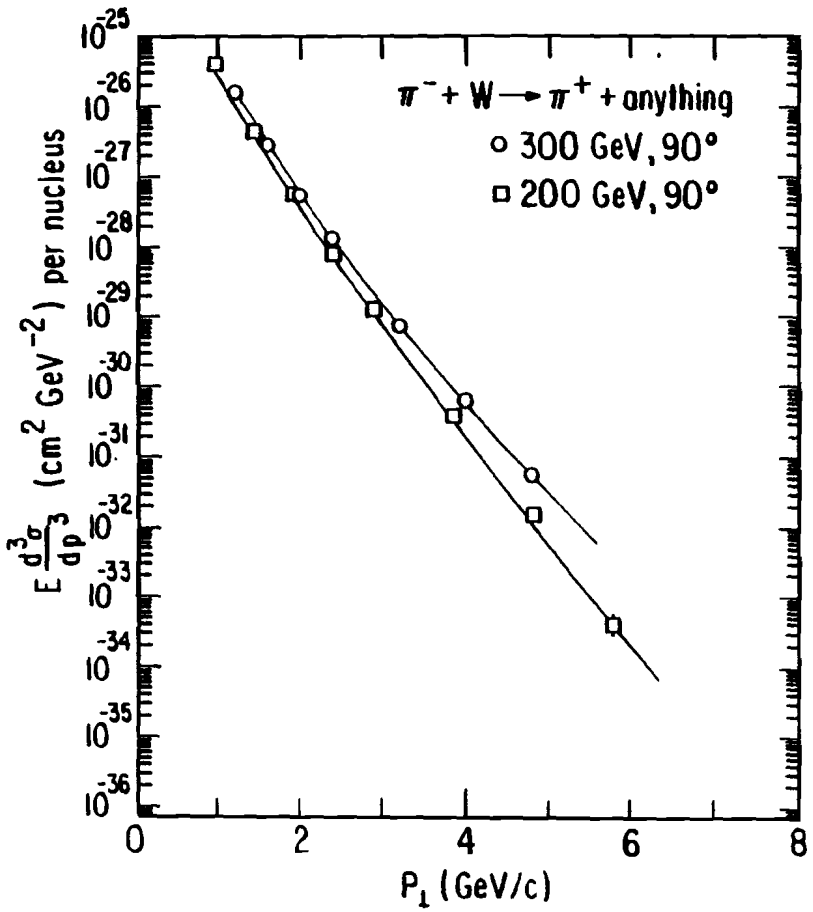
$\pi^- + W \rightarrow \pi^+ + \text{anything}$
○ 300 GeV, 90°
□ 200 GeV, 90°
$E\frac{d^3\sigma}{dp^3}$ (cm^2 GeV^{-2}) per nucleus
$P_\perp$ (GeV/c)

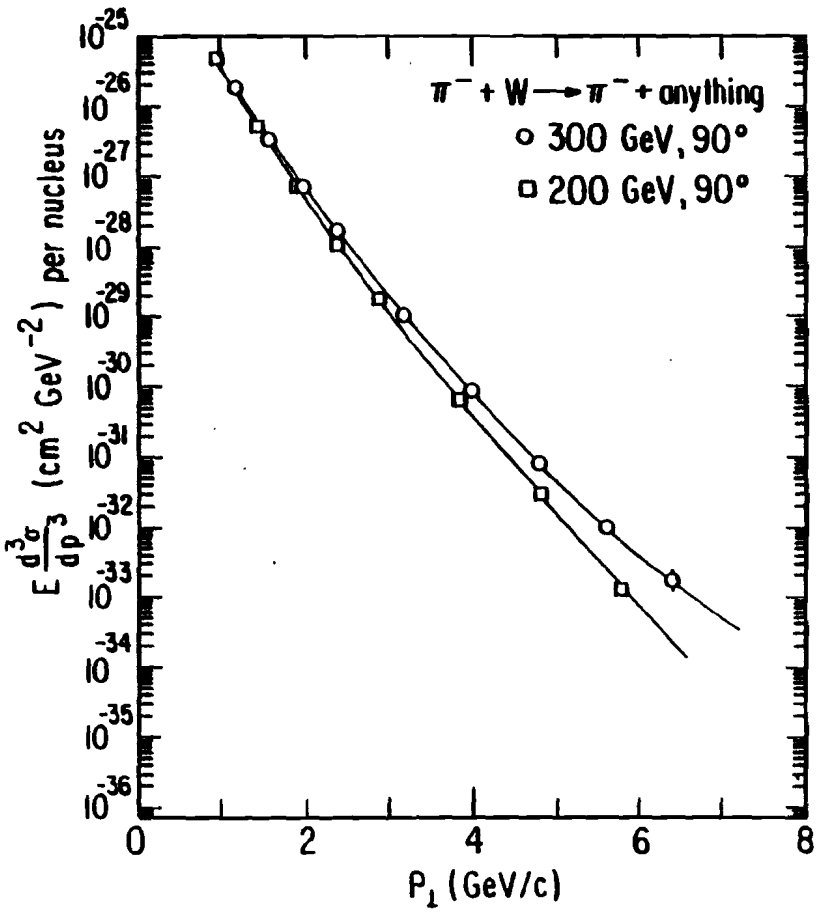
$\pi^- + W \rightarrow \pi^- + \text{anything}$
○ 300 GeV, 90°
□ 200 GeV, 90°
$E\frac{d^3\sigma}{dp^3}$ (cm^2 GeV^{-2}) per nucleus
$P_\perp$ (GeV/c)

Figure 44.--The invariant cross sections for the production of each of the π^+, π^-, K^+, K^-, p and $\bar{p}$ with the H, Be, Cu and W targets relative to the invariant cross section with the W target versus the logarithm of the atomic weight. The straight lines are fits by eye of the nuclear target points. The 90° angle refers to the π^--nucleon CM system.

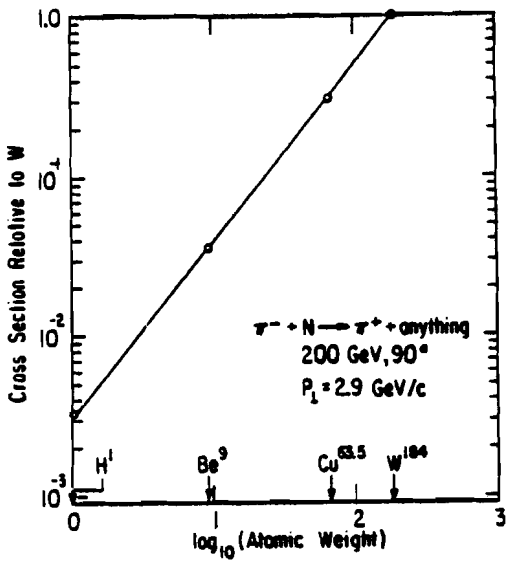
Cross Section Relative to W
$\pi^- + N \rightarrow \pi^+ +$ anything
200 GeV, 90°
$P_\perp = 2.9$ GeV/c
H^1
Be^9
$Cu^{63.5}$
W^{184}
$\log_{10}$ (Atomic Weight)

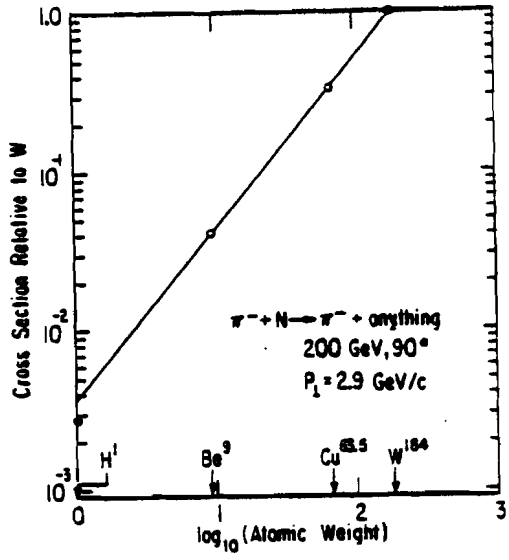
Cross Section Relative to W
$\pi^- + N \rightarrow \pi^- +$ anything
200 GeV, 90°
$P_\perp = 2.9$ GeV/c
H^1
Be^9
$Cu^{63.5}$
W^{184}
$\log_{10}$ (Atomic Weight)

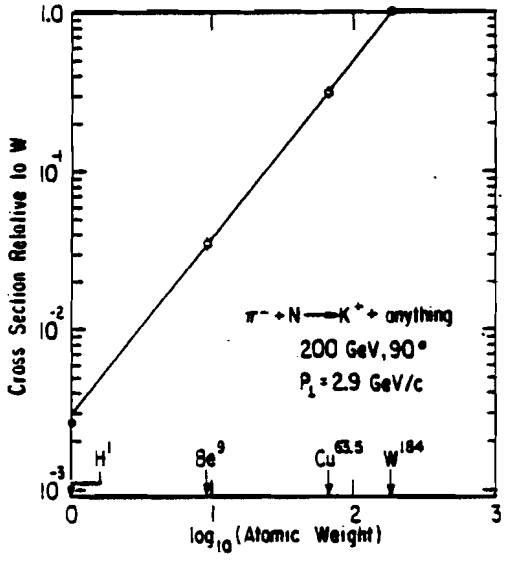
Cross Section Relative to W
$\pi^- + N \rightarrow K^+ +$ anything
200 GeV, 90°
$P_\perp = 2.9$ GeV/c
H^1
Be^9
$Cu^{63.5}$
W^{184}
$\log_{10}$ (Atomic Weight)

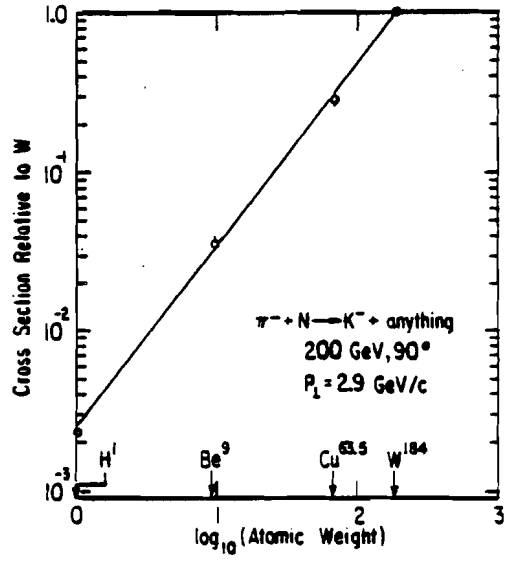
Cross Section Relative to W
$\pi^- + N \rightarrow K^- +$ anything
200 GeV, 90°
$P_\perp = 2.9$ GeV/c
H^1
Be^9
$Cu^{63.5}$
W^{184}
$\log_{10}$ (Atomic Weight)

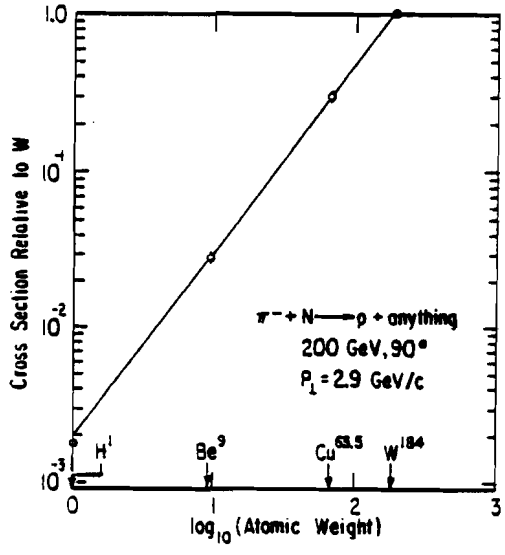
Cross Section Relative to W
$\pi^- + N \rightarrow p +$ anything
200 GeV, 90°
$P_\perp = 2.9$ GeV/c
H^1
Be^9
$Cu^{63.5}$
W^{184}
$\log_{10}$ (Atomic Weight)

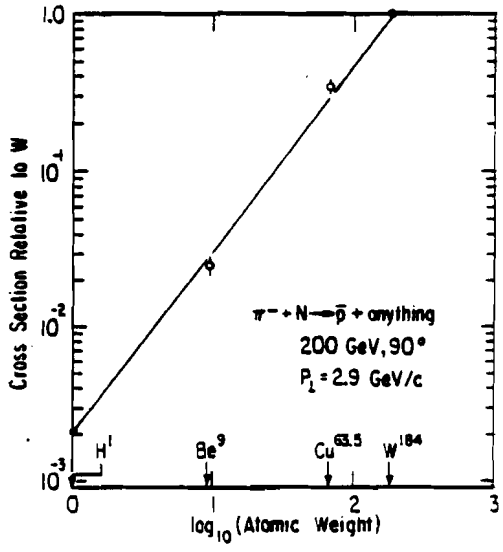
Cross Section Relative to W
$\pi^- + N \rightarrow \bar{p} +$ anything
200 GeV, 90°
$P_\perp = 2.9$ GeV/c
H^1
Be^9
$Cu^{63.5}$
W^{184}
$\log_{10}$ (Atomic Weight)

Figure 45.--The exponents α_i's versus $P_\perp$.

- This experiment (π^- beam).
- Reference 34 (proton beam).

The dashed straight lines at α_i=1 have been drawn for contrast. The 90° and 97° angles refer to the hadron-nucleon CM system.

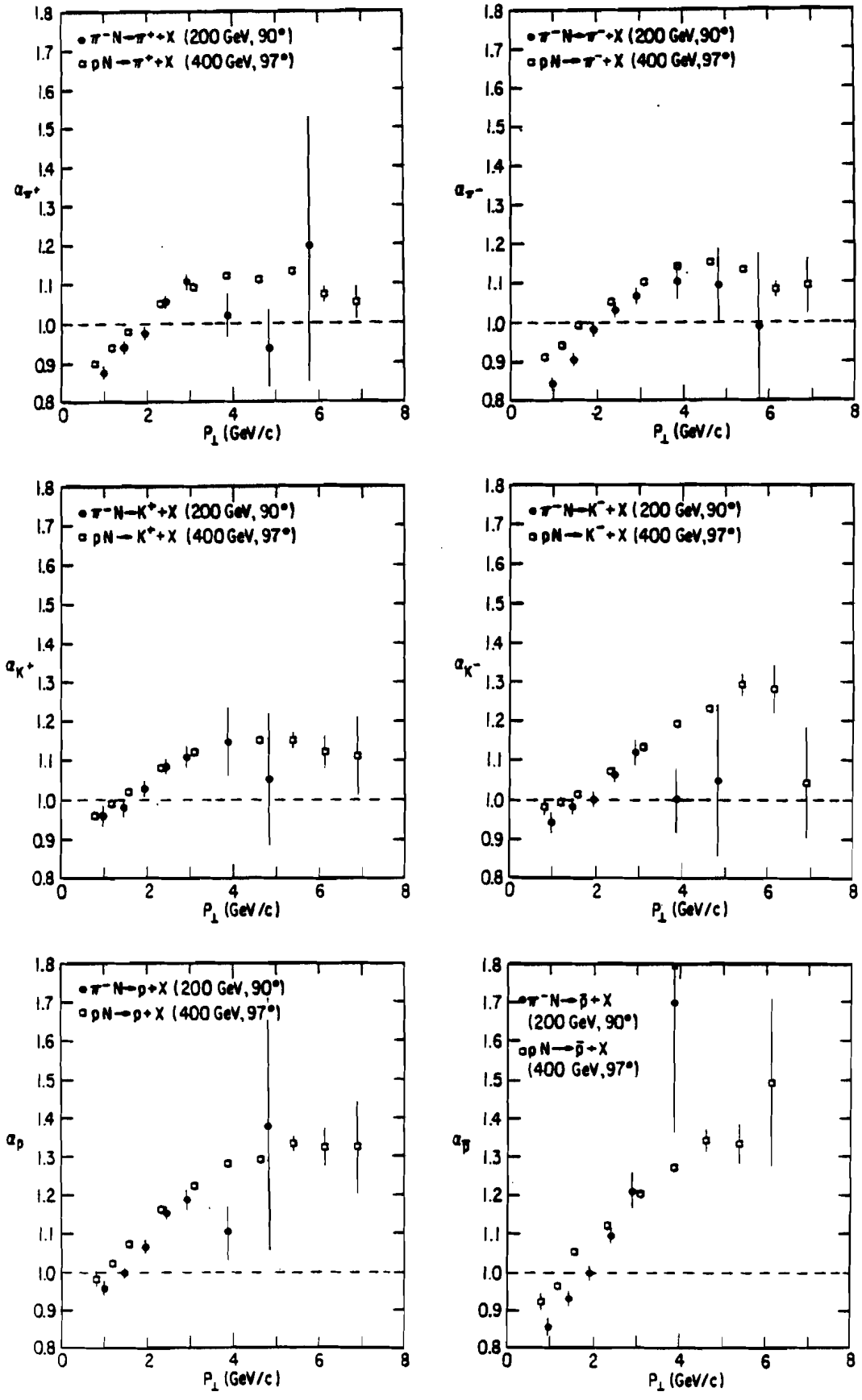
• π⁻N→π⁺+X (200 GeV, 90°)
▫ pN→π⁺+X (400 GeV, 97°)
α_π⁺
• π⁻N→π⁻+X (200 GeV, 90°)
▫ pN→π⁻+X (400 GeV, 97°)
α_π⁻
• π⁻N→K⁺+X (200 GeV, 90°)
▫ pN→K⁺+X (400 GeV, 97°)
α_K⁺
• π⁻N→K⁻+X (200 GeV, 90°)
▫ pN→K⁻+X (400 GeV, 97°)
α_K⁻
• π⁻N→p+X (200 GeV, 90°)
▫ pN→p+X (400 GeV, 97°)
α_p
• π⁻N→p̄+X (200 GeV, 90°)
▫ pN→p̄+X (400 GeV, 97°)
α_p̄
P⊥ (GeV/c)